Increasing robustness, compactness and cost-effectiveness of edge-illumination X-ray phase contrast imaging as a key step towards translation into real-world applications

Dario Basta

Department of Medical Physics and Biomedical Engineering

University College London

A thesis submitted for the degree of

Doctor of Philosophy

July, 2017

I, Dario Basta confirm that the work presented in this thesis is my own. Where information has been derived from other sources, I confirm that this has been indicated in the thesis.

Signed:

Abstract

Novel laboratory implementations of the Edge Illumination X-Ray Phase Contrast imaging (EI-XPCi) method were presented in this thesis, with the aim of facilitating its commercial translation.

A portable system, based on compact piezoelectric motors, was developed to enable the easy transportation of the setup. Tests on the system positioning accuracy were presented, and images of standard samples were benchmarked against those obtained with the existing prototype based on stepper motors.

An alternative EI implementation, which simultaneously allows the use of cheaper X-ray sources and the realisation of more compact setups, was also presented. An additional "source mask" introduced in a standard EI setup allows to section the large focal spot of a conventional tube into multiple sub-sources, creating a corresponding number of spatially shifted images, which need to be disentangled through dedicated algorithms. A proof-of-principle experiment provided results in agreement with simulated predictions, demonstrating the feasibility of the approach.

A quantitative study on the dependence of the angular sensitivity on the source-to-detector distance (at constant system magnification, tube settings and total exposure time) was also presented. Results of a simulation based on the assumption of Poisson-distributed noise in the images (valid for photon counting detectors) were compared with experimental ones obtained by using an integrating detector. The observed discrepancies were successfully

related to the additional noise sources present in an integrating detector, thus indirectly validating the simulation model.

The adaptation of EI with a laser-plasma source was investigated through a proof-of-concept experiment, with the aim of realizing a system providing a synchrotron-like performance with a more compact and accessible setup. Non-ideal experimental conditions affecting the system performance were discussed, while the results of the source characterization were used to establish some basic requirements that must be satisfied to successfully implement EI with these "new generation" X-ray sources.

To my mother and my father...

Acknowledgements

I would like to thank with all my heart my primary supervisor Prof. Alessandro Olivo for the invaluable support and the precious suggestions he gave me with passion and dedication. I will always be grateful to him for motivating me and teaching me values that are so important, not only for research, but for life in general, such as dedication, willingness to pursue personal goals, collaboration and trust in people.

I would also like to thank my second supervisor Dr. Marco Endrizzi for his patience and his constant support. His brilliant mind and his smart approach to problem solving will be a constant source of inspiration for my future career.

A great thank goes also to my third supervisor Dr. Paul Diemoz for the interesting conversions and his availability in giving me important suggestions for my work.

My thanks go also to the friends and colleagues that I met in the Phase Contrast group, such as Dr. Gibril Kallon, Mrs. Anna Zamir, Dr. Alberto Astolfo, Dr. Tom Millard, Mr. Ian Buchanam, Dr. Charlotte Hagen, Mrs. Charlotte Maughan Jones and Dr. Peter Modregger. It has been a pleasure to meet such nice people with so many different interests and ideas, which opened my mind to new perspectives and points of view.

I also want to thank Dr. Silvia Cipiccia and Dr. David Reboredo for their support during the data acquisition at the Strathclyde University in

Glasgow.

A special thank goes to Dr. Fabio Alessio Vittoria. His genuine suggestions and his selfless support, which are so uncommon nowadays, make him a great friend and a laudable colleague. I will always be inspired by his capability to solve problems, his excellent attitude for team work and, most of all, his humbleness, which are all qualities that a good researcher should have.

Finally, my most sincere and deepest thanks go to Sandra for her love and patience, to my parents Giovanna and Fernando for their support and encouragements, and to my friends Francesco Ciccarelli and Francesco Iacoviello for being so close to me especially in difficult situations.

Contents

List of Figures

List of Tables

Introduction

The commercial translation of the Edge Illumination (EI) X-Ray Phase Contrast imaging (XPCi) method has been one of the main goals of research investigations conducted at University College London (UCL) during recent years. In order to make this possible, some important aspects must be considered and optimized, such as flexibility for adaptation to different applications, cost-effectiveness and dimensions of the setup, and easy portability of the equipment.
In this thesis the realization of new and different EI XPCi laboratory implementations are presented, which take into account these aspects.

XPCi is widely used for several applications including medical physics, biology and materials science as an alternative to absorption-based imaging techniques. While the latter provide adequate performances only when the details of interest show attenuation properties significantly different from the surrounding background (like bones in soft tissue), XPCi is more suitable for weakly absorbing materials (e.g. soft tissues, cartilage). The phase shift that X-rays undergo when passing through objects translates into X-ray refraction at very small angles (μrad and below); an imaging set-up with high sensitivity to angular deflections can thus be used to convert phase effects into image contrast.

The most widely used XPCi methods will be reviewed in Chapter 1, with particu-

lar attention to Edge Illumination (EI), which is one of the most promising because of its flexibility and capability to provide intense phase signals even when implemented with conventional laboratory sources.
However, since the method's performance depends on the source characteristics and novel X-ray sources are being developed in various labs in the UK and worldwide, it is important to develop a portable and compact system that enables the easy transportation of the setup.

For this reason, a compact and portable EI system was developed, the design and realization of which will be discussed in detail in Chapter 2.
The system is based on miniaturised and highly precise piezoelectric motors, which, while providing the same positioning accuracy as that provided by the stepper motors used so far to align the optical masks used in EI setups, are much lighter and more compact.
A Labview code was implemented and integrated into the data acquisition software, in order to drive the motors in an automated way and finely adjust their positions through a closed loop procedure, which utilises their built-in sensors. In order to guarantee the portability of the entire system, the code is run on a laptop.
Preliminary tests on the motion accuracy of the new system will be presented, as well as images of standard samples that will be benchmarked against images of the same objects obtained with the pre-existing prototype, based on stepper motors. By evaluating the angular sensitivity in the corresponding refraction images, the performance of the two systems will be quantitatively compared, with the aim of demonstrating that a compact and light EI system can be developed without a loss of angular sensitivity. The results can also be considered as a test of the performance of the piezoelectric motors, and as such should also be of interest to researchers planning their use in other imaging systems.

An important aspect that must be taken into account when considering the realization of novel configurations that allow for the commercial translation of the technique, is the cost of the X-ray sources used in EI setups developed so far at University College London.

In Chapter 3, an alternative EI implementation that simultaneously allows the use of cheaper X-ray sources and the realisation of more compact setups will be presented. The main feature of this new setup is the introduction of a "source mask", the function of which is to section the large focal spot of a conventional X-ray source into multiple sub-sources. These create a corresponding number of spatially shifted images onto the detector, which need to be disentangled by means of appropriate algorithms.

The aim of that part of the thesis work was to show the validity of the above approach, which provides the possibility to exploit cheap laboratory X-ray sources and, at the same time, to realize more compact setups, since the individual "sub-sources" created through the source mask can be smaller than our current standard of 70-100 μm, allowing to reduce the system length.

The possibility of realizing more compact EI setups has been more deeply investigated in Chapter 4, where we present a quantitative study of the angular sensitivity as a function of the distance between X-ray source and detector, at constant system magnification, tube settings and total exposure time.

Under the assumption that Poisson fluctuations are the only source of noise in the images, which is true if a photon counting detector is used, the system's angular sensitivity is constant with the distance as confirmed by a preliminary simulation-based study. This suggests that more compact setups can be used, at least in applications that do not present any requirements in terms of delivered dose.

However, when using an integrating detector, an additional source of noise affecting

the system performance must be taken into account, which alters the above constant behaviour, as discussed more in detail in Chapter 4.

Finally, in Chapter 5 the adaptation of EI with a laser-plasma source was investigated. This represents an example of "new generation" X-ray sources that have been developed during recent years, with the aim of providing synchrotron-like performance with a more compact and accessible setup.
The combination of these "exotic" sources with the EI method, capable of providing unprecedented angular sensitivities when used with highly coherent radiation, was investigated through a proof-of-concept experiment carried out at the ALPHA-X beamline at the University of Strathclyde in Glasgow, where a Laser-Plasma Wakefield Accelerator (LWFA) has been developed.
The non ideal conditions encountered during the experiment, such as instability of the laser, affected the performance of the source and did not allow to perform the acquisition of XPCi data with the EI method. For this reason, it was only possible to image a wire phantom using free space propagation (FSP) XPCi, and perform some degree of characterization of the source in terms of flux and emitted spectrum.
The results of the source characterization were used to establish some basic requirements that must be satisfied in order to guarantee a source performance sufficient to enable the implementation of EI XCPi with the laser-plasma source, which has the potential to represent a valid alternative to synchrotrons and find uses in the field of medical imaging and beyond.

1

X-ray Imaging

1.1 X-ray production

Different techniques for X-ray production have been developed since their discovery in 1895 by Rontgen [7]. Among all of them, the most common is to make use of X-ray tubes, exploited in many fields including medical physics, security, environmental and material science. These devices are very suitable for applications where costs and dimensions of the setup must be contained, without requiring extreme performances. They can produce up to 10^9 photons/sec [7] and, depending on the specific application, are characterised by focal spots ranging from tens to hundreds of μm (or even $\sim 5 \div 10$ μm for microfocal sources).

A huge improvement in the production of X-rays is achieved by using synchrotron sources, which can produce highly collimated beams with an angular divergence of less than 1 milliradian [7] and they can produce a flux up to 10 orders of magnitude higher than the one obtained by tubes. They are very suitable for applications where very high fluxes and high degrees of coherence are required. The downside of such sources is their very high costs, large dimensions and limited access, which make them unsuitable for real-world applications. For this reason, new kind of X-ray sources have been developed,

with the aim of realising systems with synchrotron-like performances, while being less bulky and expensive. Among new generation sources [8], laser plasma [9] represent one of the most promising due to their good compromise between high flux and dimension (and cost) of the setup: in Chapter 4 we will discuss the working principle of such sources more in detail and will analyse some data acquired by using the one available at the Strathclyde University in Glasgow.

An important parameter that allows the evaluation of the quality of an X-ray source is given by the brilliance, defined as:

$$Brilliance = \frac{N_{ph}}{sec \cdot mrad^2 \cdot mm^2 \cdot 0.1\,\%\,BW} \tag{1.1}$$

which expresses the number of photons N_{ph} produced per unit time (in sec), within a unit solid angle (in $mrad^2$), by a unit source area (in mm^2), within an energy bandwidth of 0.1 %.

Typical values of brilliance achievable with synchrotrons sources are up to 10 orders of magnitude higher than those obtained with X-ray tubes. However, depending on the specific applications, one type of source can be more convenient than the other.

In the next paragraphs we will give an overview of the most popular methods to produce x-rays, discussing the main properties, comparing the performances and evaluating in which contexts one is more suitable than the others.

1.1.1 X-ray tubes

X-ray tubes [10] consist of an evacuated vessel containing two electrodes between which a high potential difference is applied. A schematic of an X-ray tube with its major components is shown in Fig. 1.1.

The cathode consists typically of a tungsten filament, which emits electrons via thermionic emission. The electron beam is accelerated toward the anode by the high potential dif-

ference, hitting the target and interacting with its atoms. The anode is made of a metal plate characterized by high atomic number and high melting point (usually tungsten, molybdenum or rhodium), often embedded in a large mass of copper to facilitate heat dissipation. In order to make the latter more efficient, a *rotating anode* can be used, which allows to spread the heat over a larger area [10].

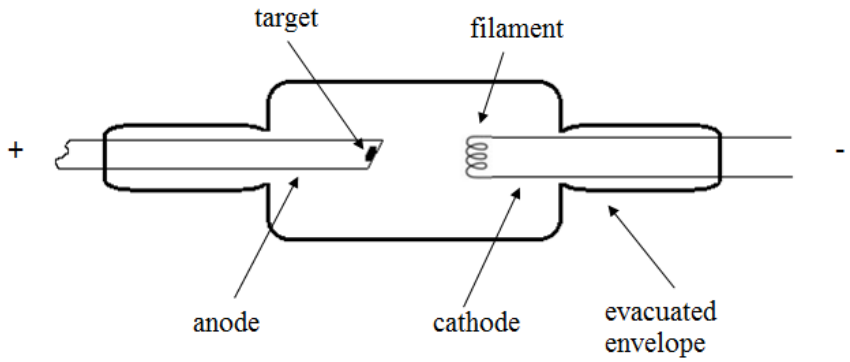

Figure 1.1: Schematic of an X-ray tube with a rotating anode target.

The interaction of the electrons with the target material causes the emission of X-ray radiation via two dominant processes, *bremsstrahlung* and emission of *characteristic lines*, whose corresponding contributions to the spectrum are shown in Fig. 1.2).
Bremsstrahlung is the radiation emitted by an electron when decelerated by the nuclei of the target atoms and is characterized by a continuous energy distribution.
Characteristic lines represent the radiation emitted when an electron ionises an atom by liberating an electron from the inner energetic levels: when the perturbed atom relaxes to its ground state, an electron from an outer shell drops down to fill the vacancy, emitting a photon with energy corresponding exactly to the difference between the energy of the two shells. This radiation is characteristic of the atomic energy levels of the material used as a target and is responsible of the peaks observed in the emission spectrum, superimposed to the continuous bremsstrahlung contribution.

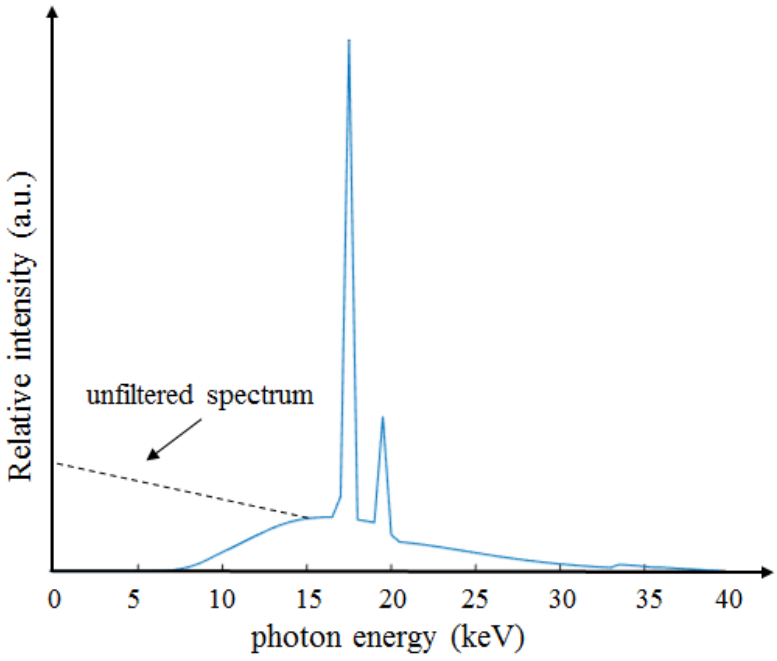

Figure 1.2: Simulated emission spectrum by an X-ray tube using a molybdenum target operated at 40 kVp. The continuous energy distribution is due to bremsstrahlung, while the peaks at approximately 17.5 keV and 19.6 keV correspond respectively to the K_α and K_β emission lines (the first resulting from an L to K shell transition, while the second from an M to K shell transition). The maximum photon energy (which is 40 keV in this case) corresponds to the case where all the kinetic energy of the electron accelerated to the anode is lost in one head-on collision. The minimum energy cut-off is due to the target self-filtration and corresponds to the minimum energy at which X-rays can escape from the target without being re-absorbed.

With a *fixed-anode* source, the peak brilliance achievable with bremsstrahlung are of the order of $10^5\, photons\, s^{-1}\, mm^{-2}\, mrad^{-2}\, per\, 0.1\%\, bandwidth$, while the brilliance of characteristic lines from targets such as copper or molybdenum can be two to three orders of magnitude higher [8]. With rotating anodes, which are able to sustain higher electron currents (and thus to produce more flux), the brilliance can be improved by roughly one order of magnitude for both bremsstrahlung and characteristic radiation. Nevertheless, the main limitation of conventional X-ray tubes is their *very low efficiency in X-ray production*, because less than 1% of the energy absorbed by the anode

is re-emitted in the form of X-rays, while the rest is dissipated in the form of heat [11].

1.1.2 Synchrotron sources

A further improvement in the production of X-rays is obtained by using synchrotron radiation sources [7] [8] [12] in which a relativistic charged particle is accelerated along curved trajectories. In general, whenever a charged particle undergoes an acceleration, it emits electromagnetic radiation. For example, when electrons are subjected to an acceleration perpendicular to their velocity, their direction is changed and they travel on a circular path. When the electron energies are well above the rest mass energy, relativistic effects cause the radiation to be strongly collimated in the direction parallel to the particle velocity $\vec{v}$, within a forward cone with opening angle:

$$\alpha \approx \frac{1}{\gamma} \tag{1.2}$$

where $\gamma \equiv 1/\sqrt{1-\frac{v^2}{c^2}}$ is the *Lorentz factor*, which is also equivalent to the ratio between the total energy of the particle and its rest-mass energy. Since the electron's rest mass energy is only 0.511 MeV, at an energy of 511 MeV the opening angle of the cone is only 10^{-3} radian (at 5.1 GeV the angle is ten times smaller) [12].

In a synchrotron source, electrons are usually injected in a *storage ring* and kept circulating at relativistic energies (typically of the order of GeVs). In a section of the storage ring, the electron passes through a *bending magnet* which produces a uniform magnetic field, causing the electron to move on a circular orbit and emitting a very intense radiation, collimated in a very narrow cone as shown in Fig. 1.3.

The peak brilliance of the radiation produced by a bending magnet is of the order of 10^{15} $photons$ $\mathrm{s}^{-1}mm^{-2}mrad^{-2}$ per 0.1 %BW (with typical electron currents of the order of a few hundreds mA and energies of a few GeV [7]), which is ten orders of magnitude larger than the peak brilliance achievable with X-ray tubes.

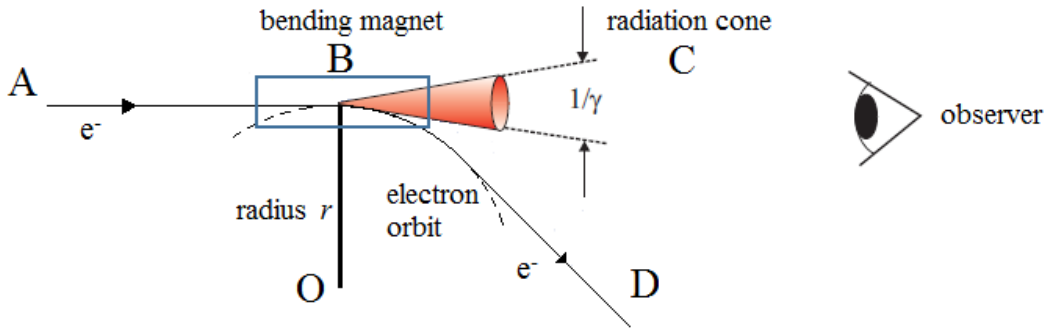

Figure 1.3: Electron bunch accelerated in a bending magnet - the electron bunch at point A passes through a *bending magnet* B that produces a uniform magnetic field pointing in the plane of the page. The associated Lorentzian force causes the electrons to move on a circular orbit with radius r and center O, lying in the plane of the storage ring. In accelerating the electrons within the bending magnet, a tightly collimated cone C of synchrotron radiation is emitted, before emerging from the magnet to travel along the straight path D.

The broad emitted power spectrum from a bending magnet has a critical frequency

$$\omega_c = \left(\frac{3}{2}\right)\gamma^3\omega_0 \tag{1.3}$$

where ω_c is defined in such a way that half of the emitted power lies below its value, while ω_0 is the cyclic frequency of the orbiting charged particle. With ω_0 being of order of 1 MHz in a typical storage ring, and $\gamma \sim 10^4$ (with electron energies of 5 GeV), bending magnet radiation has a critical energy of around $10^{18}Hz$, corresponding to a wavelength of 1 Å typical of hard X-rays [7].

There is a much more efficient way to produce X-ray beams from a synchrotron than by having the electrons orbiting in a purely circular arc. In a typical storage ring there are straight sections followed by circular arc segments. In any one of these straight sections, a device can be inserted, forcing the electrons to oscillate around their trajectory

by means of an array of magnetic dipoles which produce an alternating magnetic field. The corresponding synchrotron radiation is emitted within forward-pointing narrow cones with different directions: the degree of overlap between these radiation cones can discriminate between *wigglers* and *undulators*, as shown in Fig.1.4.

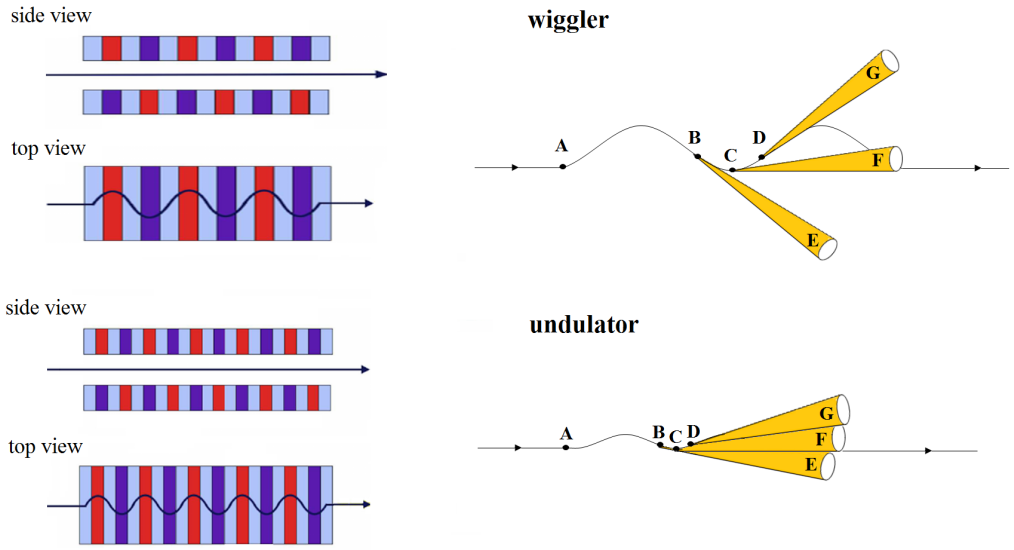

Figure 1.4: Schematic of a wiggler (Top Left) and an undulator (Bottom Left), with their respective emitted radiation cones.

For a wiggler, the radiation cones do not have a significant degree of overlap. Only the forward-pointing ones will overlap (like cone F), the number of which depends on the number of the magnetic dipoles. The electromagnetic fields add incoherently, with a resulting spectrum which is smooth and broad. The intensity of the spectrum depends on the period of the wiggler: the smaller the period, the higher the number of overlapping cones, the more intense the resulting radiation.

An undulator is basically a wiggler with a period of the magnetic dipoles sufficiently small, that the cones E, F, and G have a significant degree of overlap. The radiation emitted by a given electron at one oscillation is in phase with the radiation from the

following oscillation. The amplitude of the radiated waves adds coherently for wavelengths corresponding to the harmonics of the device and the resulting X-ray spectrum is sharply peaked at those harmonics.
The typical brilliance achievable with a wiggler is one to two orders of magnitude larger than the one obtained using bending magnets, while the brilliance of undulator radiation is typically three to four order of magnitude greater [8].

1.2 X-ray interactions with matter

When X-rays interact with matter, they can be transmitted, absorbed or scattered, depending on their energy and on the properties of the material [10] [7].
In the first case, their kinetic properties (energy and momentum) are not changed after passing through the object. In the second case, they are stopped in the material, delivering their energy to the medium in a process called *photoelectric absorption*. This process occurs when a photon, incident with energy $E = h\nu$ on a bound electron with binding energy B_e, is totally absorbed by the latter. This can happen only if $h\nu \geq B_e$; the electron is then emitted with energy $\mathrm{T} = h\nu - B_e$. The effect dominates at lower energies $(10 \div 100)keV$.
In the third case, they can undergo energy and momentum variations caused by *Compton scattering*, or just momentum transfer in a process called **coherent scattering**. The former occurs when the X-ray photon interacts with an individual electron with a binding energy sufficiently small to be considered negligible compared to the energy of the X-ray. In this case, scatter is inelastic: both energy and momentum are exchanged between the photon and the electron. This scattering is incoherent because the free electrons interact with photons independently. This process increases with electron density and dominates in the energy range $(10keV \div 100MeV)$. On the other hand,

coherent scattering occurs when X-ray photons interact with the entire electron cloud. The scattering process is elastic (there is only momentum exchange). Furthermore, since the photon wavelength λ is greater than the electron spacing, the interaction happens with the whole electron cloud, which oscillates at its resonance frequency, emitting radiation. The process increases with Z (atomic number) and takes places at energies between 10 and 100 keV, but it is rarely important in the medical physics energy range, compared to the other two processes.

For sake of completeness, I mention also another process called *pair production*, which dominates at energies well above 1 MeV and for this reason has no direct relevance for diagnostic radiology. When a photon with energy > 1.02 MeV interacts with the electrostatic field of the nucleus of high Z materials, its energy can be converted into electron and positron pair. As a consequence of the energy-mass equivalence, there is a well-defined threshold of 1.02 MeV (= 2 times the electron rest mass) below which the process cannot take place.

1.3 Conventional X-ray imaging

There is more than one way to produce image contrast by using X-rays. *Conventional X-ray imaging* was the first to be developed and is based on a physical principle that exploits the different attenuation properties of the materials when crossed by X-rays. By referring to Fig.1.5, one can define the attenuation contrast C_{att} as the relative difference between the detected intensity I_1 of X-rays transmitted immediately outside the detail of interest and the intensity I_2 of those transmitted through it:

$$C_{att} = \frac{I_1 - I_2}{I_1} \tag{1.4}$$

The intensities I_1 and I_2 are expressed by [11]

$$I_1 = I_0 exp(-\mu_1 t_1); \qquad I_2 = I_0 exp\left[-\mu_1(t_1 - t_2)\right] exp(-\mu_2 t_2) \tag{1.5}$$

where I_0 is the X-ray intensity impinging on the imaged object, μ_1 the attenuation coefficient of the background, μ_2 the attenuation coefficient of the detail of interest, t_1 and t_2 the thicknesses of the background and the detail, respectively.

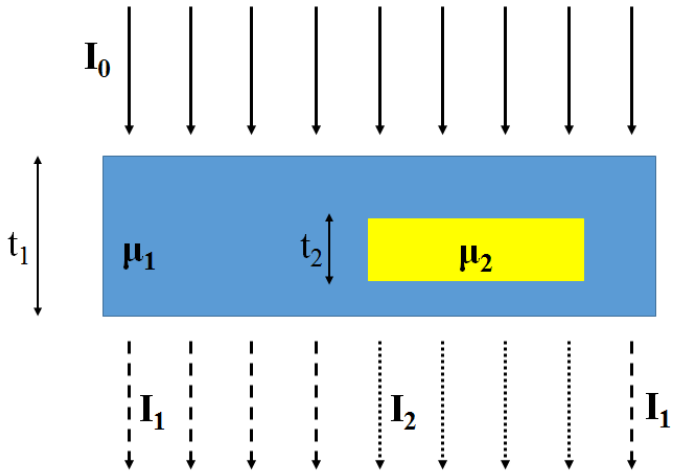

Figure 1.5: Conventional X-ray imaging working principle.

By inserting the expressions 1.5 in the definition 1.4, we obtain

$$C_{att} = 1 - exp\left[(\mu_1 - \mu_2)t_2\right] \tag{1.6}$$

It can be noted that the attenuation contrast depends only on the difference $(\mu_1 - \mu_2)$ of the attenuation coefficients and on the thickness t_2 of the detail. An other important thing to notice is that, when the detail is very thin (i.e. $t_2 \sim 0$) and/or has similar attenuation properties as the background (i.e. $(\mu_1 - \mu_2) \sim 0$), the contrast becomes very small.

Conventional X-ray imaging is extensively used nowadays in several medical applications (e.g. radiography, mammography, angiography, etc.), but also in industry (e.g. non-destructive testing and quality control) and security (e.g. detection of weapons and explosives). Nevertheless, despite the significant innovation brought by the introduction of digital detectors [13] and the development of computed tomography [14, 15], the method used to generate image contrast has remained the same for many years, basically since the discovery of X-rays in 1895 by Rontgen [16].

In summary, the main limitation of the conventional technique is that is very efficient only when the detail of interest shows absorption properties stronger than the surrounding background (e.g. bones in a tissue).

However, there is a wide class of materials (like soft tissues, cartilage, micro calcifications, etc.) which is characterized by weak absorption properties, but that can exhibit much stronger phase shift effects. The latter are responsible for the deviation of X-rays from their original path when they pass through the sample, giving rise to refraction. For this reason, an alternative technique called *X-ray Phase Contrast imaging* (XPCi) has been developed, which exploits the refraction properties of X-rays.

1.4 X-ray Phase Contrast imaging (XPCi)

The complex refractive index n of a material can be represented as:

$$n = 1 - \delta + i\beta \tag{1.7}$$

where the imaginary part β is related to the absorption properties, while the unit decrement of the real part δ refers to the phase shift of the X-rays when they pass through the thickness of the imaged object. For most biological materials and in the energy range of X-ray imaging (typically from tens of keV to 100 keV) [11], the phase effect

term is much larger than the absorption one (up to 3 orders of magnitude).

When X-rays pass through materials with different refractive indexes, their speed varies. As a consequence, different parts of the X-ray wave front could be anticipated or delayed, creating a distorted wave front. Image contrast can then be generated in two ways:

1. detection of the interference patterns arising from the interaction of distorted waves and unperturbed ones;

2. detection of angular deflections resulting from wavefront distortions caused by phase shifts. It can be shown [17] that:

$$\alpha = \frac{1}{|\vec{k}|} \cdot |\vec{\bigtriangledown}_{xy}\phi| = \left| \vec{\bigtriangledown}_{xy} \int_{object} \delta(x,y,z)dz \right| \tag{1.8}$$

   where α is the deviation angle, $|\vec{k}| = \frac{2\pi}{\lambda}$ is the wave vector of an X-ray with wavelength λ, z is the initial propagation direction and $\vec{\bigtriangledown}_{xy}$ is the gradient operator (derivatives are performed along the transverse directions x and y).

From equation 1.8, we can see that the phase shift ϕ is related to the real part of the refractive index δ via the relation $\phi = \int_{object} \delta(x,y,z)dz$, where the integral is taken along the X-ray propagation direction z. Hence, by using an imaging setup with high sensitivity to X-ray angular deflections α, it becomes possible to convert phase effects into image contrast.

Below we will briefly introduce the main X-ray Phase Contrast imaging (XPCi) methods [18], explaining the basic principles they are based on and underlining their main advantages and disadvantages.

1.4.1 Free Space Propagation (FSP)

FSP is the simplest XPCi method because it does not require the introduction of any optical element along the beam path, as shown in Fig. 1.6.

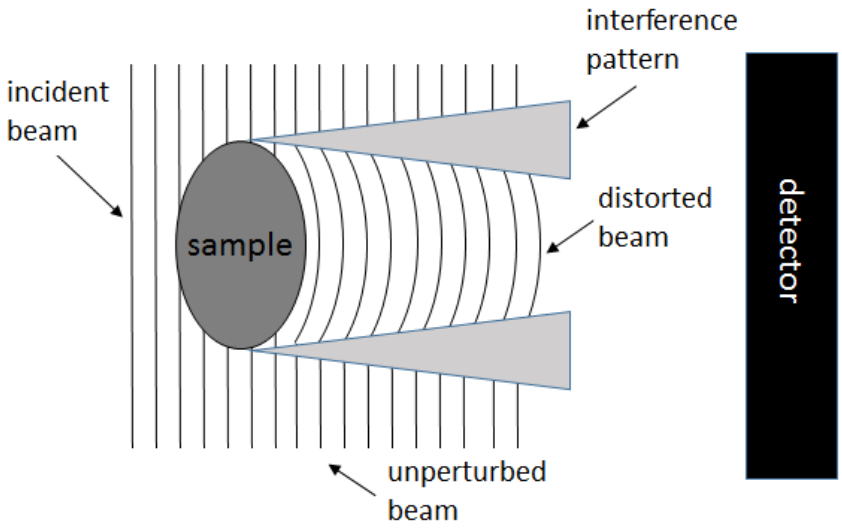

Figure 1.6: Free Space Propagation (FSP) working principle.

The setup is very similar to the one used in conventional radiography, with the main difference that in FSP the sample is placed at some distance from the detector, instead of being in contact with it. If the propagation distance is sufficient, the wave fronts that were distorted for having passed through the sample, interfere with the unperturbed wave fronts. The resulting signal consists of strong positive and negative oscillations, and can be calculated via the Fresnel/Kirchoff diffraction integral [17, 19, 20].

The typical interference pattern of a cylindrical sample that would be produced by a point source and acquired with a detector with virtually infinite spatial resolution is shown in Fig.1.7. This is characterized by the main positive/negative pair of peaks corresponding to the object edges, as well as a series of secondary minima and maxima. However, this is an ideal case that can be never realized in practice [20]. In order to take into account both detector resolution and finite source size [21], one should con-

volve the "ideal" pattern generated by a point source with the detector point spread function PSF and with the projected source distribution $S_{pr} = \frac{d_{sd}}{d_{ss}} S$ (where d_{sd} is the sample-to-detector distance, d_{ss} is the source-to-sample distance and S is the spatial distribution of the real source), the ultimate effect of which is to broaden the main peaks and reduce their intensity. However, the blurring effect of the detector and of the source can be partly eliminated through deconvolution procedures [22, 23].

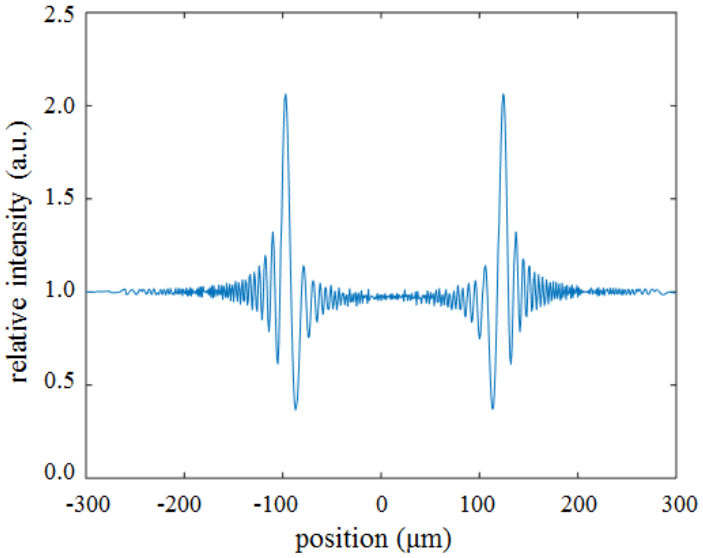

Figure 1.7: Free-space propagation interference pattern of a cylindrical object produced by an "ideal" point source distribution.

One advantage of FSP imaging is that it does not require any stringent requirements in terms of temporal coherence and therefore it works also with polychromatic radiation [17]. Several phase retrieval methods have been developed [24] [25], including an energy-based approach [26], holotomography [27] and single shot retrieval [28]. The method can be extended to CT [29] [30] [31] and can be used for many applications [32] [33] including also mammography [21] [34].

Furthermore, the setup is very simple and does not require any alignment procedure, which can instead be crucial for other methods employing optical elements, such as

grating interferometry and edge illumination.

However, a high degree of spatial coherence is required for the method to work properly. This can be achieved either with Synchrotron Radiation (SR) or micro-focal sources [18]. The problem is that SR sources are very expensive and are available only for limited time slots (beam-time is awarded on the basis of competitive peer-review process). Micro-focal sources are characterized by low emitted power, therefore an exposure time of the order of hours is required to collect sufficient statistics, which is too long for clinical and many other applications.

1.4.2 Bonse/Hart interferometry

A Bonse/Hart interferometer [35] [36] consists of three crystal blades, placed in the arrangement shown in Fig. 1.8.

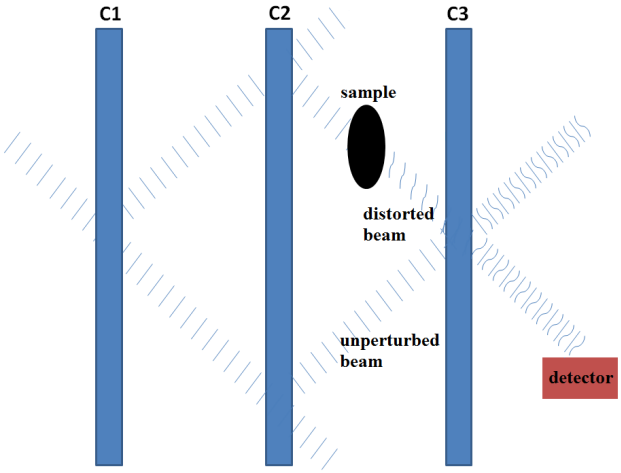

Figure 1.8: Bonse-Hart intereferometer.

The first crystal splits the X-ray beam in two by means of a symmetrical Laue reflection [35]. The second one deflects the two partial beams towards each other. The third one, placed where the beams meet each other, recombines them. At every interaction with the crystal blades (apart from the first one), one beam is discarded, thus not all

the initial X-rays are used. If an object is inserted along one of the two branches, the recombined beam will consist of the interference between the distorted beam that went through the object and the unperturbed one propagating along the other branch.
The method allows a full phase reconstruction of the imaged sample and is extremely precise [37], allowing also for the retrieval of quantitative phase contrast information for soft biological samples [38]. Further developments of the technique have been carried out by Momose [39] [40] and by Ando and his group [41] [42].
Nevertheless, the beam must be strictly parallel and monochromatic, which limits the use of this method predominantly to SR environments [18]. Moreover, the crystal blades must be positioned with a precision of the order of a fraction of the atomic distance with respect to each other, which makes the necessary alignment very difficult to obtain. A solution to this is achieved if the blades are produced by cutting a single crystal i.e. they are all attached to the same common base. Another downside is that the alignment of the interferometer itself respect to the direction of the incoming rays is critical, which makes the system very sensible to environmental vibrations and temperature changes [33].

1.4.3 Analyzer Based Imaging (ABI)

This approach exploits the narrow reflectivity curve of perfect crystals when they are illuminated by monochromatic radiation [43] [44]. This curve can be used to discriminate between X-rays deflected towards the detector or absorbed in the crystal, depending on how much they are deviated from their original direction.
Let us suppose the crystal is oriented in such a way that the primary, unperturbed beam hits it at the angle of maximum reflectivity (Bragg angle). When a sample is introduced, refraction occurs. Hence, photons deviated from their original direction by more than half the reflectivity curve width, will hit the crystal with an angle sufficiently different from the Bragg one, as to prevent them from being reflected towards the de-

tector. In other words, the higher the photon deviation (which is mostly pronounced along the edge of imaged details), the lower the fraction of X-rays redirected towards the detector and therefore the number of counts. The working principle of an analyzer crystal is shown in Fig. 1.9.

An interesting result is obtained by slightly rocking the crystal off the position of maximum reflectivity, e.g. by 50% of the rocking curve width. In this case, only half of the primary beam is reflected towards the detector. Due to the steep slope of the curve (called also *rocking curve*), a system with high sensitivity to small deviations in photon directions is obtained.

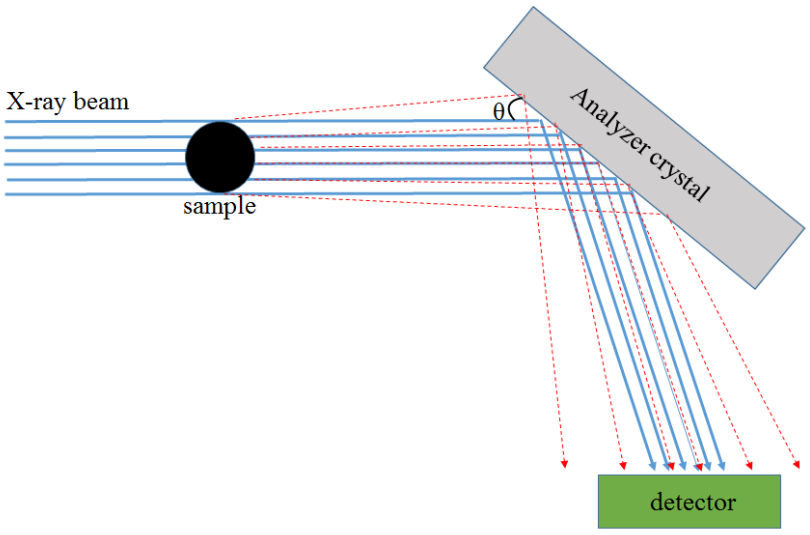

Figure 1.9: Working principle of Analyzer-based imaging.

Three cases can happen:

- **Photons not hitting** the sample or traversing a region of negligible phase gradient (leading to negligible deviation) will be deviated towards the detector (and so detected) with 50% of probability;
- **Photons deviated in one direction** (e.g. upwards) will hit the crystal at an

angle where the reflectivity is increased and therefore be redirected towards the detector with a higher probability. This causes a bright fringe to appear, typically along one edge of the sample;

- **Photons deviated in the opposite direction** (e.g. downwards) will hit the crystal at an angle at which the reflectivity is reduced, generating a dark fringe on the other side of the sample detail.

Objects transparent to X-rays (i.e. giving a very low absorption signal) can therefore become detectable thanks to their X-ray refraction properties. By using angles with a high misalignment, an image contrast higher than the one typical of FSP XPCi can be obtained [45, 46].

The method can be extended to CT [47] [48] and is suitable for several medical applications that include imaging of breast cancer specimens [49] [50], cartilage [51], *in vivo* on small animals [52] and many others.

On the downside, radiation must be strictly parallel and monochromatic. This is easily achieved only with SR sources, for which as said there is limited access. Other downsides are: high sensitivity to environmental vibrations and temperature changes; sensitivity to phase changes only in one direction due to the intrinsic properties of perfect crystals; delivery of extra radiation dose which is not used for image formation, because part of the primary beam is absorbed in the crystal instead of redirected towards the detector after it has traversed the sample.

1.4.4 Grating Based Imaging (GBI)

An alternative and efficient way to create phase contrast is given by grating-based methods, first introduced by J. Clauser [53]. The main idea is to create an X-ray interferometer exploiting the *Talbot self imaging effect*. The Talbot effect was first observed in 1836 by Henry Fox Talbot [54]. When a plane wave is incident upon a

periodic diffraction grating, the image of the grating is repeated at regular distances from the grating plane. These repeated images are called self images or *Talbot images*. Furthermore, at half these distances a self-image also occurs, which is phase-shifted by half a period. At smaller regular fractions of the typical Talbot distances, sub-images can also be observed, creating a fractal pattern often called the *Talbot carpet*.
The Talbot length z_t is expressed through the following formula:

$$z_t = \frac{\lambda}{1 - \sqrt{1 - \frac{\lambda^2}{\alpha^2}}} \tag{1.9}$$

where α is the period of the diffraction grating and λ is the wavelength of the light incident on the grating.
The simplest implementation of the interferometer [55],[56],[57], possible when coherent radiation is available, is made of two gratings. The first grating is placed immediately after the sample. It is made of a low absorbing material, and is used to create a periodic phase shift in the wave front: for this reason it is called *phase grating*. The *analyzer grating* is instead made of an absorbing material, and is used to analyze the interference pattern generated by the phase grating.
For the Talbot effect to occur, the phase grating must be illuminated by a coherent X-ray beam. The analyzer is placed at one of the Talbot distances, where the interference pattern generated by the X-rays passing through the first grating creates a self image of the grating itself. The introduction of the sample perturbs the interference pattern: these perturbations are then converted into intensity differences onto the detector, which is placed immediately behind the analyzer. In order to separate phase information from other contributions to the signal (such as absorption and ultra-small angle scattering), a technique called *phase stepping* is used. One of the gratings, typically the first, is scanned along the transverse direction over one period. The recorded intensity as a function of the step position produces a sinusoidal signal for each pixel.

By comparing this signal with and without the sample (which introduces perturbations), absorption, phase and scatter information can be retrieved.

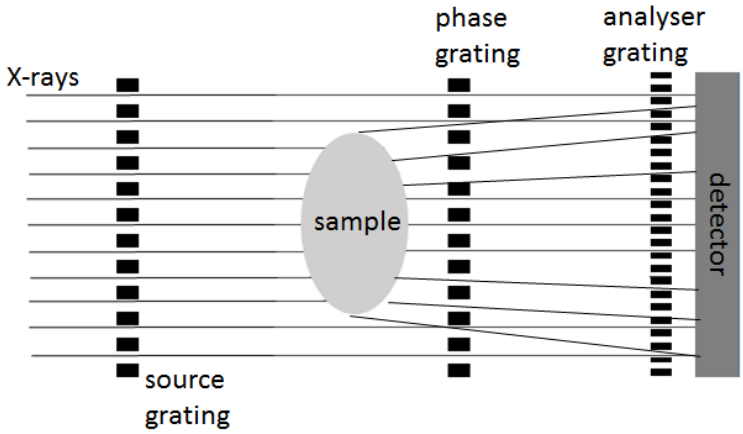

Figure 1.10: The Talbaut/Lau configuration used in grating interferometry.

By adding a third grating after the source, the Talbot-Lau configuration [58],[59] is obtained in order to increase the spatial coherence of the source, as shown in Fig. 1.10. The Talbot/Lau configuration allows the application of the method also to extended sources, because the third grating splits the original, spatially incoherent source into several mutually incoherent but individually coherent sub-sources. The method was also shown to tolerate a reasonable degree of polychromaticity ($\sim$10%) [55].

The method can be translated to CT [60] and allows to perform dark field imaging [59] by further extending the analysis based on the "phase stepping" curve previously mentioned. Together with the lateral shift and the intensity reduction of this curve caused by the introduction of the sample in the field of view, also a "dampening" of the oscillation is observed, which can be related to the dark-filed signal (i.e. multiple refraction in different directions caused by sample inhomogeneities too small to be resolved by the pixel). The method can also provide phase sensitivity to both orthogonal directions [61] [62].

The list of possible applications is fully described in the review paper by Pfeiffer et al.(2013) [63].

One downside of this method is given by the fact that the source grating is composed of channels much longer in the X-ray propagation direction than in the transverse one, and so it strongly collimates the X-ray beam. The net result is a reduction in the amount of X-rays emitted which actually reach the detector: this translates into low fluxes, and therefore into exposure times incompatible with real-world applications. If the third grating is eliminated, the method can work properly only with sources characterized by a high degree of spatial coherence, like SR (very expensive and with limited access) or micro-focal sources (with low emitted power, again implying long exposure times).

1.4.5 Edge Illumination

An innovative approach to X-ray phase contrast imaging is given by the edge illumination (EI) method, which was first developed at the Elettra synchrotron facility in the late '90, as an alternative to ABI that does not require the use of an analyser crystal [64].

Even though both GBI and EI methods use gratings, the way by which they produce phase contrast is different. In fact, whereas the former extracts information from interference patterns generated by coherent illumination of a phase grating and exploitation of the resulting self-image, the latter is non-interferometric and focuses only on refraction effects. In fact, EI gratings (that hereafter we will call "masks" to distinguish them from those used in GBI) have a period between one and two orders of magnitude larger than GBI ones, which prevents, at X-ray wavelengths, any interference effect from taking place. The basic idea behind the development of EI is that only the edges of the detector pixels illuminated by X-ray play an active role in the creation of the phase contrast signal. This technique was first introduced in the late nineties by using collimated and monochromatic synchrotron radiation [64].

A schematic side view of the EI setup is shown in Fig. 1.11. As can be seen, an X-ray beam is collimated by a first slit (called pre-sample aperture). Before impinging on the detector, part of the incident beam is stopped by an absorbing edge, placed in front of a row of detector pixels.

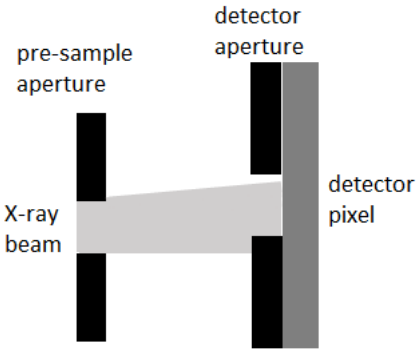

Figure 1.11: EI setup (side view showing a section along the direction perpendicular to the beam propagation).

When a sample is scanned along the direction perpendicular to the beam propagation, refraction effects will deviate the photons from their original path and several cases can happen, the two most notable being described in Fig. 1.12.

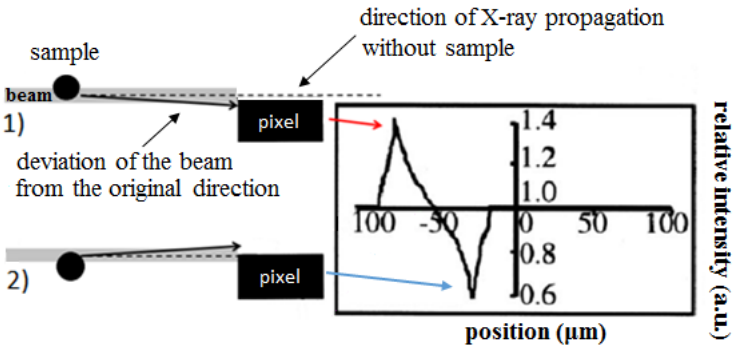

Figure 1.12: Image formation principle of "single beam EI ", in which the sample needs to be scanned along the direction perpendicular to the beam propagation).

In the first case, a fraction of the photons previously falling outside the active area of the pixels are deflected within it, increasing the number of counts respect to the background and contributing to the positive peak in the detected signal. In the second case, a fraction of the photons that previously fell inside the active area of the pixels are deflected outside it, decreasing the number of counts with respect to the background and creating a negative peak in the detected signal.

Another interesting aspect of this setup is that, the narrower the beam, the more intense the acquired signal. In fact, when the sample is scanned through the beam, photons within a narrower beam are more easily deviated inside/outside the detector surface: their contribution to the signal and to the contrast is thus more significant. Indeed, it has been shown [18] that, by progressively reducing the pixel illuminated fraction from 80% to 60% and then to 15%, the peak to peak signal in the intensity profiles of acquired images of wires increases from 7% to 12% and eventually to $\sim 40\%$, respectively. In comparison to the contrast obtained for the same sample with an absorption method ($< 1\%$), this leads to a contrast increase of almost two orders of magnitude.

Hence narrowing the beam in edge illumination increases the phase contrast, which means higher Signal to Noise Ratio (SNR) at the same dose, or equivalently same SNR at a lower dose. However, it also causes the elimination of a lot of photons from the original beam: this translates into a flux reduction, leading to an increased exposure time.

Another general problem of "single beam" EI, regardless of the beam cross section, is that it is necessary to scan the sample through the beam to obtain an image. A solution to this problem is obtained by using a set of apertures (which we will refer to as "masks"), which allows the acquisition of an image in a single shot, instead of scanning it through the beam, as is necessary with a single aperture. The method also enables applying EI principle to divergent X-ray beams.

A schematic of an EI system setup using multiple apertures [65] is shown in Fig.1.13.

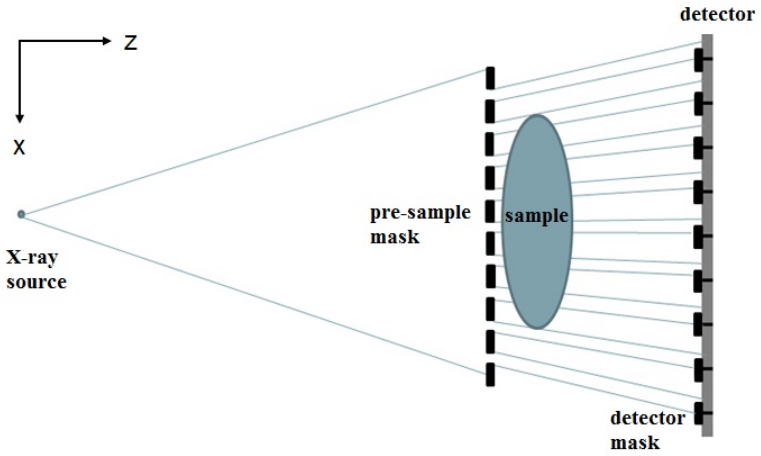

Figure 1.13: Laboratory implementation of the EI method, sometimes referred to as the "Coded aperture" system.

The **pre-sample mask** is placed just before the sample and is used to create an array of individual beams, each one impinging on the edge of an aperture on the detector mask. The beamlets created by this mask do not interfere with each other. Moreover, the mask prevents unnecessary radiation from reaching the sample, ensuring efficient dose delivery.

The **post-sample mask** (or detector mask) is placed in contact with the detector and is used to create insensitive regions between adjacent pixel rows (or columns).

One of the most important features in EI XPCi is the fact that phase sensitivity depends on the transition between sensitive and insensitive areas on the pixel. The sharper this transition, the higher is the phase sensitivity, leading to increased contrast for the same sample.

The ultimate image resolution obtained with this system is determined by the pre-sample aperture width (typically of the order of 10 μm). A dithering process [2] can be used to increase sampling and thus image resolution: for a given fixed displacement of the two masks, several images can be acquired corresponding to a series of sub-pixel sample displacements. These images can then be recombined, leading to an image with

a resolution determined by the dithering step.

The wide range of possible applications of Edge Illumination includes security scans [66] [67] [68], small animal imaging [69] [70], mammography [71], palaeontology [72], material science [73] and many others.

Phase sensitivity in two orthogonal directions is possible by using L-shaped pre-sample apertures instead of long slits, and aligning both sides of each L-shape to two orthogonal edges of the corresponding (square) detector apertures [74] [75]. However, the work presented in this thesis was mainly focused in applications involving 1D phase sensitivity, leading to the choice of masks with long slits.

EI has a series of practical advantages over GBI. While grating-based methods requires a very fine positioning of the gratings which must be placed at Talbot distances, the EI method is not affected by this problem. More generally, and also considering transverse directions and rotations, while the latter requires alignments of tens of nanometres, the former can tolerate a few μm. EI works well also with spatially incoherent sources, without the need of a source grating, because interference effects are not required to take place. Diverging beams are easily taken into account by scaling down the sample mask's dimensions according to the mutual distance between the masks. Fully polychromatic sources can be used.

One disadvantage of EI is that the increase in phase contrast signal achieved by illuminating smaller pixel fractions is translated into a longer exposure time required to achieve the same X-ray statistics, i.e. the same noise level in the image. Moreover, the number of photons needed to generate enough signal to noise ratio (SNR) is made lower by the enhanced contrast, leading to exposure times still compatible with medical applications.

For further details about image formation principles, see [76].

1.5 State of the art in the field of X-ray Phase Contrast imaging and novel contributions provided by this thesis work

As discussed in the previous sections, the field of X-ray imaging includes several methods and can be used for a wide range of applications.

Conventional X-ray imaging, which was the first method to be developed, is nowadays very well established in the medical field, as well as in industry and security. Nevertheless, its performance is compromised when used with materials showing low absorption properties, such as soft tissues [77]. Furthermore, the method was the subject of substantial innovations since the introduction of Computed Tomography (CT) [14, 15] and the use of digital detectors [13], dated back to the late 70's and 90's, respectively.

X-ray Phase Contrast imaging (XPCi) represents an important alternative, because it exploits the X-rays phase shift properties, which lead to stronger effects with respect to absorption ones (up to 3 orders of magnitude) for certain materials including tumours in soft tissues, cartilage, explosives, etc. The method shows a soft tissue sensitivity comparable with the one provided by Magnetic Resonance Imaging (MRI), but at the same time is faster (in terms of acquisition time), less expensive and provides a higher spatial resolution.

Free space propagation [20] is the most simple XPCi method, it does not require any alignment procedure (such as Grating Interferometry and Edge Illumination) and can tolerate a certain degree of polychromaticity [17]. However, it requires an X-ray source with a high degree of spatial coherence, which is achieved only at synchrotrons or by using micro-focal sources. Unfortunately, the former are very expensive and not easy to access, while the latter lead to excessively long exposure times because of the low emitted power.

Crystal interferometry [35] and analyzer-based imaging [46] can provide extremely high

image quality in several applications, but they are very sensible to environmental vibrations and they require monochromatic and parallel beams, which again are provided only at SR.

Grating Interferometry [57] and Edge Illumination [64] are the only Phase Contrast methods that can be efficiently adapted with laboratory sources [58, 78], i.e. they can work also under non ideal conditions such as polychromaticity, divergence of the beam and low spatial coherence. Even if both methods use gratings, they are based on two different mechanisms: the first one exploits the Talbot self-imaging effect [54] and is based on detecting interference patterns, while the second one is completely non interferometric and exploits only refraction effects [76]. Despite the wide range of applications in which both techniques are used (see respective sections), EI turns to be more robust against environmental vibrations and has higher tolerances in terms of alignment of the optical elements [79], [77], plus it does not require an additional source grating in order to work with laboratory sources. These advantages are the reason why our group focuses on this particular technique.

When I started my PhD in medical physics at University College London in 2013, EI systems made use of very bulky and heavy stepper motors to move optical elements [79] [80] [81]: this prevented the easy transportation of the setup to different scientific environments to test the method with novel X-ray sources available outside the UCL lab. My original contribution consisted in the development of a portable system, based on piezo-electric motors, capable to provide the same performance achieved so far with previous systems, but with a more compact setup.

In particular, I made a very careful selection of the type of motors needed for our applications, after establishing some important criteria such as maximum dimensions and weight, maximum tolerance for the positioning accuracy and costs. At the end, my choice was on the piezoelectric motors, because this technology can guarantee compactness, high motion accuracy (compatible with our requirements) and contained costs at

the same time.

I also developed a Labview code, used to drive the motors in an automatic way, and I integrated it with the data acquisition system, which I modified for my needs. After preliminary tests that I made in order to evaluate the positioning accuracy and the software procedure, I evaluated the angular sensitivity in refraction images acquired with both systems, in order to compare their performance.

Another important contribution of my work consisted into facilitating the realization of more cost-effective setups. At present, X-ray sources used so far by the group at UCL are characterized by a very high flux and by focal spots which, although they are not microfocal, they are sufficiently small to meet EI requirements [80], however they are very expensive. For this reason, I developed a newithreminds the Talbot-Lau configuration used in Grating Interferometry [59] [59], in the latter case the source grating is used to increase spatial coherence (necessary condition for the Talbot effect to take place and be exploited), while in EI it is simply used to section the large focal spot of a more cost-effective, conventional X-ray tube. By using deconvolution algorithms [82] to restore the images generated with this configuration, I demonstrated, via a proof-of-concept experiment, that the approach is viable and allows the use of cheaper X-ray sources and at the same time to reduce the overall system length by a factor of 2.

At present, EI setups make use of system lengths of 2 m (a part from microscopy applications[83] and beam tracking approaches [84], in which 1 m lengths were used), which allow the achievement of very good performance in terms of angular sensitivity and image contrast. However, the impact of a reduction in the overall system length on the angular sensitivity has never been studied in detail. For this reason, I carried out a quantitative study on this subject, with the main aim of realizing more compact EI setups that might be preferable for applications in which the available space is limited. The study consisted in evaluating the angular sensitivity in refraction images obtained by using different source-to-detector distances, while keeping the same sys-

tem magnification and exposure time. In order to do this, I compared results from a simulation which considered only the presence of Poisson-distributed noise with those obtained with an experiment that I carried out with an integrating detector. The simulated results showed that, with a photon counter detector, the angular sensitivity does not change with the source-to-detector distance: this allows to choose a system length that is more suitable for the specific application (e.g. longer systems might be beneficial when dose must be kept to a minimum, because the reduced flux does not affect the sensitivity and hence the image quality). On the other hand, experimental results with an integrating detector showed that the sensitivity gets worse with the source-to-detector distance, suggesting that more compact systems might be preferable with respect to longer ones in the same conditions (i.e. magnification, exposure time and tube settings), unless the source power can be changed in order to compensate the flux loss at longer distances. However, for applications in which dose is an issue, longer setups are preferable and would require the use of a photon counter.

My last contribution consisted in evaluating the performance of the EI method when adapted to new generation X-ray sources such as a laser plasma source, which can in principle provide synchrotron-like radiation but with a more compact and easily accessible setup. A preliminary Phase Contrast proof-of-concept experiment showing promising results was already performed with this source [85], but only with a FSP setup (i.e. without any optical elements between X-ray source, sample and detector). By considering the capability of EI to achieve nanoradian angular sensitivity when combined with highly spatial coherent sources [80], the adaptation of EI with a laser-plasma source is expected to provide important results. Unfortunately, due to instability of the laser, I was able to perform only a characterization of the source, which I used to establish some important requirements that must be fulfilled in order to guarantee an acceptable performance.

In summary, my personal contribution to the research group I worked with and, more in

general, to the field of X-ray Phase Contrast imaging, consisted in further expanding the possibilities of adapting the EI method with both laboratory and "non conventional" X-ray sources. A particular attention was given to the development of implementations involving portable, compact and cost-effective setups, towards the translation of the method into real-world applications.

2

Design and realisation of a portable Edge Illumination X-ray Phase Contrast imaging system

As well as a possible first step towards translation into real world applications, the capability of EI to work with polychromatic, divergent and incoherent X-ray beams can provide the wider scientific community access to phase contrast imaging techniques with laboratory sources. The method can be implemented with virtually any X-ray source technology. However, its performance is inescapably related to the source characteristics: in particular, the angular sensitivity of the method is considerably enhanced when implemented with highly coherent sources such as synchrotrons [86]. Since novel X-ray sources are being developed in various labs in the UK and worldwide, it is important to develop a portable and compact system that enables the easy transportation of the setup.

At present, the optical elements used for EI experiments are aligned by means of rather heavy (few Kg) and bulky (several tens of cm) motors, which make the system diffi-

cult to transport. To solve this limitation, I developed a portable system based on miniaturised and highly precise piezoelectric motors. In comparison with the stepper motors used so far, the piezo-motors are characterized by an even higher accuracy in the positioning, and in addition are lighter and compact. Their small dimensions (few cm) and the limited load that they can support ($\sim$ 1 Kg) make these motors suitable in particular for small and light samples, while stepper motors might be preferable when a higher robustness is required.

Several tests, described in this chapter, showed that the portable system is capable to obtain the same performance as the one achieved by previous systems, but with a more compact and flexible setup.

In this chapter we will describe the realisation of the portable system, with particular reference to the motors design and the LabView software that I specifically implemented to drive and integrate them with the pre existing Data Acquisition System.

Results of the preliminary tests that I performed to evaluate the accuracy of the motor positioning will also be discussed.

Finally, we will show a comparison of wire images of different materials that I acquired with both the previous system and the portable system. The results, published as a note in the journal Review of Scientific Instruments (RSI) [87], showed that the angular sensitivities of both systems are comparable within the experimental error. Specifically, this analysis revealed an angular sensitivity of (270 $\pm$ 6) nrad, which compares well with the (260 $\pm$ 10) nrad reported for systems based on stepper motors. This allows for the realization of more compact EI setups without affecting the phase sensitivity, and it facilitates the translation of the method into real-world applications.

The results can also be considered a test of the performance of the piezo-motors, and as such could be of interest to researchers planning their use in other imaging systems.

2.1 Materials and methods

The aim was to develop a portable, light and compact system that could be easily carried to different scientific environments (e.g. x-ray imaging facilities, centres for biomedical diagnostics, university laboratories). The masks were mounted on stacks of motors to allow for accurate alignment and movement. These motor stacks must be smaller and lighter than those used in the previous system, while maintaining the same motion accuracy. To remotely control the devices, I developed a dedicated LabView code and I integrated it into the existing DAQ software via a TCP/IP connection.
Motors constitute an essential part of EI setups because they are used in several procedures which require movements along different directions. Examples of these procedures are mask alignment, illumination curve acquisition and sample dithering[79].

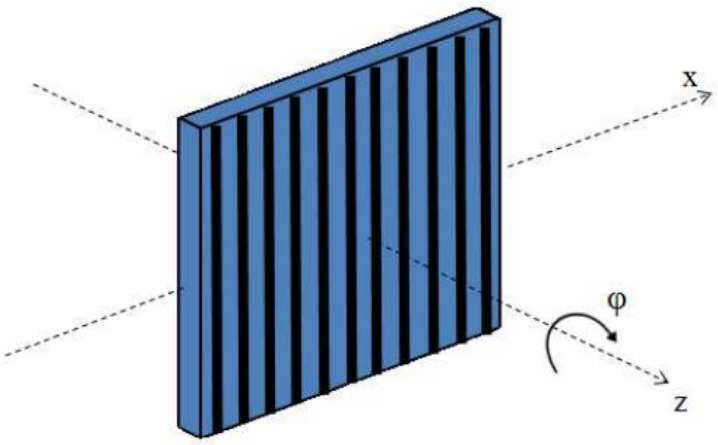

Figure 2.1: Required movements for the masks, where z is the beam propagation direction.

Mask alignment is carried out every time a new setup is implemented. Each setup is characterized by its own specific set of parameters such as, for example, pitch and aperture width of the masks, distance between them, spot size of the x-ray source, detector pixel size, etc. The two masks (one placed just before the sample and one

placed just in front of the detector) must be aligned along the optical axis in such a way that their projected pitches both match the detector pitch. Moreover, apertures in both masks should be parallel to each other. In principle, the full alignment procedure requires an adjustment of all six degrees of freedom, but stricter tolerances are required for translations along x and z directions and rotations by the angle ϕ[79] (Fig. 2.1).

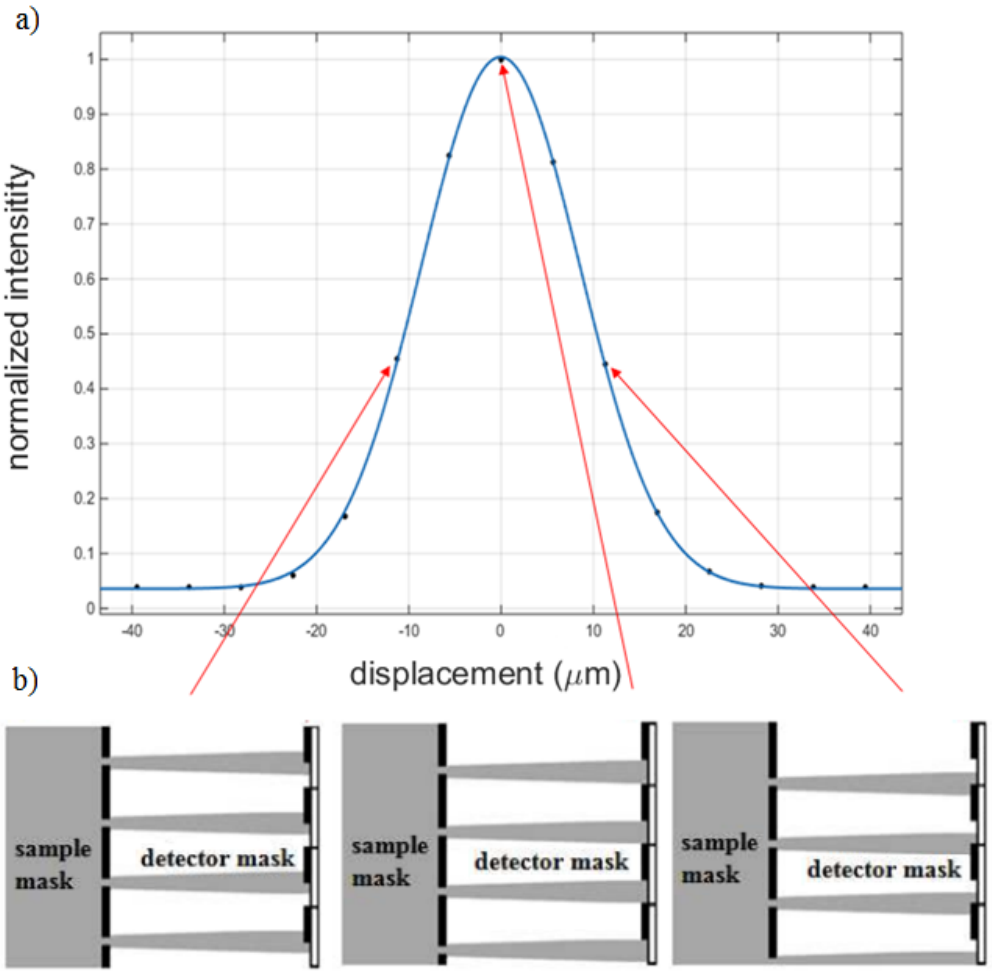

Figure 2.2: (a): illumination curve; (b): pre-sample mask positions corresponding to specific points on the curve, as indicated by the arrows.

The illumination curve is the variation of the detected intensity as a function of the displacement between the two masks along the transverse direction x. Its measurement

involves a procedure during which the sample is taken out of the field of view, while the pre-sample mask is shifted in several steps along the x direction (see Fig. 2.1), resulting in different illumination levels for the detector pixels. At each mask displacement, the intensity of the radiation impinging each pixel is recorded, leading to an intensity profile similar to the rocking curve in analyzer based imaging [88]. The experimental points can be fitted with a gaussian function in order to extract its characteristic parameters (amplitude, centroid and standard deviation). By comparing the values of the illumination curve with and without the sample, a dedicated algorithm can be used to retrieve information about absorption, refraction and ultra small angle scattering generated by the sample [89].

Fig. 2.2 shows an example of illumination curve, as well as three mask displacements corresponding to three different points on the curve.

The dithering procedure consists in the acquisition of multiple images at several subpixel displacements of the sample along the direction orthogonal to both the beam propagation and the mask apertures (direction x in Fig. 2.1), with a total travel range that corresponds to one mask period. All these images are taken while keeping the relative displacement between the two masks fixed, i.e. at the same illumination level. These images are then recombined to obtain one with increased spatial resolution (determined by the dithering step, rather than by the pixel size[2, 90]).

The choice of the motors took into account important criteria such as motion accuracy, dimensions, weight and costs, as discussed in the next section.

2.1.1 Design criteria

All the three procedures discussed above require motion accuracy of about half a μm for translations and a few μrad for rotations [79]. The positioners used so far for EI experiments match the requirements for the motion accuracy, but are quite heavy and

bulky, with a weight of few kilograms and dimensions of several tens of centimetres. This feature prevents the easy transportation of the setup and can hinder the construction of compact setups such as required by some applications such as small animal or specimen imaging.

For this reason, the main criterion behind the choice of the new motors was the necessity to fit all the basic elements of the EI setup (masks, motors and corresponding control units, laptop and accessories like posts, holders, screws, etc.) into a compact (a few tens of centimetres) and light (a few Kg) case.

As hinted above, the another important criterion was enabling the realization of more compact setups with reduced overall system lengths, as required by some applications. At present, the footprints of the stepper motors used so far in standard EI implementations do not allow to reduce the system length to dimensions below 1 m.

Furthermore, provided that the motors fulfilled the two above criteria (i.e. compactness and lightness of the whole setup), it was also important to verify that they could guarantee a motion accuracy compatible with the requirements of our method, especially regarding the maximum tolerances accepted for the aligning procedures [79].

On this bases, the most obvious choice was offered by motors based on piezoelectric technology, which allows to fulfil all the above criteria at the same time (summarized in the scheme in Fig.2.3).

Even though different stepper motors were checked, which could possibly be available at even lower costs, their dimensions and weight were not compatible with the first two criteria. For this reason, devices manufactured by SmarAct and based on piezoelectric technology were chosen for the portable system, which makes the motor stacks compact, light and with a motion accuracy compatible with our requirements.

Selection Criteria	Required specs
Fit the whole system in a compact and light case with overall dimensions and weight of few tens of *cm* and a few *Kg*, respectively.	**Max dimensions** of each single motor and control unit: a few *cm*. **Max weight** of the motors and control units: a few hundreds *g*
Allow for the realization of more compact setups with inter-distances between optical elements down to a few *cm*.	**Max dimensions** of each single motor: a few *cm*.
Guarantee a positioning accuracy compatible with EI requirements.	**Max tolerance for translations**: half µm **Max tolerance for rotations**: a few µrad

Figure 2.3: Selection criteria

2.1.2 The motor stack design

Each positioner is only a few centimetres high, and weighs a few hundred grams.

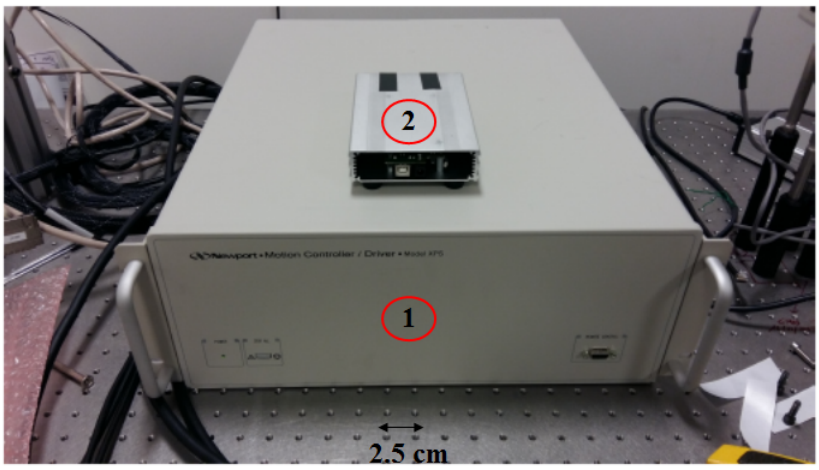

Figure 2.4: Comparison of Newport (1) and SmarAct (2) control units.

Furthermore, the control units of SmarAct motors are several times smaller and lighter than those used for Newport, as shown in Fig. 2.4, which compares the dimensions of

the two control units.

Fig.2.5 compares the dimensions of the stack based on Newport stepper motors (used so far in our research group) and the new one based on SmarAct piezo-motors.

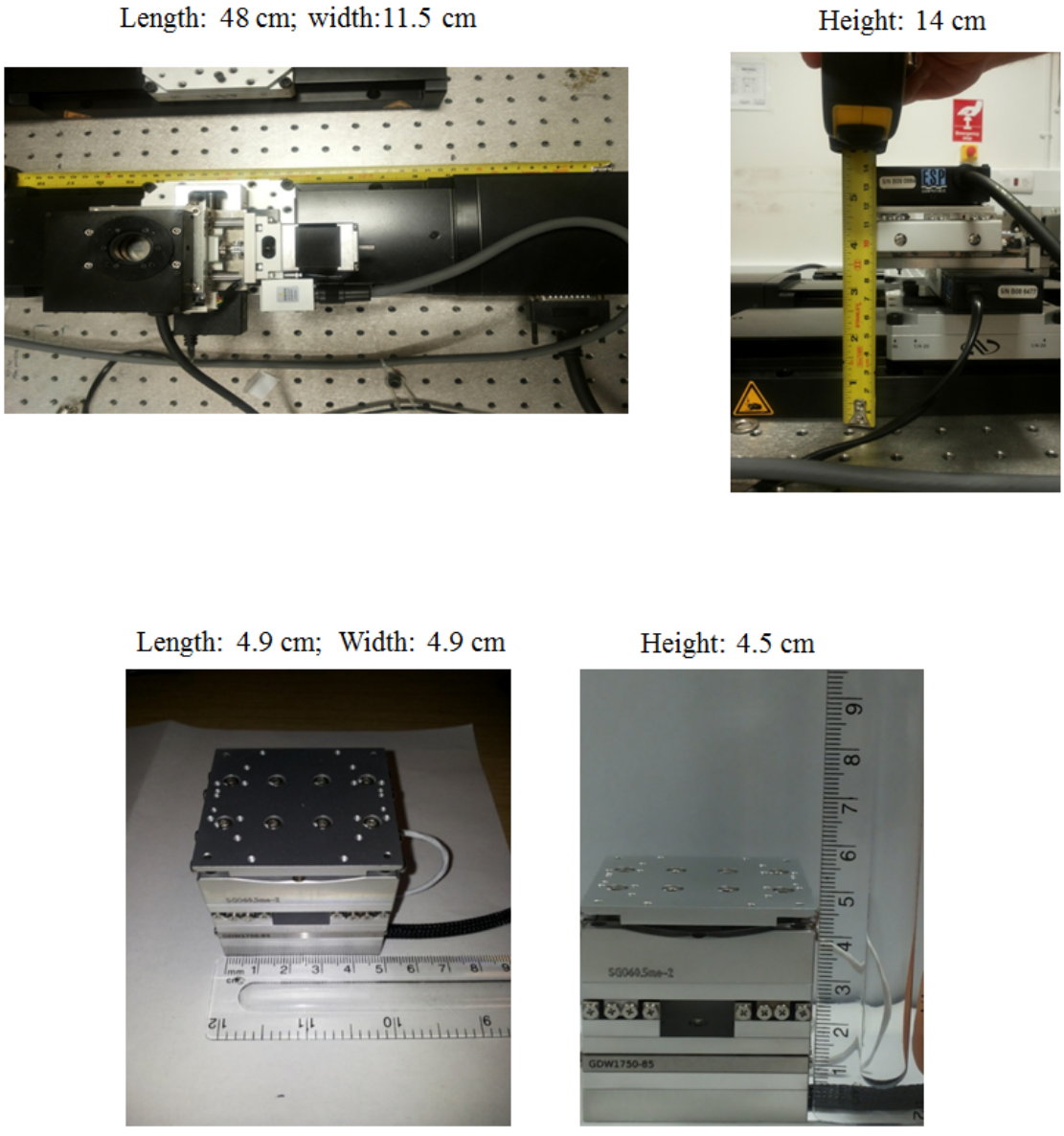

Figure 2.5: Dimensions of Newport stepper motors (top) and SmarAct piezo-motors (bottom).

The specs of the SmarAct positioners were carefully checked in order to meet the key requirements of compactness, lightness and high accuracy in the positioning. In order to have the possibility to place objects in and out of the field of view (for sample and flat field images, respectively), it was necessary to use a positioner with a long travel range. Furthermore, the smallest distance involved in the sample movement during the dithering procedure (described in the previous section) is typically of the order of a few microns. Therefore, it was decided to use a SmarAct SLC-24120 linear translator with a travel range of $\pm$ 41.5 mm and equipped with a microsensor characterised by a closed loop resolution of 0.1 μm and a bi-direction repeatability of $\pm$ 0.5 μm. The principal specs of this device are shown in Fig. 2.6.

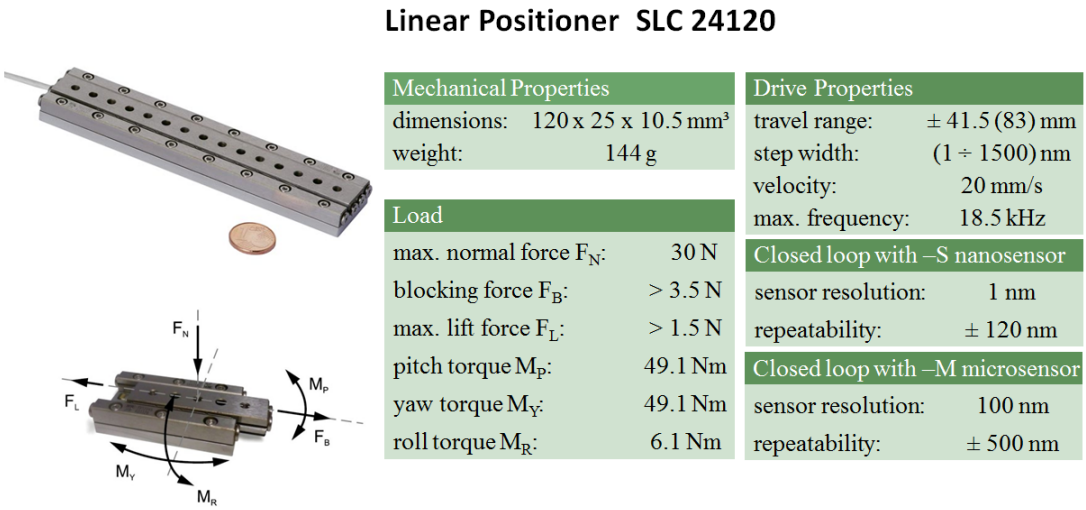

Figure 2.6: Principal specs of a linear translator SLC 24120-M-E with a microsensor [1].

A stack of motors was instead required to move the optical masks in several directions. Specifically, for the sample mask we used an SLC 1750-S linear translator equipped with a nanosensor. This choice is due to the highest motion accuracy which is required when the sample mask is moved in a closed loop positioning (performed during image acquisition). The detector mask movements do not require such an high accuracy,

because they are performed only for the preliminary mask alignment, which does not involve any closed loop procedure (the position can be adjusted by the user over several attempts). For this reason, an SLC 1750-M-E was used for the detector mask. Fig. 2.7 shows the specs of a SmarAct linear translator SLC 1750 for translations and a goniometer SGO-60.5 for rotations around the optical axis.

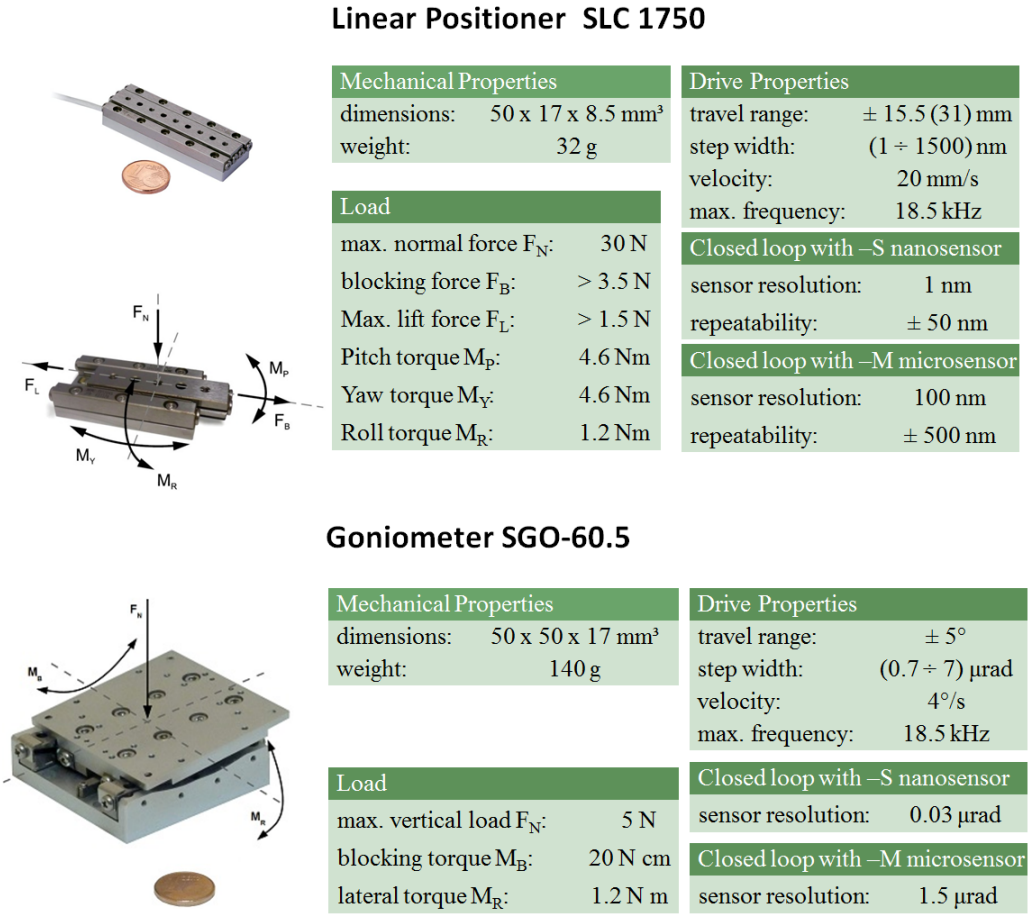

Figure 2.7: Principal specs of a linear translator SLC 1750 and a goniometer SGO-60.5 [1].

From the mechanical properties reported in Fig. 2.7, it can be noted that a linear translator is characterized by dimensions of a few centimetres and a weight of only 32 grams, which makes it very compact and light. The travel range is ± 15.5 mm, which is suffi-

cient to cover the typical distances required for mask alignment. The maximum vertical load the device can sustain is 30 N ($\sim$ 3 Kg), which is enough for the weight of the mask and the mask holder. Depending on whether a nanosensor or a microsensor is used for closed loop positioning, the sensor resolution can be 1 nm or 100 nm respectively, with a correspondent repeatability of $\pm$ 50 nm and $\pm$ 500 nm. The goniometer is also very compact and light (only few centimetres in dimensions and 140 g in weight). It has a travel range of $\pm$ 5 °, which is compatible with maximum rotation angles involved for mask alignment ($\sim$ 1°). If equipped with a nanosensor (microsensor), the resolution is 0.03 μrad (1.5 μrad).

According to the specifications that I provided (number of devices for each stack, travel range, motion accuracy and sensor resolution of each device), two stacks of motors were designed and assembled by the SmarAct company.

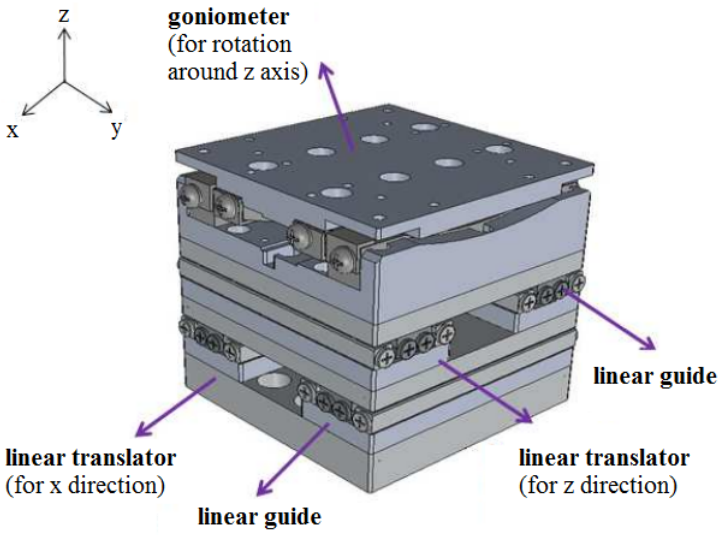

Figure 2.8: Design of the SmarAct motor stack, used to move optical masks along several directions.

Fig. 2.8 shows the design of a single stack of motors, which enables translation along

the x and z axes and a rotation around z. The full compact system is composed of:

- A SLC 24120-M-E linear translator, used to move the sample. The motor is equipped with a microsensor for closed loop positioning.
- A stack of three motors (two SLC 1750-M-E linear translators and a SGO 60.5-M-E goniometer) equipped with microsensors, used to move the detector mask.
- A stack of three motors (two SLC 1750-S linear translators and a SGO 60.5-S goniometer) equipped with nanosensors, used to move the sample mask.

2.1.3 The Control System

In order to drive the motors in an automatic way during the data acquisition, I developed a control system based on a LabView code that I wrote and interfaced with both a GUI and a TCP/IP connection.

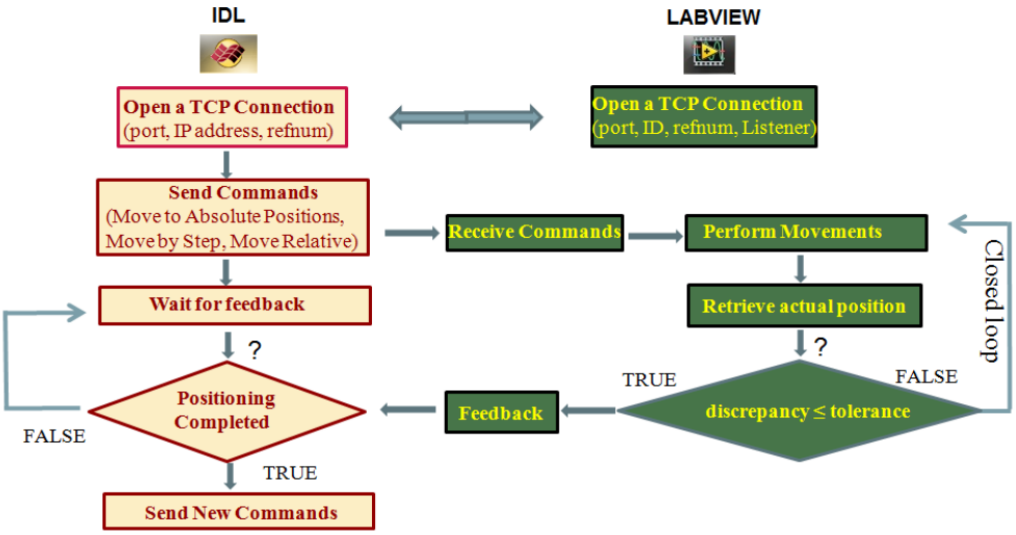

Figure 2.9: Basic operations and routines performed by the IDL/Labview code.

Commands can be sent using two methods: via a Labview GUI interface, which allows the operator to move the motors to absolute or relative positions directly, or via an IDL script (incorporated into the pre-existing DAQ system written in IDL) that enables the automated control of the motors during an acquisition.
The flow diagram in Fig. 2.9 shows the basic routines that I implemented in the hybrid IDL/Labview code. Once the TCP/IP connection is opened, several commands are sent from IDL (e.g. move the "n" motor to a given absolute position). Once the command is received by LabView, it is forwarded to the"n" motor and its actual position is retrieved using the attached sensor. In order to increase the positioning accuracy, I implemented a closed loop procedure: the code evaluates the discrepancy between the target position and the one retrieved by the sensor, and adjusts it until this becomes smaller than a certain tolerance; at this point, the IDL script moves on to the next command.

2.2 Preliminary tests

As already mentioned, when the motors receive the command to move to an absolute position, a small discrepancy is observed between the target position and the one retrieved by the sensor. For this reason, I implemented a closed loop positioning routine to adjust the motors movement after a maximum number of iterations. In order to evaluate the accuracy of the positioning during the closed loop procedure, I carried out several tests on both motor stacks (the one equipped with microsensors and that equipped with nanosensors), as described in the next session.

2.2.1 First detector mask motor stack

The first test was conducted on the motor stack equipped with microsensors and used to move the detector mask. The closed loop procedure consisted in the following steps:

- with the motor in an initial reference position "0", the command *go to absolute position* was sent by the user in order to reach a certain *target* position.
- the micro sensor attached to the motor was used to retrieve the actual position, in order to evaluate the discrepancy between the latter and the target position (in a closed loop positioning the expected value should be consistent with 0, within the experimental error);
- these two operations were repeated n times (where n is of the order of 1000), while varying the initial and target position, for a fixed step and direction of motion. In this way, it was possible to test the closed loop procedure with a certain step while covering a large range of arrival positions.

The entire procedure was then repeated with different steps (1μm, 10μm), for a given direction. After each set of acquisitions, a statistical analysis was performed on the observed discrepancy as a function of the iteration number n, by looking at its distribution, related mean and standard deviation.
Since both linear translators of the first motor stack have the same features, only measurements carried out for one of them are reported in Figs.2.10,2.11,2.12,2.13,2.14,2.15 for different steps and both directions.
We found that the distributions of the discrepancy between expected and retrieved positions had mean values consistent with 0, with standard deviations between 130 and 200 nm: these values are comparable to the nominal sensor resolution of 100 nm.
Tests on the goniometer are not reported because they are not essential for our purposes: this device is used only for the preliminary alignment procedure, which is not automated and does not need any closed loop positioning.

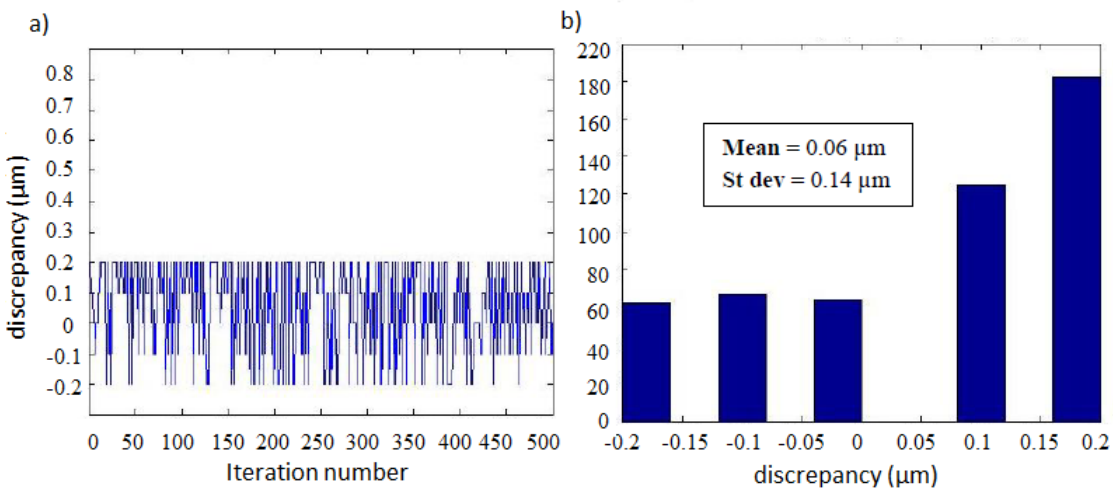

Figure 2.10: Plot(a) of the discrepancy values as a function of the iteration number, with the corresponding distribution(b) shown in histogram, for step = 1 μm and forward direction.

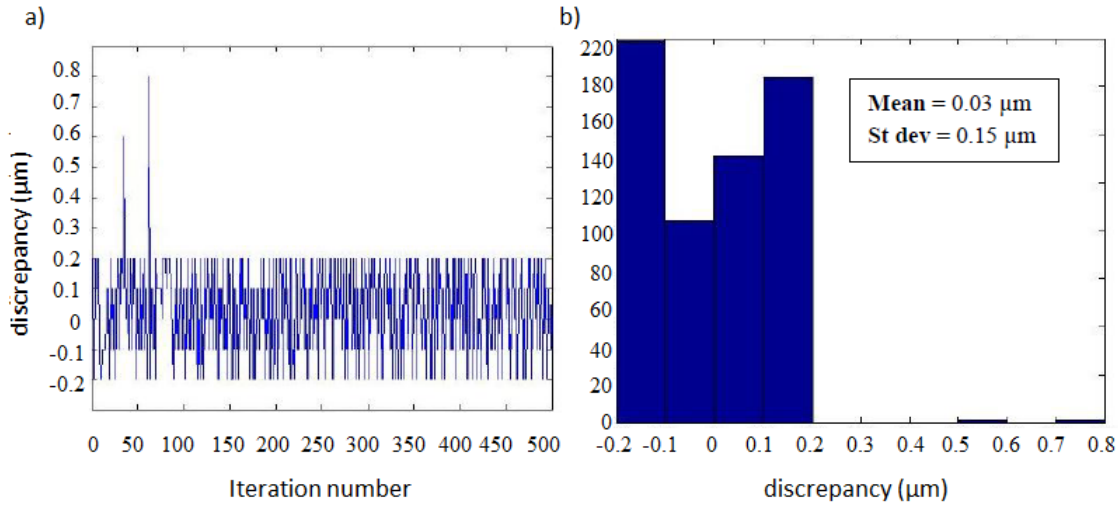

Figure 2.11: Plot(a) of the discrepancy values as a function of the iteration number, with the corresponding distribution(b) shown in histogram, for step = 1 μm and backward direction.

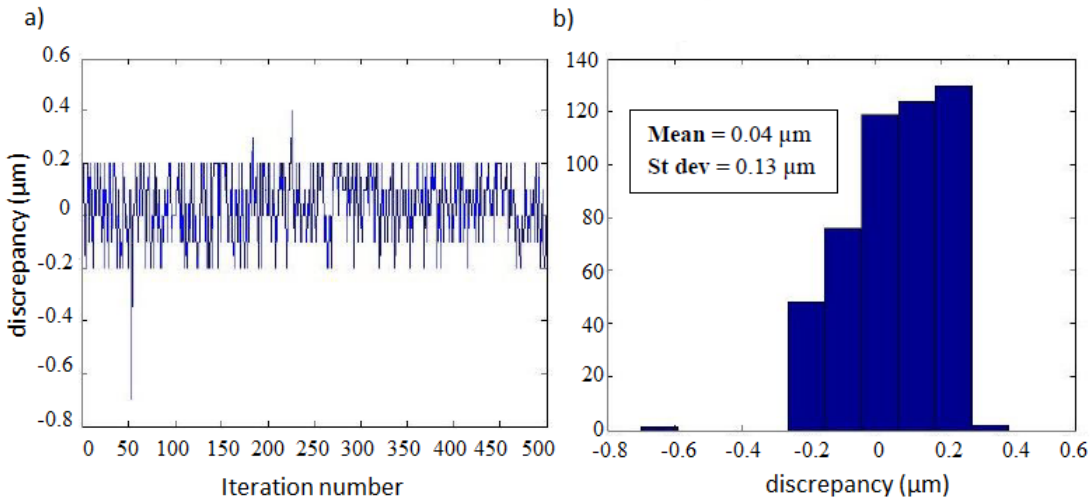

Figure 2.12: Plot(a) of the discrepancy values as a function of the iteration number, with the corresponding distribution(b) shown in histogram, for step = 10 μm and forward direction.

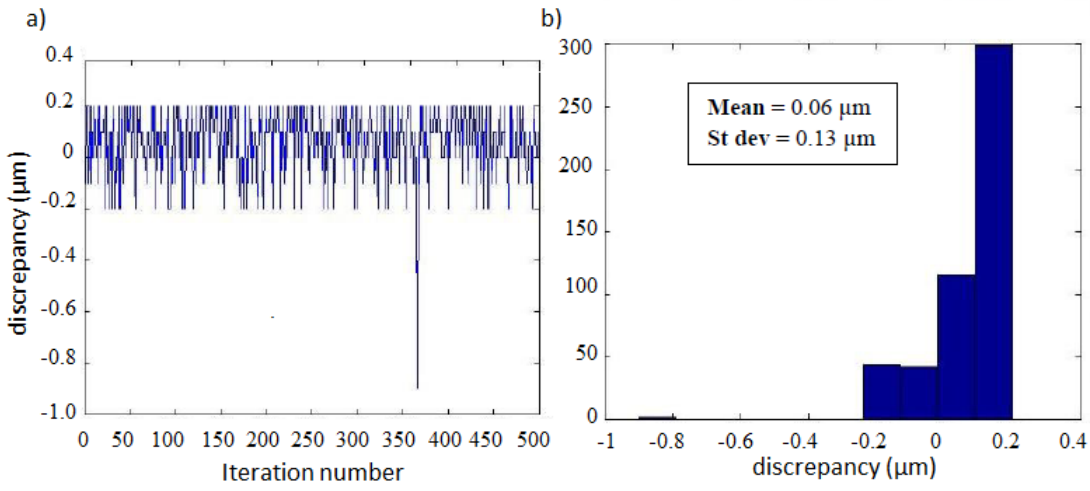

Figure 2.13: Plot(a) of the discrepancy values as a function of the iteration number, with the corresponding distribution(b) shown in histogram, for step = 10 μm and backward direction.

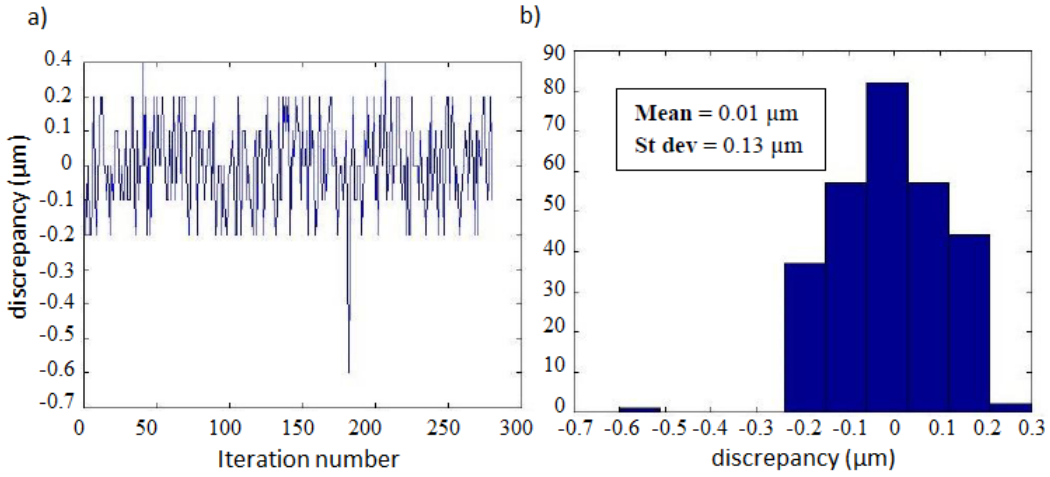

Figure 2.14: Plot(a) of the discrepancy values as a function of the iteration number, with the corresponding distribution(b) shown in histogram, for step = 100 μm and forward direction.

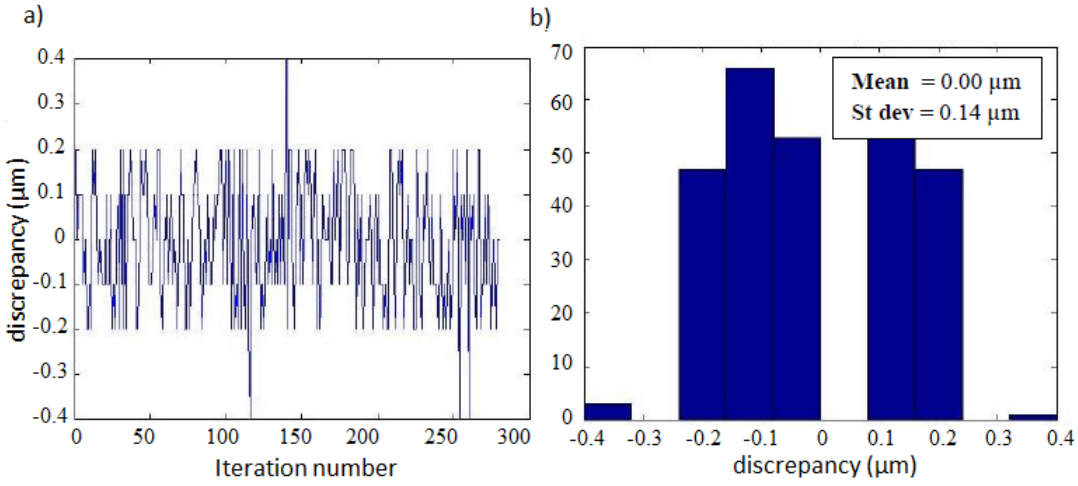

Figure 2.15: Plot(a) of the discrepancy values as a function of the iteration number, with the corresponding distribution(b) shown in histogram, for step = 100 μm and backward direction.

2.2.2 Second sample mask motor stack

According to nominal values provided by the manufacturer, SmarAct positioners equipped with microsensors have a bi-directional repeatability of ~ 1 μm. As a consequence, each time a motor is moved to a certain position from different starting points, it can make an error of up to 1 μm. This can affect the level of illumination expected for a given mask position (i.e. specific point on the illumination curve), which can therefore be different at each new acquisition. Hence, it was decided to use a motor stack with nanosensors to move the pre-sample mask with higher repeatability and accuracy compared to those of the motor stack described in the previous section, for which the requirements were less demanding.

As the control unit of motors based on nanosensors is based on Labview libraries which are different from those used for the previous stack, I developed a new Labview code. Furthermore, I repeated the testing procedure described in the previous section to characterise accuracy and repeatability of the new stack. The results showed that the accuracy of the motor procedure was comparable to the nominal sensor resolution of 1 nm, meaning that the motor converged to the target position in most of the cases. This should guarantee sufficient accuracy for the mask motion, and therefore a more reliable phase retrieval procedure.

2.3 Imaging tests

After the preliminary tests, I carried out an experiment in which I acquired images of wires of different material and thickness, using both the previous system based on stepper motors and the new portable system based on piezo-motors, in order to compare their performance.

Fig.2.16 shows the experimental setup based on the new portable EI system.

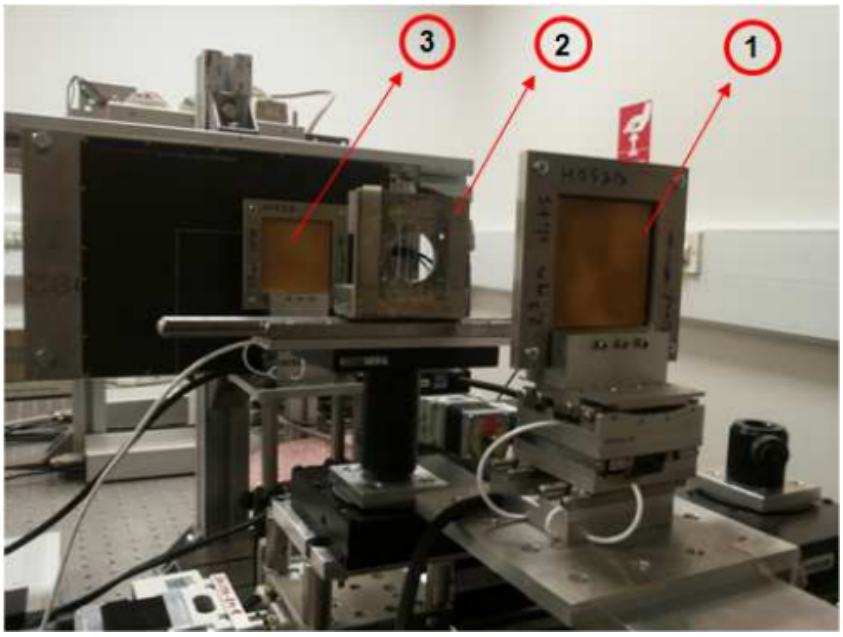

Figure 2.16: EI portable system based on piezo-motors: (1) is the sample mask, (2) the wire sample and (3) the detector mask.

The sample mask (labelled with (1) in the figure) was supported by a holder attached to the SmarAct motor stack equipped with nanosensors. The wire sample (2) was fixed on top of the Smaract SLC-24120 linear translator characterized by a travel range of 8 cm and equipped with a microsensor: this enabled to move it in and out of the field of view for flat field acquisitions. Materials and thicknesses of the wires were: sapphire (300 μm diameter), boron (200 μm with 14 μm diameter tungsten core), nylon (100 μm diameter), PEEK (150 μm diameter), MAXIMA (300 μm diameter). The latter is a trademark mixture of plastic polymers used to manufacture fishing lines. The detector mask (3) was mounted on the SmarAct stack with microsensors: this was moved only during the initial alignment procedure and kept fixed during the acquisitions.
The X-ray source was a Rigaku MM007 X-ray tube with a Mo target operated at 35 kV and 25 mA, with a spot size of 75 μm. The detector was the Hamamatsu C9732DK flat panel with a 50 μm pixel size. The masks, designed by Creatv MicroTecg Inc.(Potomac,

MD, USA) were made of electroplated gold of 150 μm thickness on to a 500 μm thick graphite substrate. The aperture width and the pitch of the pre-sample mask were 23 μm and 79 μm, respectively. The detector mask had an aperture width of 29 μm and pitch of 98 μm. The source-to-detector distance was 2 m, with a source-to-object distance of 1.6 m and an object-to-detector distance of 0.4 m, resulting in a magnification of 1.25.

For each set of acquisitions, I processed the raw data with a dedicated reconstruction algorithm that enables to retrieve absorption, refraction and scattering signals from three input projection images [89]. The algorithm assumes that the X-ray beam, after passing through the sample, is attenuated (by absorption), shifted (by refraction) and broadened (by ultra-small angle scattering). This can be described by the equation

$$\frac{I(\bar{x})}{I_0} = (O * L)\,(\bar{x} - \triangle x_R) \cdot t \tag{2.1}$$

where $I(\bar{x})$ and $L(\bar{x})$ are, respectively, the intensity recorded by a detector pixel and the illumination level corresponding to the mask displacement $\bar{x}$. I_0 is the beam intensity before passing through the sample, while t, $\triangle x_R$ and $O(x)$ represent, respectively, transmission through the sample, beam shift caused by refraction and scattering. The symbol $*$ denotes convolution.

By assuming that both *L(x)* and *O(x)* can be expressed as a linear combination of Gaussian functions, the following system can be derived [89] in the case in which three images I_i are acquired with different mask displacements x_i and only one term (N,M=1) is used for each function and:

$$I_i = t\frac{A}{\sqrt{2\pi\sigma^2}} exp\left[-\frac{(x_i - \triangle x_R)^2}{2\sigma^2}\right],\ i = 1, 2, 3 \tag{2.2}$$

By knowing the three (acquired) images I_1, I_2, I_3, the system can be analytically solved for t, $\triangle x_R$ and σ^2, allowing to separate contributions to absorption, refraction

and scattering.

Following this procedure, I acquired each projection image with different sample mask displacements corresponding to different positions on the illumination curve, typically one at the centre (corresponding to 100% intensity), and the other two at 50% intensity on opposite sides. In order to increase the spatial resolution, I acquired 6 dithering steps for all three images, with 5 sec exposure time for each step. Since the EI method is based on detecting the refraction of x-rays passing through the sample, the following analysis is focused on this aspect.

The retrieved refraction signal and the corresponding profile along a row of detector pixels, obtained using the previous, stepper motor-based system, are shown in Fig. 2.17 and Fig. 2.18, respectively. The equivalent results for the new portable system are shown in Fig. 2.19 and Fig. 2.20, respectively.

In the refraction image, the standard deviation of a rectangular area where no sample is present provides an estimation of the background noise in the image. Since this is a retrieved image in which pixel content represents the magnitude of the refraction angle of that point, this represents the *angular sensitivity* of the system (at a given detected statistics), i.e. the lowest refraction angle that can be resolved under those conditions [80]. This metric can be used to make a quantitative comparison between the two setups. Hence, I measured the angular sensitivity for both the SmarAct system and the Newport one, which were respectively (270 ± 6) *nrad* and (260 ± 10) *nrad*: the two values are thus comparable within experimental uncertainty. This important result shows that the use of piezoelectric motors for EI setups allows the method to keep the same performance as that of previous systems based on stepper motors. At the same time, it also enables the realization of more compact and light setups, more suitable for transportation, thus allowing easy tests of the EI technology in different environments and with different X-ray sources.

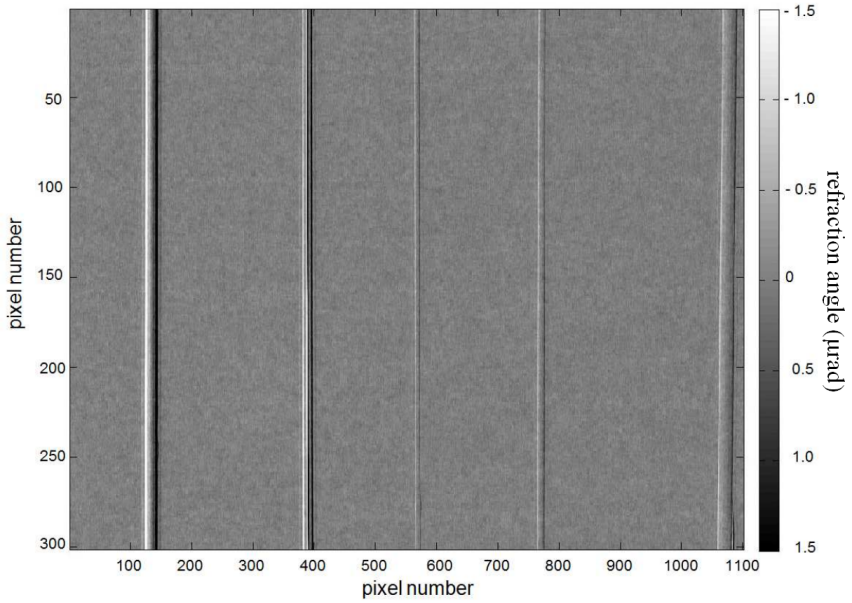

Figure 2.17: Refraction image obtained with the "old" stepper motor system.

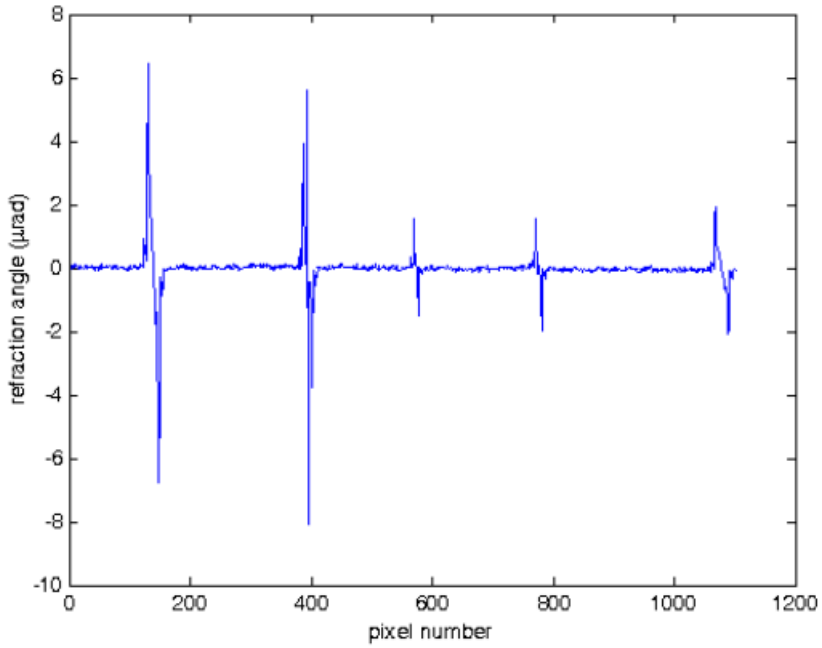

Figure 2.18: Profile of the refraction signal along a row of detector pixels, extracted from the image in Fig. 2.17.

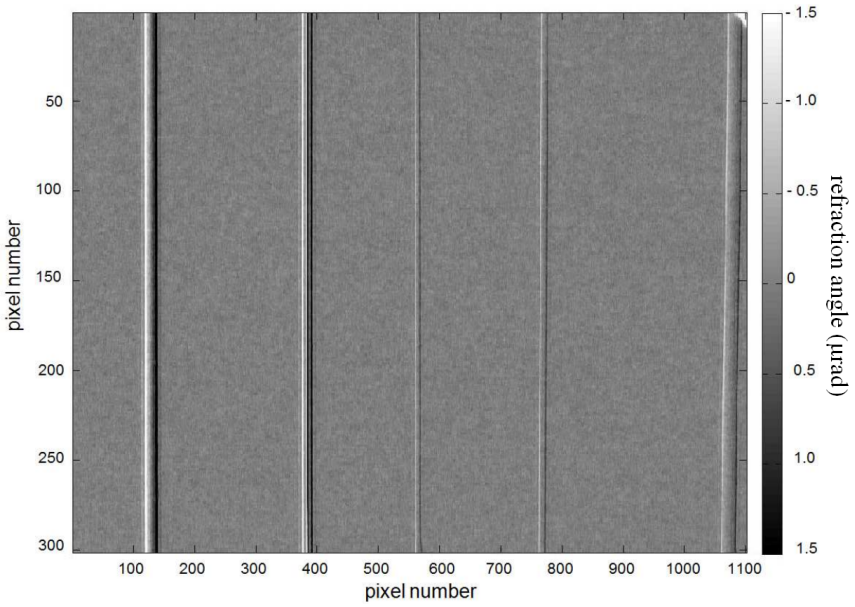

Figure 2.19: Refraction signal obtained with the new portable system.

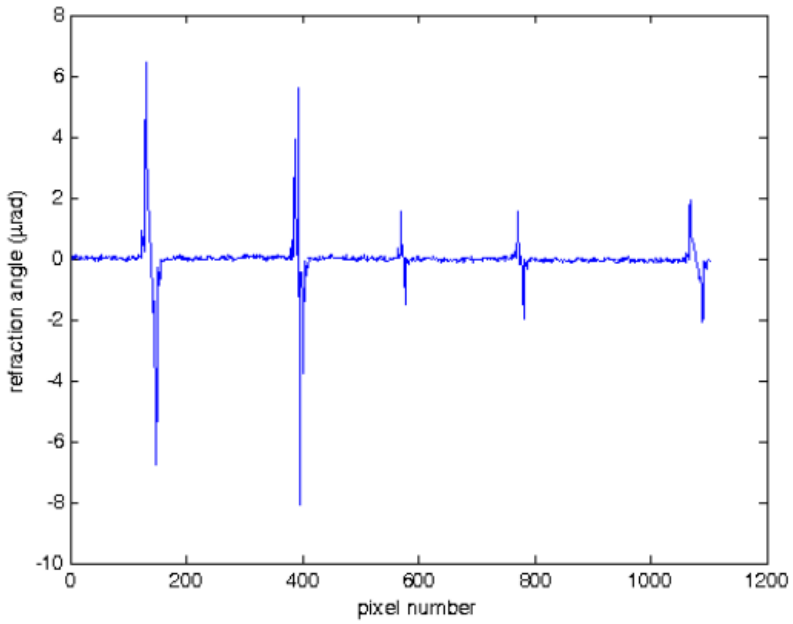

Figure 2.20: Profile of the refraction signal along a row of detector pixels, extracted from the image in Fig. 2.19.

2.4 Conclusions

The design and realization of a portable EI system for XPCi has been presented. The basic components are precise and miniaturised piezo-motors, which allow the motion of optical elements with high accuracy. The motors are compact and light, which makes the setup easily transportable to different scientific environments.

A dedicated control system based on LabView was implemented to drive the motors in an automated way, and to finely adjust their positions via a closed loop approach through their built-in sensor. The code was then integrated with the data acquisition software, and run on a laptop to guarantee the portability of the entire system.

Preliminary tests allowed the evaluation of the performance of the software procedure when moving the motors to absolute positions. The discrepancies between expected and retrieved positions were compatible with the nominal sensor resolutions.

The performance of the portable system was then quantitatively compared with that of the old system based on stepper motors, by acquiring images of the same sample with both, and applying the same phase retrieval procedure. Specifically, the angular sensitivity of the refraction signal was extracted for both systems from images of wires of different material and thickness. This provided an estimation of the smallest deviation angle detectable with both setups: for the portable system, a value of (270 $\pm$ 6) nrad was obtained, while the previous system led to a value of (260 $\pm$ 10) nrad.

Therefore, it can be concluded that a lighter and more compact system based on piezo-electric motors can be realized while maintaining the same sensitivity to angular deflections as obtained so far with bulkier systems based on stepper motors.

An important benefit of such a system is that it enables the easy transportation of the EI setup: this provides the possibility to test the performance of the method with novel X-ray sources that are being developed worldwide and, for this reason, are available outside the UCL lab. As we will see in Chapter 5, this feature has been decisive for the realization of a proof-of-concept experiment involving the adaptation of the portable EI setup with a laser-plasma source recently developed at the Strathclyde University in Glasgow, Scotland.

As we will discuss more in details in Chapter 4, an other important benefit of the portable system, compared to other EI systems used so far, is to allow the realization of extremely compact setups that require to place the sample and the two optical masks at distances of only a few centimetres from each other: such configurations, whose implementation might be very useful in clinical applications where available space is very limited, are not possible with the bulky stepper motors used so far in EI.

These features, together with the flexibility of EI and its capability to be adapted to various types of laboratory sources, extends the potential of the method and can simplify its adaptability to a wide range of real-world applications such as imaging of soft tissue specimens, small animals, digital histology and material science.

3

Lab-based edge-illumination X-ray phase contrast imaging with a structured focal spot

3.1 Introduction

The potential of X-ray Phase Contrast imaging (XPCi) has been widely explored over recent years, especially in applications where low-absorbing materials are imaged. While XPCi methods such as crystal interferometry [35], analyzer-based imaging [46] and free-space propagation (FSP) [20] provide excellent performance, their high coherence requirements have restricted their use to synchrotron environments (or microfocal x-ray tubes), therefore limiting their commercial translation. Instead, grating interferometry [57] and edge illumination (EI) [64] can both be adapted to conventional laboratory sources [58, 78]. Our group has been focussing on the latter, for reasons related to its full achromaticity [91], compatibility with non-microfocal lab-sources without requiring a source grating [78, 92], and tolerance to misalignment/vibration of the optical elements [79, 93].

Full details on the image formation principles in EI can be found in Refs. [76, 94].
While non micro-focal sources can be used, the basic principle of EI requires that the beamlets created by the pre-sample mask do not mix [65], which still imposes a degree of limitation on the maximum focal spot that can be used. The projected focal spot convolved with the magnified aperture in the pre-sample mask must lead to a degree of smearing largely contained within a single pixel. For this reason, EI setups currently under development at University College London use high-powered x-ray sources (e.g. Rigaku M007) which, while being an excellent match with EI requirements [80] due to their capability to generate high fluxes from focal spots around 70-100 μm, are high-end scientific instruments and therefore not particularly cost effective, which could be an aspect to consider in terms of commercial translation. Moreover, with the exception of targeted microscopy experiments [83], overall setup lengths so far ranged between 1.5 and 2 m [65].
In this chapter an alternative implementation of the EI method that simultaneously allows the use of cheaper x-ray sources, and the realisation of more compact setups are presented. In particular, the basic elements that constitute the new EI setup are described, with particular reference to a newly introduced "source mask" and its function.
The basic principles underlying image formation with this specific configuration are also discussed, together with the analysis that I carried out on the dependence of dithered and non-dithered intensity profiles on the source spatial distribution (in particular when passing from a single X-ray source to the three sources created by the source mask). This study was conducted by using a wave optics simulation code [3] that I suitably modified in order to take into account source distribution, the characteristics of the new source-mask (i.e. gold thickness, pitch, apertures) and the specific geometry of the system.
Finally, in order to validate this idea, the results of a proof-of-principle experiment

(published in Applied Physics Letters (APL) [95]) that I carried out in collaboration with my colleagues of the Phase Contrast Imaging Group at UCL, are presented. These show that the proposed approach is viable by demonstrating that deconvolving differential phase-contrast image profiles that I acquired with three separate sources, provides results in agreement with simulated predictions for equivalent profiles generated by a single source. It is also shown that this enables reducing the system length from the 2 m used so far to 1 m.

3.2 The setup

Fig. 3.1 shows a schematic of the new EI setup.

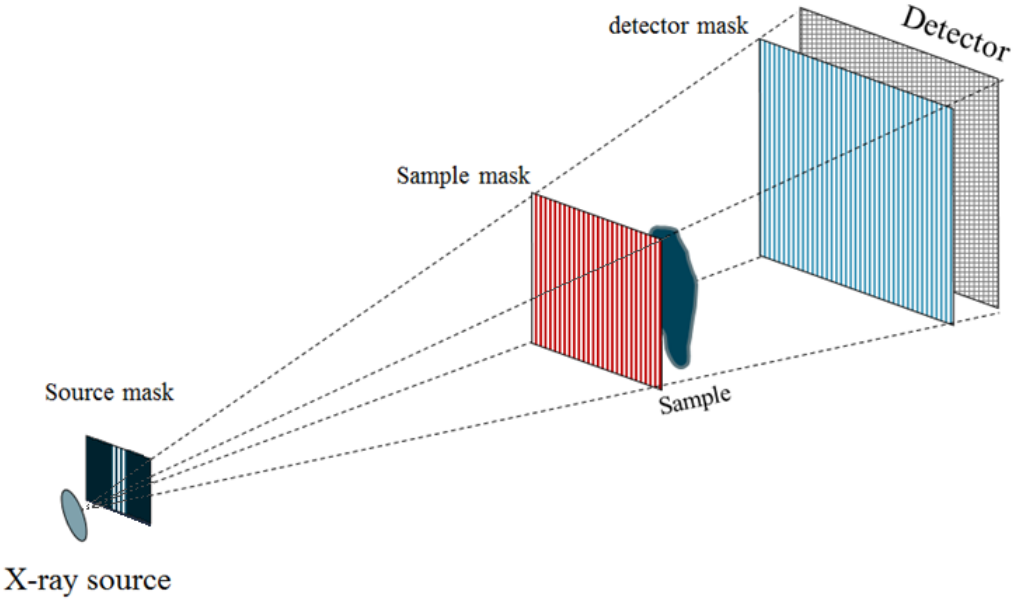

Figure 3.1: Schematisation of the EI setup that makes use of a source mask.

It is based on the introduction of a third x-ray mask, in close proximity to the source,

analogous to the introduction of the "source grating" in Talbot-Lau grating interferometry setups [58] (shown in Fig. 1.15 of Chapter 1).

However, two significant differences should be noted between the two configurations. First, in grating interferometry the source grating is used to increase coherence. Conversely, EI is an incoherent XPCI method [92, 96], and maintains this key characteristic also in this new implementation: the apertures in the source mask are large, and their only function is to allow the use of a much larger focal spot, since this could provide a more cost effective way to generate a sufficiently high x-ray flux. While in principle source apertures as large as 70-100 μm could be exploited, we used smaller apertures in this proof-of-concept experiment (17 μm), because we wanted to simultaneously investigate the possibility to reduce the overall system length. The angular sensitivity decreases with increased focal spot (above a given threshold) and reduced propagation distance [80]. The latter has a direct influence on the overall system length, due to the need to limit the dimensions of the projected focal spot. Hence, the use of a smaller source should offset that of a reduced system length, while maintaining the same sensitivity. It should be noted that the apertures were still sufficiently large as to not generate any noticeable coherence effect.

The second key difference from the Talbot-Lau method has to do with the effect that the source mask has on the acquired images. The one-to-one relationship between apertures in the sample/detector masks and detector pixels means that the use of multiple sources results in the generation of a plurality of images shifted by one pixel with respect to the other, with the number of images matching the number of sources. This is exemplified in Fig. 3.2 for the 3-source case.

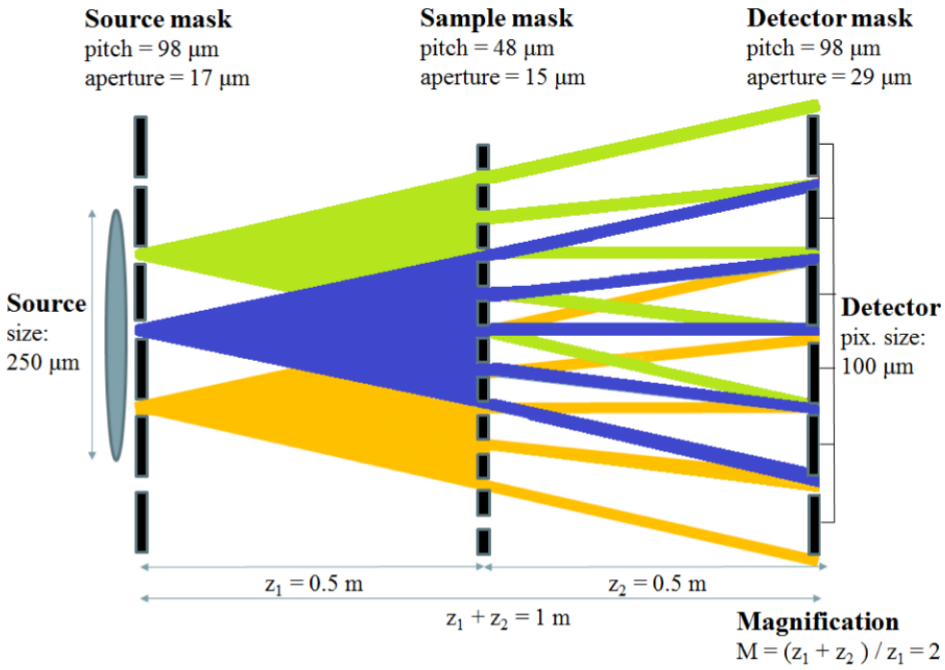

Figure 3.2: Schematisation of the new EI setup. Different colours have been used for different sub-sources defined by an individual aperture in the source mask. Each one creates an image shifted by one detector pixel with respect to its neighbours. While the illumination of five pixels from each source is displayed for demonstration purposes, this actually extends over the entire field of view.

3.3 Image formation principle

Making reference to Fig. 3.2, the intensity *I(i)* recorded by the *i-th* detector pixel is given by the contribution of the three sources, and can be expressed by the following relationship:

$$I(i) = \sum_{n=-1}^{1} I_n(i), \tag{3.1}$$

where n indicates the source number (0 being the central one) and $I_n(i)$ is the intensity produced by the *n-th* source in the *i-th* pixel. Under the hypothesis that all sub-sources have the same shape but are just laterally shifted one respect to the other, $I_n(i)$ is equal to the intensity $I_0(i-n)$ produced by the central source in the *(i-n)*-th

pixel. Equation (3.1) can then also be written as:

$$I(i) = \sum_{n=-1}^{1} I_0(i-n). \tag{3.2}$$

By exploiting the properties of the Kronecker delta $\delta_{i(n-j)}$, we can write Eq. (3.2) as:

$$\begin{aligned} I(i) &= \sum_{n=-1}^{1} \sum_{j} I_0(j)\delta(i-n-j) = \\ &= \sum_{j} I_0(j) \sum_{n=-1}^{1} \delta(i-n-j), \end{aligned} \tag{3.3}$$

by taking into account that the sum over j index is independent from the sum over n. By defining a Discrete Source Distribution (DSD) as $DSD(i) = \sum_{n=-1}^{1} \delta(i-n)$ and exploiting the definition of discrete convolution, we can write:

$$I(i) = \sum_{j} I_0(j) DSD(i-j), \tag{3.4}$$

which shows that the intensity in the *i-th* pixel is given by the discrete convolution of the intensity I_0 produced by one source in the center of the distribution and the *DSD*. We explored the validity of the approach discussed above through a combination of simulation work and a proof-of-concept experiment, both described in the next sections. The results were then compared to check the agreement between theory and experiment.

3.4 The simulation framework

In order to carry out a preliminary study on how the number of sources affects the intensity profile of test samples, I used a simulation code based on a wave optics model. The code, implemented in Matlab, was developed by Vittoria et al [3] and allows to simulate an Edge Illumination system (shown in Fig. 1.19 of the Introduction) as a

series of free space propagations and transmissions through various objects (e.g. masks and sample).

Free space propagation between the source and the sample mask and between the two masks can be described by means of Fresnel diffraction integrals [17, 19, 20]. By using the *paraxial approximation* (i.e. considering only waves the propagation direction of which forms a small angle with respect to the optical axis), it can be shown [3] that the complex amplitude of the electromagnetic field on two planes z = z_A and z = z_B can be described by:

$$\psi_B(x,y) = \psi_A(x,y) * H_{\triangle z}(x,y) \tag{3.5}$$

where z is the propagation distance, $\triangle z = z_B$ - z_A, $*$ indicates the convolution operation, and H_z is the Fresnel propagator:

$$H_z(x,y) = \frac{exp(ikz)}{i\lambda z} exp\left(ik\frac{x^2+y^2}{2z}\right) \tag{3.6}$$

The transmission through an object (which can be one of the masks or the imaged sample) can be described by:

$$\psi_{out}(x,y) = T_{obj}(x,y)\psi_{in}(x,y) \tag{3.7}$$

where $T_{obj}(x,y)$ is the complex transfer function of the object, while $\psi_{in}(x,y)$ and $\psi_{out}(x,y)$ are, respectively, the complex amplitude of the incoming and outgoing fields. For an ideal mask, $T_M(x,y) = 1$ within the apertures and $T_M(x,y) = 0$ in the absorbing septa.

For the sample, $T_{obj}(x,y)$ is given by:

$$T_{obj}(x,y) = exp\left[-ik\int_0^z \delta(x,y,z')dz'\right] exp\left[-k\int_0^z \beta(x,y,z')dz'\right] \tag{3.8}$$

where the integral is taken along the sample thickness z.

The code allows taking into account different setup parameters, such as system magnification, distances between the optical elements, aperture width, pitch and thickness of the masks, detector pixel size, etc. Finite source sizes and pixel crosstalk are also taken into account by convolving the signal produced by a point source with the projected source distribution and the detector PSF, as described more in detail in Ref. [3].

The code has been tested and extensively used for several EI applications [97], [98], [99].

In this specific case, the simulation was adapted to the new system geometry described in Fig.3.1. In particular, the presence of the three sub-sources was taken into account in the code by implementing an appropriate source distribution as a series of three rectangular functions, with weights matching those that were measured experimentally. This "triple source distribution" was then convolved with the signal generated by one central source.

Example results obtained by using this simulation framework are provided for a wire sample with a diameter of 400μm. In Fig. 3.3, both "undithered" (Figs. 3(a) vs 3(b)) and "dithered" (Figs. 3(c) vs 3(d)) intensity profiles of EI differential phase-contrast images are shown. As already discussed in the previous chapters, with "dithering" I refer to a procedure in which the spatial resolution in the final image is increased by re-combining multiple frames acquired while the sample is displaced by sub-pixel positions [2, 65, 90].

In this case, 6 sub-pixel steps were used. As can be seen, while going from a single source to three sources simply broadens the peaks in the undithered profiles (Figs. 3(a) vs 3(b)), the effect is markedly different in dithered ones. In the latter case, the use of three sources results in three distinct positive and negative peaks: these are effectively three separate image profiles, each one created by one of the three "sourcelets" shifted by the number of dithering steps. However, images equivalent to those created by a single source can be restored by inverting Eq. (3.4), which can be done by means of

a deconvolution procedure. In this case, I used the Richardson-Lucy algorithm with a total variation regularization [82], as explained more in detail in the next section.

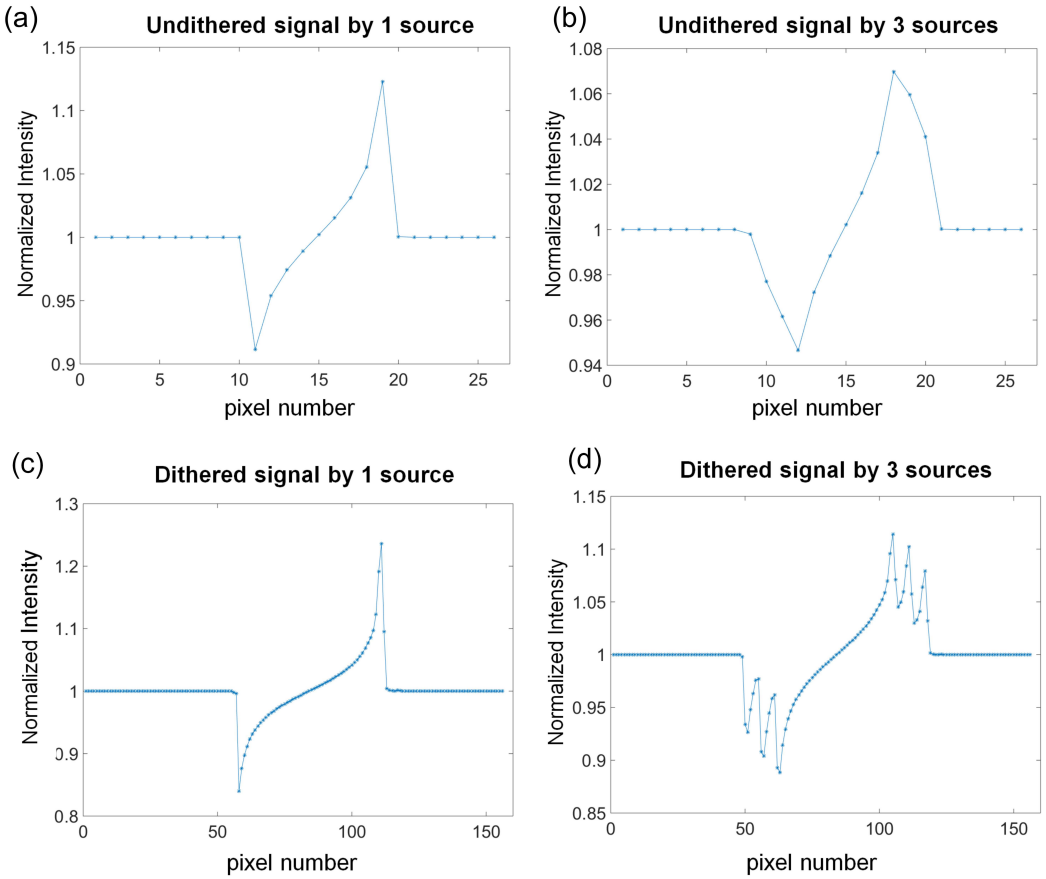

Figure 3.3: Comparison between simulated intensity profiles of EI differential phase-contrast images of a wire sample, generated by using one source (a,c) and three sources (b,d); (a) and (b) represent "undithered" profiles; (c) and (d) "dithered" ones. In the labels of the horizontal axes, we refer to "image" pixels, rather than physical detector pixels: these correspond to the detector pixel size in undithered images, and to detector pixel size divided by the number of dithering steps in the dithered ones. Note also that the signal intensity is higher in the dithered cases, thanks to the finer sampling of the peak near its maximum value [2]. For all plots, the intensity normalised through division by the number of counts in the background is plotted as a function of the pixel number.

3.4.1 The Richardson-Lucy algorithm

Deconvolution methods are used to restore the signal O that was degraded by the convolution with the point-spread function PSF of an imaging system. In general, the recorded signal I can be described by:

$$I = O * PSF \tag{3.9}$$

where the symbol $*$ denotes convolution.

In the ideal, noise-free case, if the PSF of the system is known (or at least some assumptions can be be made on its form, based on the system geometry), the original image O can be deterministically recovered by inverting Eq. 3.9. However, in the real case, the recorded signal is affected by noise, so that Eq. 3.9 becomes:

$$I = O * PSF + N \tag{3.10}$$

where N is the noise described by the appropriate distribution.

Usually, the choice of the best deconvolution algorithm is determined by the specific application and by the user requirements. More specifically, a compromise should be obtained among the quality of the final image, the quantitative correctness of the solution and the available computational time [100]. *Non-iterative methods* such as regularized inverse-filtering [101] and Wiener filtering algorithm [102] are faster if compared to *iterative* ones such as Richardson-Lucy(RL) [82] and constrained Tikhonov-Miller [103], but they often fail to provide optimal image quality, especially in the presence of noise [104]. For this reason, I decided to use the iterative Richardson-Lucy algorithm, which is one of the most commonly used in literature [104] [105] [106]. However, as iterative deconvolution processes are affected by noise amplification when converging to the exact solution [107], I also used a regularization procedure in order to stop the process af-

ter a certain number of iterations. Even though some regularization procedures such as Tikhonov-Miller [108] or maximum entropy [109] avoid noise amplification, they can excessively smooth the object edges, which instead play a crucial role for the signal formation in EI. For this reason, I decided to use the total variation (TV) regularization method [107], which enables to preserve the sharpness of the edges and at the same time keep noise to a limited level.

Hence, the acquired images were deconvolved by using the following iterative Richardson-Lucy algorithm with TV regularization, as described by Dey et al [107]

$$O^{s+1} = \left(\frac{i}{O^s * PSF} * P\tilde{S}F \right) \cdot \frac{O^s}{1 - \lambda div\left(\frac{\bigtriangledown O^s}{|\bigtriangledown O^s|} \right)} \tag{3.11}$$

where O^s and O^{s+1} are respectively the restored (deconvolved) images at the s^{th} and $(s+1)^{th}$ iteration, and λ is the regularization parameter used to stop the process after a certain number of iterations. Further details about the derivation of the algorithm can be found in ref. [104].

3.4.2 Effect of the relative intensity of the sub-sources on illumination curves and images

Considering the case in which three sub-sources are created through the source mask, a new simulation was run in order to study the effect of their relative intensity on the illumination curve, the dithered images of a wire and the corresponding intensity profiles. As expected, the relative intensity of the sources does not affect the shape of the illumination curve. Its standard deviation, in fact, depends only on the source size, the aperture width and the mutual distance between the three sub-sources, which are all kept constant in the simulation.

Conversely, both the dithered images and the corresponding intensity profiles are affected by the source distribution, as already discussed in the previous section and shown

in Figs. 3.4, 3.5, 3.6, 3.7.

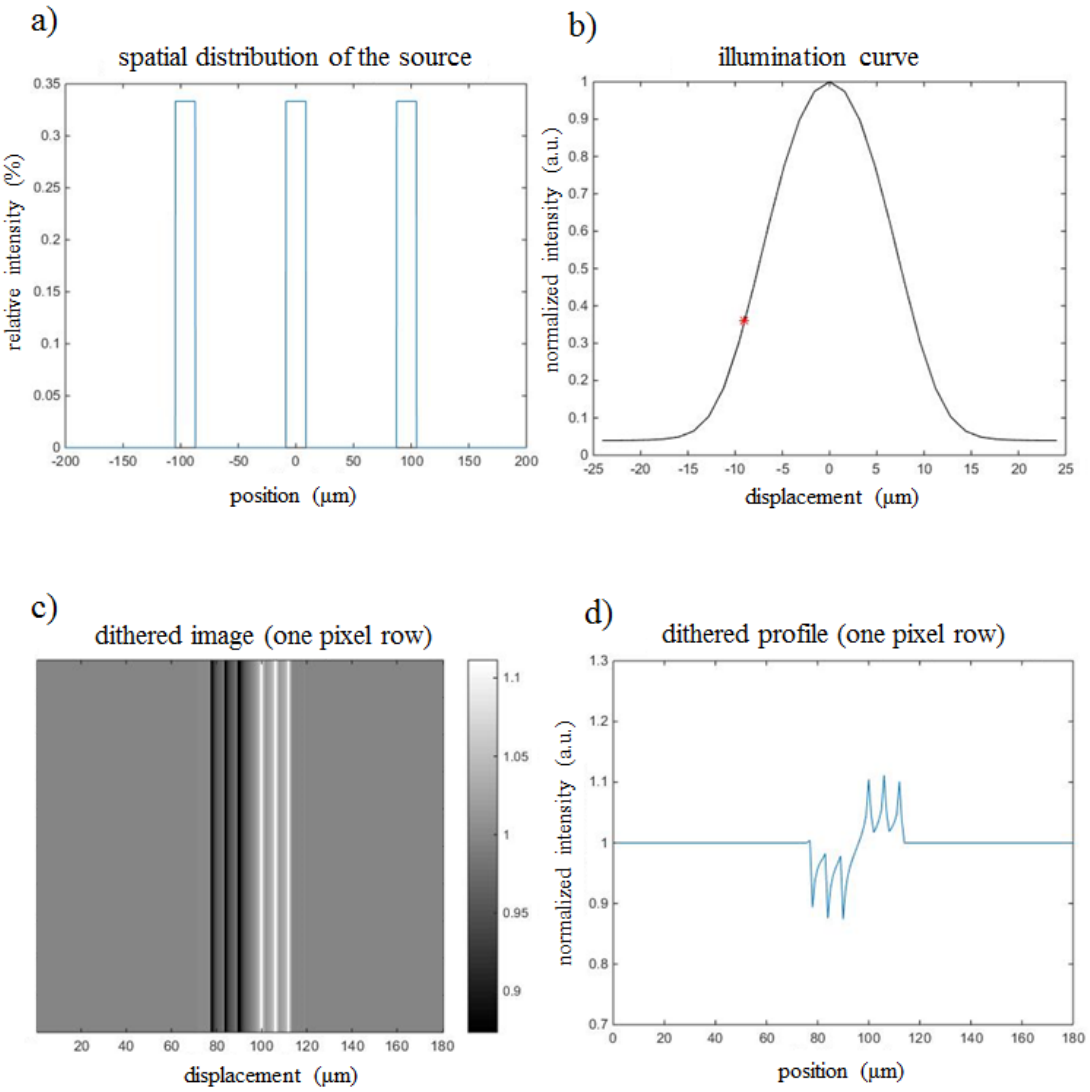

Figure 3.4: Effect of the source distribution (a) on the illumination curve (b), the image of a wire (c) and the corresponding intensity profile along a pixel row (d). The relative contribution of the three sources to the intensity distribution is 33%, 33% and 33%. The red star drawn along the curve in (b) represents the position on the illumination curve at which the images are simulated. The grey-scale values refer to normalized intensity.

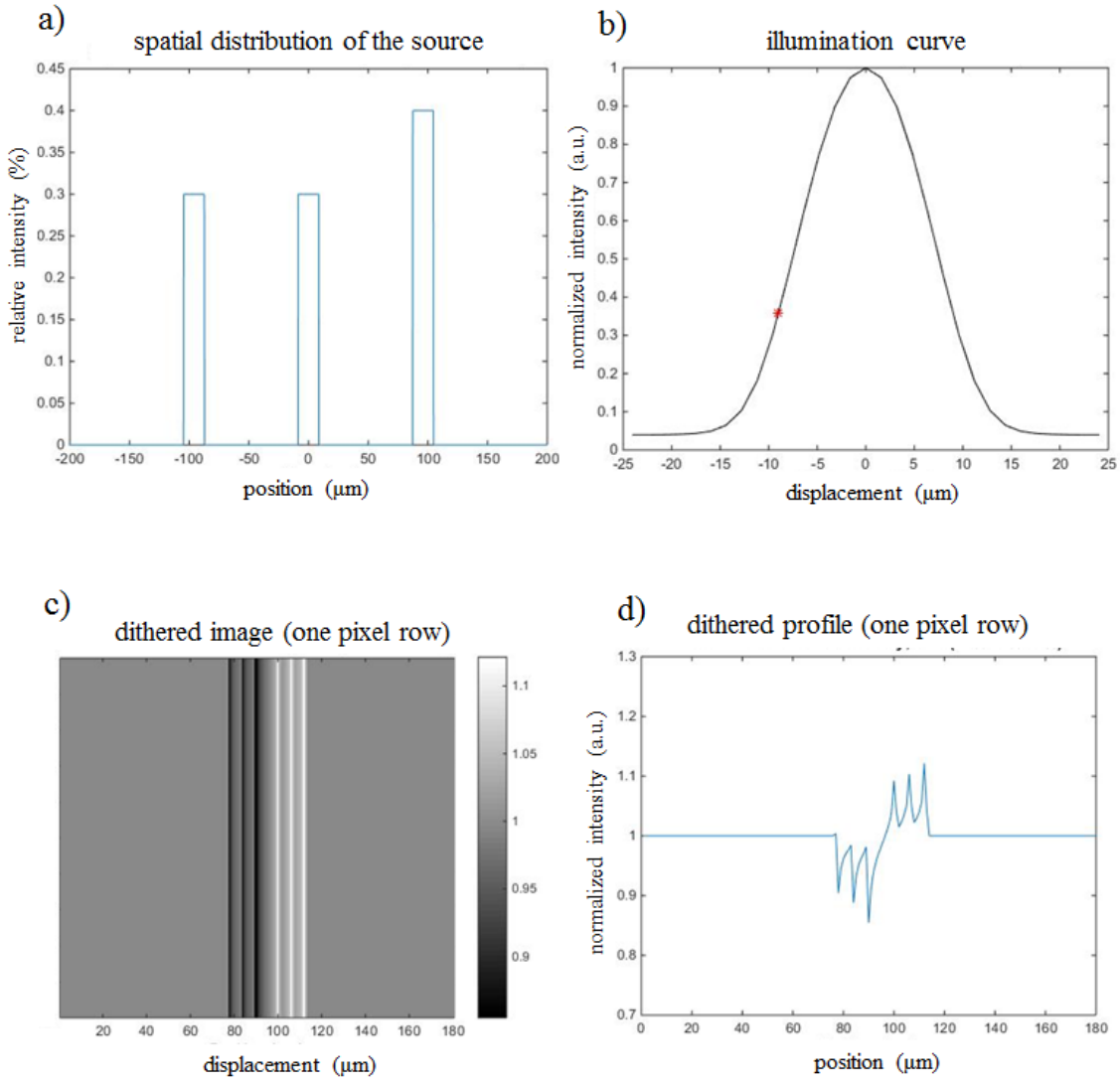

Figure 3.5: Effect of the source distribution (a) on the illumination curve (b), the image of a wire (c) and the corresponding intensity profile along a pixel row (d). The relative contribution of the three sources to the intensity distribution of 30%, 30% and 40%. The red star drawn along the curve in (b) represents the position on the illumination curve at which the images are simulated. The grey-scale values refer to normalized intensity.

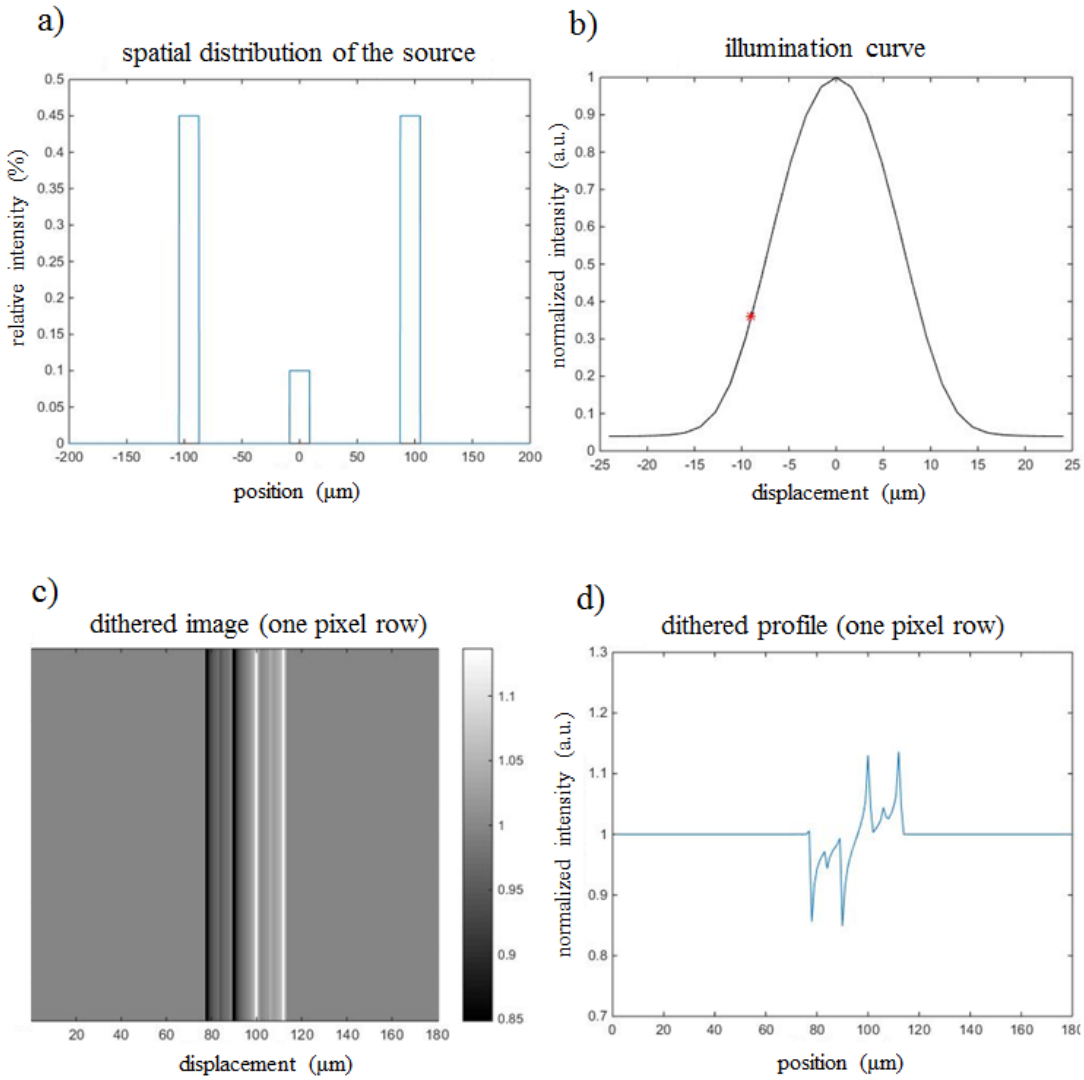

Figure 3.6: Effect of the source distribution (a) on the illumination curve (b), the image of a wire (c) and the corresponding intensity profile along a pixel row (d). The relative contribution of the three sources to the intensity distribution of 45%, 10% and 45%. The red star drawn along the curve in (b) represents the position on the illumination curve at which the images are simulated. The grey-scale values refer to normalized intensity.

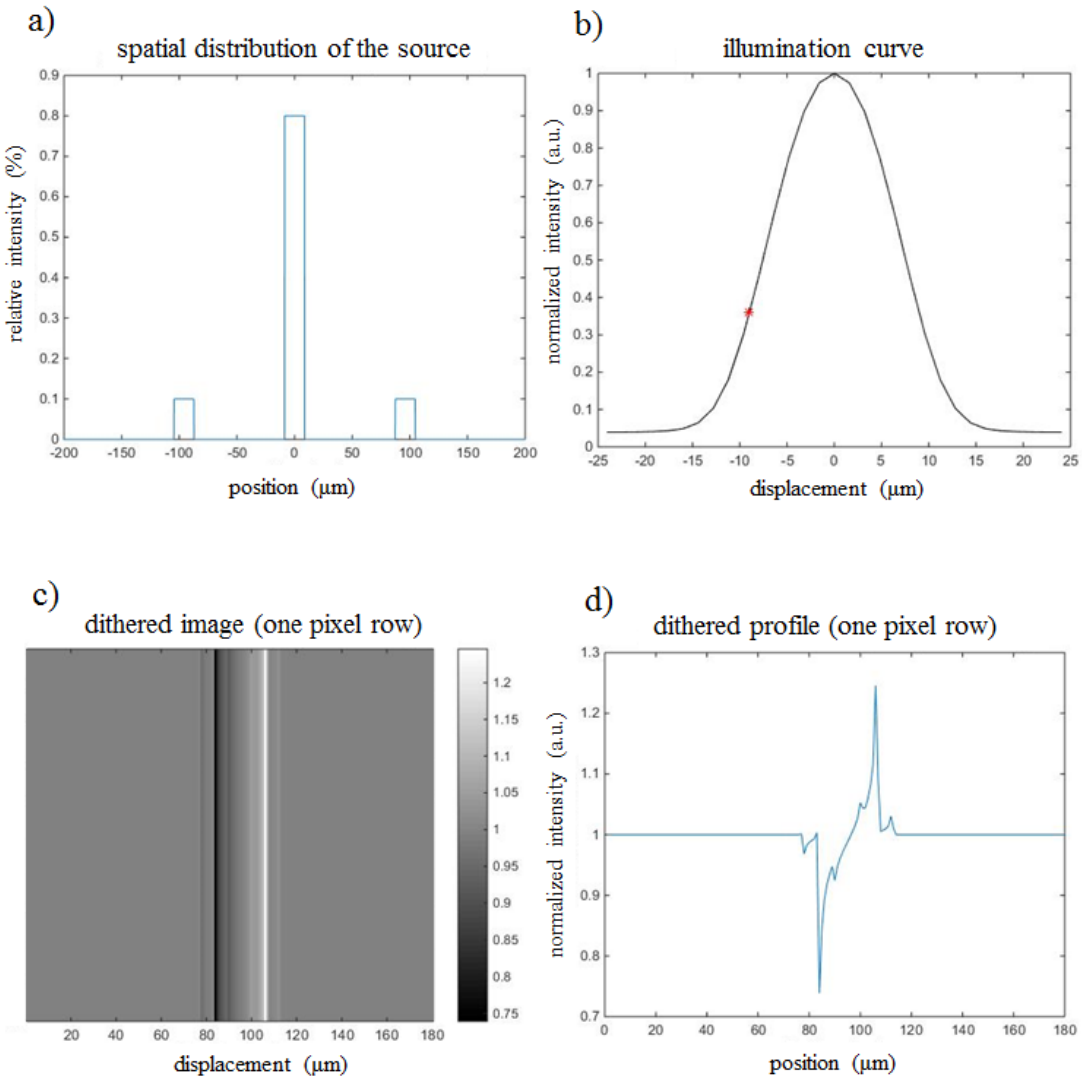

Figure 3.7: Effect of the source distribution (a) on the illumination curve (b), the image of a wire (c) and the corresponding intensity profile along a pixel row (d). The relative contribution of the three sources to the intensity distribution of 10%, 80% and 10%. The red star drawn along the curve in (b) represents the position on the illumination curve at which the images are simulated. The grey-scale values refer to normalized intensity.

In the above figures, four situations are represented, corresponding to different relative contributions of the sources to the total intensity. It can be noted that, while the illumination curve does not change shape in all the cases, both the images and the profiles change as a function of the sources' relative intensities: specifically, the source with the largest intensity contributes to the highest peak in the profile (with the corresponding fringe in the image becoming the brightest).

3.5 Experimental validation

Fig. 3.8 shows the setup used to experimentally validate the new approach via the acquisition of images of test phantoms and biological samples.

Since a large focal spot was not available, we created one by defocusing the micro-focal source previously used for our microscopy studies [83] where, however, the tungsten target was replaced with a molybdenum one. The source featured a 10 μm thick transmission Mo target, and was operated at 50 kV and 0.2 mA. While this is a transmission-type source that would normally allow reaching focal spots of 3-4 μm, in this case it was defocused to $> 250\,\mu$m, allowing the production of three sources via a 150 μm thick gold mask with a pitch of 98 μm and 17 μm apertures. A downside of this approach is the low emitted flux, since the source does not allow increasing the current above 0.2 mA; coupled to the use of an indirect conversion, passive-pixel CMOS-based flat panel detector (Hamamatsu C9732DK), this resulted in a noise level in the images much higher than normally observed in EI experiments. However, this sub-ideal setup was sufficient to show that the approach works, and the agreement with the simulation supports the reliability of the obtained results. In particular, it should demonstrate that the sensitivity model described in Ref. 15, which allows maintaining a constant sensitivity by simultaneously reducing system length and focal spot size, still holds. This will be

validated experimentally in future developments, along with possible tradeoffs between available flux and cost of existing x-ray sources with extended focal spots.

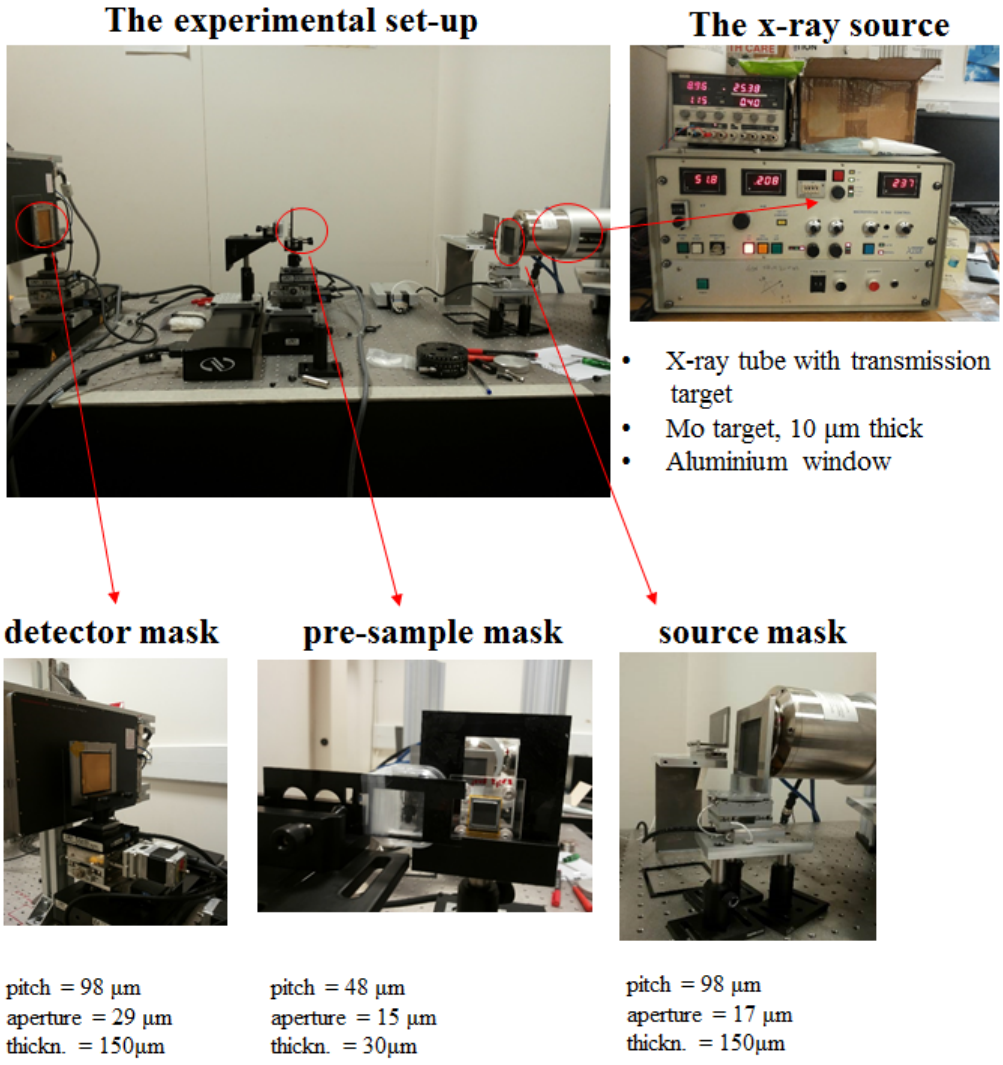

Figure 3.8: Basic components of the new EI configuration. Source and detector mask are made of 150 μm thick gold electroplated on a 500μm thick graphite substrate, while the sample mask is made of 30 μm thick gold on a 150μm thick graphite substrate.

The detector mask had the same period as the source mask (i.e. 98 μm), while the aperture size was 29 μm instead of 17 μm. This imposes the use of a "symmetrical" setup for

the pre-sample mask position (see Fig. 3.2), similarly to a setup previously introduced for grating interferometry [110]. We used a mask which we already had available, with 48 μm pitch, 15 μm apertures and 30 μm gold nominal thickness, previously used in Ref. [2]. Harmonic matching in a symmetric configuration would require either a pitch of 49 μm in the pre-sample mask, or of 96 μm in source and detector mask, if a pre-sample mask with 48 μm pitch is used. Therefore, this was obtained through a small rotation of the source and detector mask to slightly reduce their effective pitch. This enabled a significant system length reduction while maintaining a propagation distance and a projected source size very close to those used in previous systems, where a 70 μm focal spot was demagnified 4 times by the 1.6/0.4 source-to-sample/sample-to-detector distance arrangement [65, 78, 92]. All masks were aligned by means of the compact system described in the previous chapter. Inter-mask distances were of 0.5 m, for an overall system length of 1 m. It should be noted that the thin gold layer of the pre-sample mask is another non-ideal parameter affecting the ultimate image quality.

3.5.1 The illumination curve

A key validation test on the system modelling is the match between simulated and experimental illumination curves, i.e. the curves obtained in the absence of the sample when the pre-sample mask is scanned over one period in the direction transverse to the mask apertures (for a detailed description see Chapter 2). In this experiment, the illumination curve was also used to check the alignment since, if harmonic matching is not achieved, the illumination curve would be broadened. Figure 3.9 shows the comparison between simulated (solid line) and experimental (circles) illumination curves, demonstrating that a good agreement was obtained.

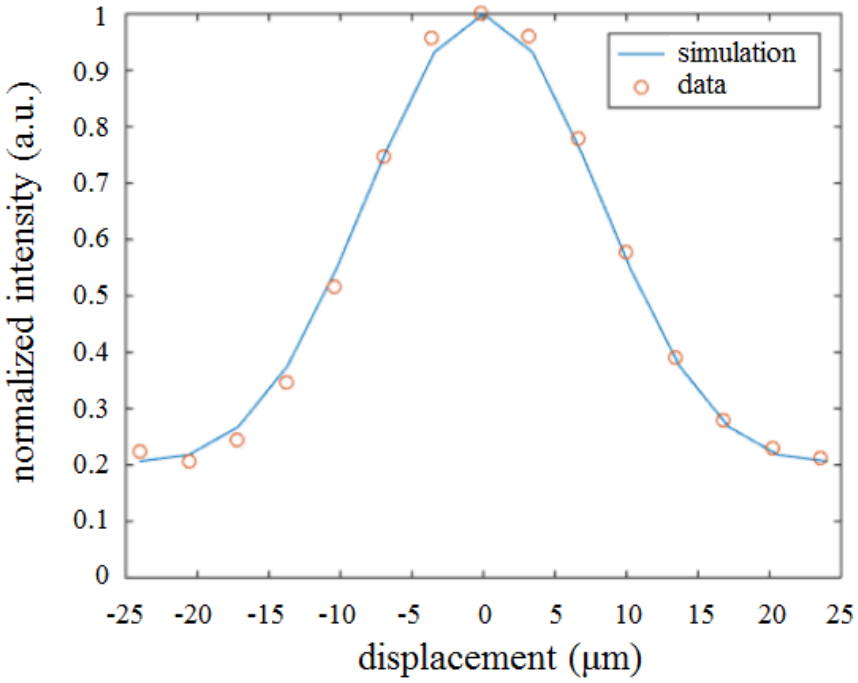

Figure 3.9: Simulated (solid line) vs experimental (circles) illumination curves. The 20% offset in both curves is due to the relatively high transmission through the thin sample mask. The same parameters used in the experiment were implemented in the simulation based on a wave optics model [3].

3.6 Results

Experimental images of geometrical objects are shown in Figs. 3.10 and 3.11. Cylindrical fibres featuring both high (Sapphire, diameter 250 μm) and low (Polybutylene Terephthalate (PBT), diameter 180 μm) absorption and phase shifts were used.

Experimental acquisitions were performed with 12 dithering steps of 4 μm size and exposure times of approximately 1000 seconds per position. The acquired images were subsequently deconvolved with the Lucy-Richardson procedure, in order to reduce the distortions induced by the convolution of the original image (produced by a single

source with a large focal spot) with the source spatial distribution (given by a series of three rectangular functions corresponding to the three sub-sources). If this procedure is performed correctly, the three intensity peaks corresponding to each sub-source should be restored to a single one with enhanced intensity.

All images are mixed intensity projections, obtained by illuminating only one side of the detector pixels with 50% of the total intensity (corresponding to one side of the illumination curve).

The agreement with the simulation provides confidence that extension to quantitative phase retrieval [92] and to dark field imaging [89] can be applied to these images, just as done previously for "standard" EI images. These developments go beyond the scope of the current proof-of-concept study and will be explored in future work. Two things can be noted: 1) the deconvolution procedure restores the expected "single positive / single negative" peak typical of differential phase contrast profiles, while at the same time restoring the higher peak intensity that would be produced by a single source, and 2) a good agreement between simulation and experiment was obtained for both the acquired and the deconvolved profiles. In particular, Figs. 3.10(d) and 3.11(d) compare the latter with theoretical profiles generated by a single source. This last aspect is particularly important, because it proves that the deconvolution procedure is capable of restoring images equivalent to those that would be created by a single source. The remaining small oscillations around the main peaks are due to cross-talk between pixels [2, 65]; indeed, they are also present in the profiles simulated through use of a single source. Note that cross-talk had not been added to the simulated profiles shown in Fig. 3.3, since in that case we were interested in understanding the signal behaviour under "ideal" conditions. All images were obtained with the pre-sample mask placed in the position corresponding to the maximum slope in the illumination curve, i.e. to a normalised intensity of approximately 0.6 (see Fig. 3.9 for reference).

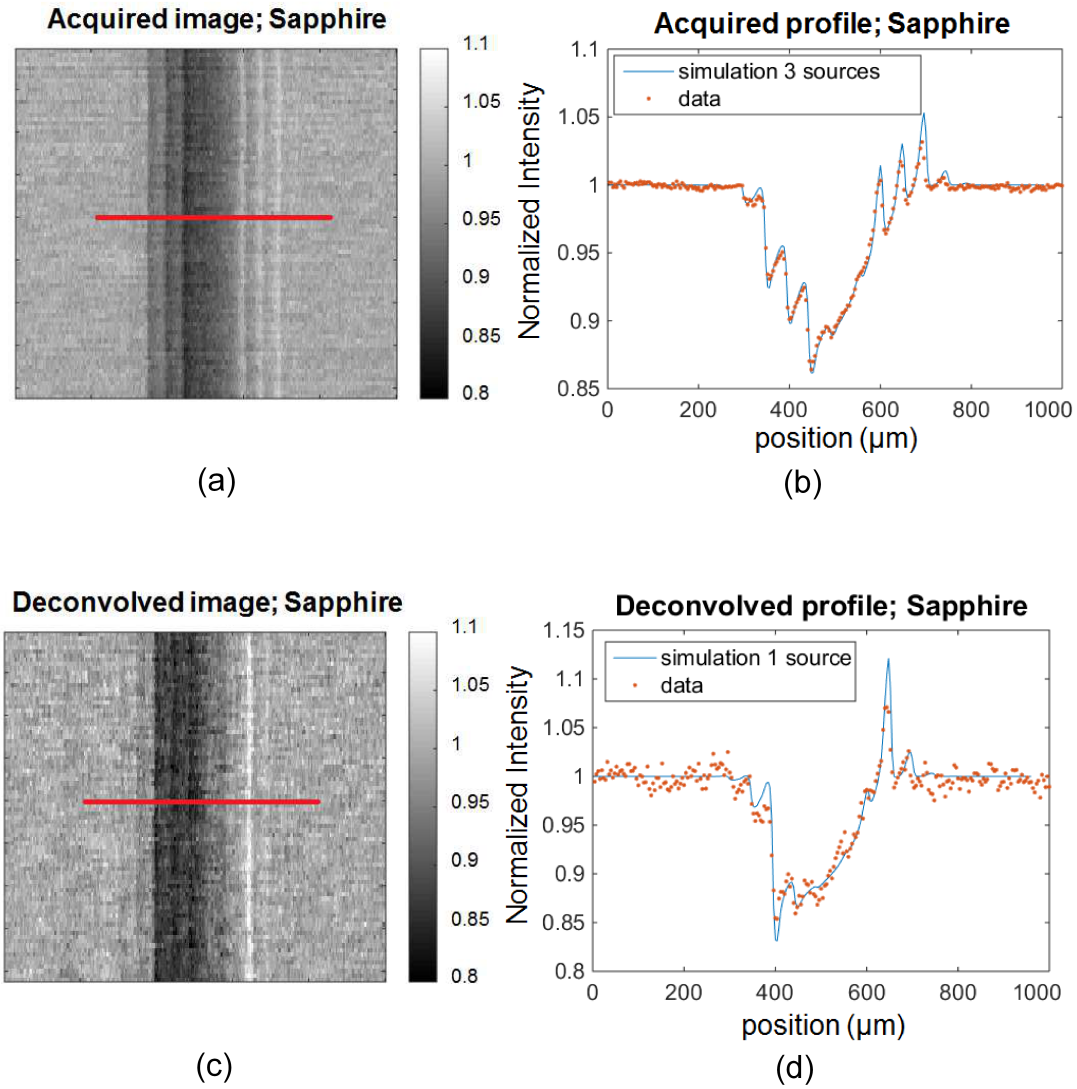

Figure 3.10: Dithered images of cylindrical fibres made of sapphire ((a)acquired and (c) deconvolved). Corresponding image profiles along the pixel rows are indicated by the solid red lines across the images ((b) sapphire acquired, (d) sapphire deconvolved). For all profiles, solid lines represent the simulation and dots the experimental values.

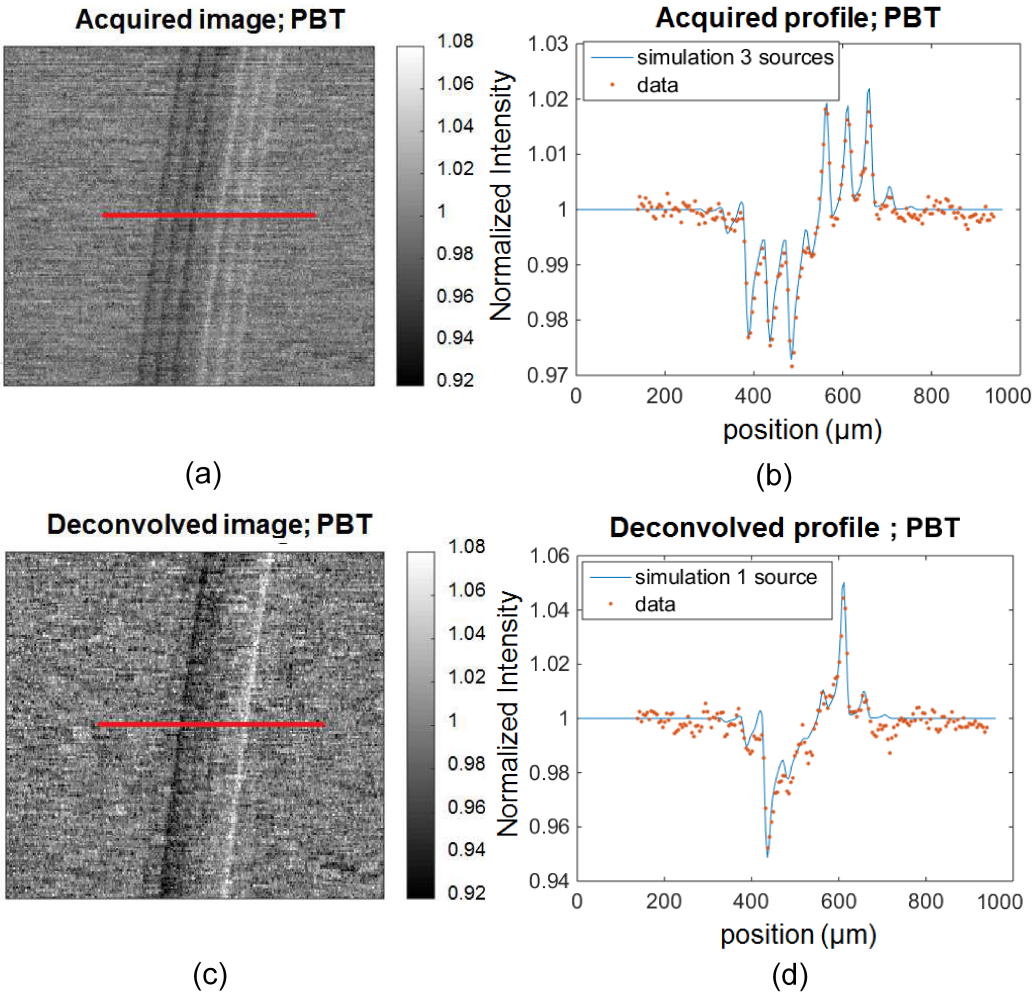

Figure 3.11: Dithered images of cylindrical fibres made of PBT ((a) acquired and (c) deconvolved). Corresponding image profiles along the pixel rows indicated by the solid red lines across the images ((b) PBT acquired, (d) PBT deconvolved)). For all profiles, solid lines represent the simulation and dots the experimental values.

Finally, in order to test the approach on a more complex biological sample, we acquired

images of a ground beetle, with the same setup and imaging conditions described above. Acquired and deconvolved images are shown in Figs. 5(a) and 5(b), respectively. Also in this case the three differential phase contrast peaks are restored to one (see arrows), and their intensity is enhanced. Additional peaks of lower intensity can be attributed to cross-talk between adjacent pixels, as discussed previously.

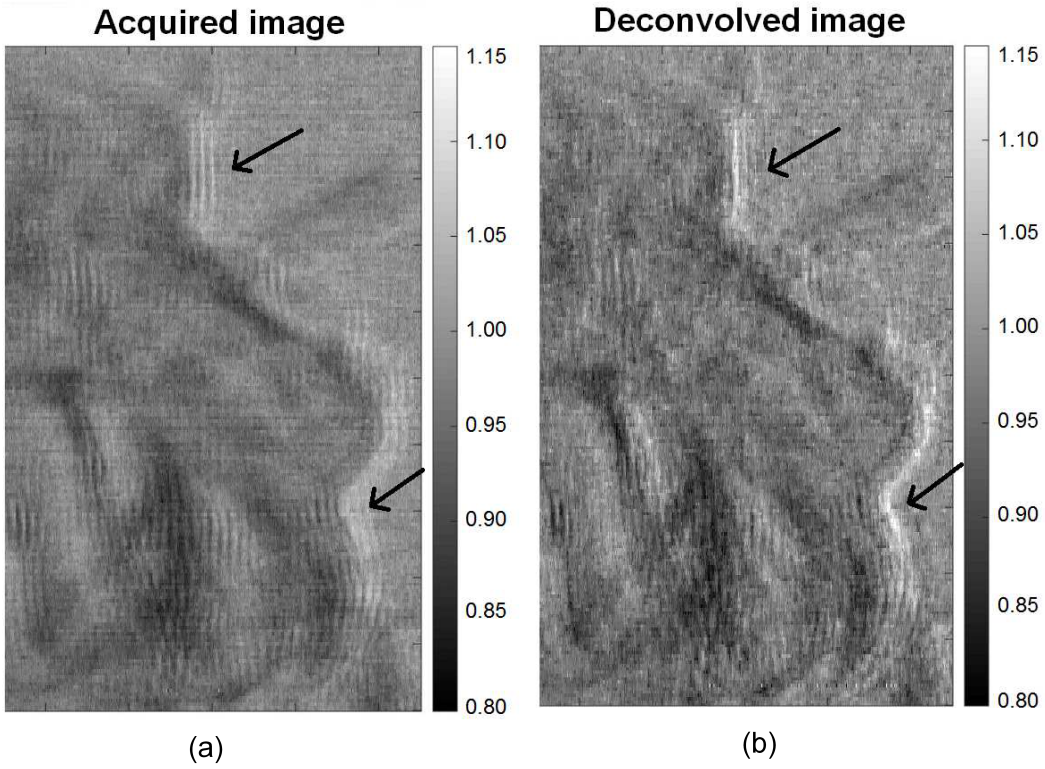

Figure 3.12: Acquired (a) and deconvolved (b) images of a ground beetle. The right part of the head is shown to underline how the three peaks in the recorded image are restored to a single, more intense one in the deconvolved image (see arrows).

3.7 Conclusions

We have performed a proof-of-concept study to demonstrate that the segmentation of a large focal spot X-ray source through an appropriate mask is a viable approach in EI XPCI.

While in principle it would be possible to create sub-sources as large as 100 μm, the creation of smaller sources offers the opportunity to simultaneously reduce the system dimensions. This additional aspect was also explored in this proof-of-concept study, by building and evaluating a system with an overall length of 1 m.

The use of multiple sub-sources results in the creation of a corresponding number of spatially shifted images, which need to be disentangled by means of appropriate algorithms. In this proof-of-concept study, good results were obtained by using the Richardson-Lucy deconvolution method with a total variation regularization. One important aspect of future studies will be the assessment of whether the deconvolution procedure affects image quality. It should be noted however that positive indications on the effectiveness of similar approaches have already been provided for Free Space Propagation (FSP) [22, 23].

While the non-ideal nature of the used proof-of-concept setup (especially low flux and thin pre-sample mask) resulted in limited signal-to-noise ratio, the experiment was sufficient to prove that the proposed approach works, and provides results which are in agreement with our simulation framework. Future work will further develop this concept through the design of optimised systems, especially in terms of e.g. maximum number of sources that could be used and minimum system dimensions.

4

Study of the angular sensitivity of EI systems as a function of the source-to-detector distance

4.1 Introduction

In the previous sections, I looked at different approaches that have been explored to expand the potential of Edge Illumination (EI) in terms of commercial translation.
In Chapter 2 the realization of an EI system based on compact and light piezoelectric motors [87] was described, which improves the portability of the setup without affecting its performance in terms of angular sensitivity.
In Chapter 3 a new configuration featuring a source mask (added to the conventional setup) was analyzed. The latter allows the use of cheaper X-ray sources [95] by sectioning the large focal spots produced by conventional tubes. Even if this configuration enables the realization of more compact setups, reducing the system length from 2 m (used so far) to 1 m, no quantitative results were given in terms of loss/gain in sensitivity.

This aspect has been taken into consideration in this Chapter, where I quantitatively studied, through a combination of simulation and experimental work, the dependence of the angular sensitivity on the distance between X-ray source and detector, while keeping the system magnification constant.
First, I showed the results of simulations based on the assumption of constant exposure time and Poisson distribution for the detector noise (valid for photon-counting detectors), for a wide range of distances (0.5 m to 3 m).
Subsequently, I compare the simulated results with the experimental ones that I obtained with the same setup parameters (pitches and apertures of the masks, exposure time, range of distances), but using an integrating detector, since a photon counter was not available.

4.2 Purpose of the study

Let us consider the standard laboratory Edge Illumination (EI) setup (already described in detail in Chapter 1), shown again in Fig. 4.1 for ease of readability.

An important parameter that must be taken into account in this part of the study is the system magnification, which can be expressed by:

$$M = \frac{d}{z_1} = = \frac{z_1 + z_2}{z_1} = 1 + \frac{z_2}{z_1} \tag{4.1}$$

where d is the source-to-detector distance, z_1 is the distance between the X-ray source and the pre-sample mask, and z_2 is the distance between the pre-sample and the detector masks. Typical magnification values used in EI experiments range from 1.25 to 10, with the latter being mainly used for microscopy applications aimed at much higher image resolutions (microns instead of tens of microns).

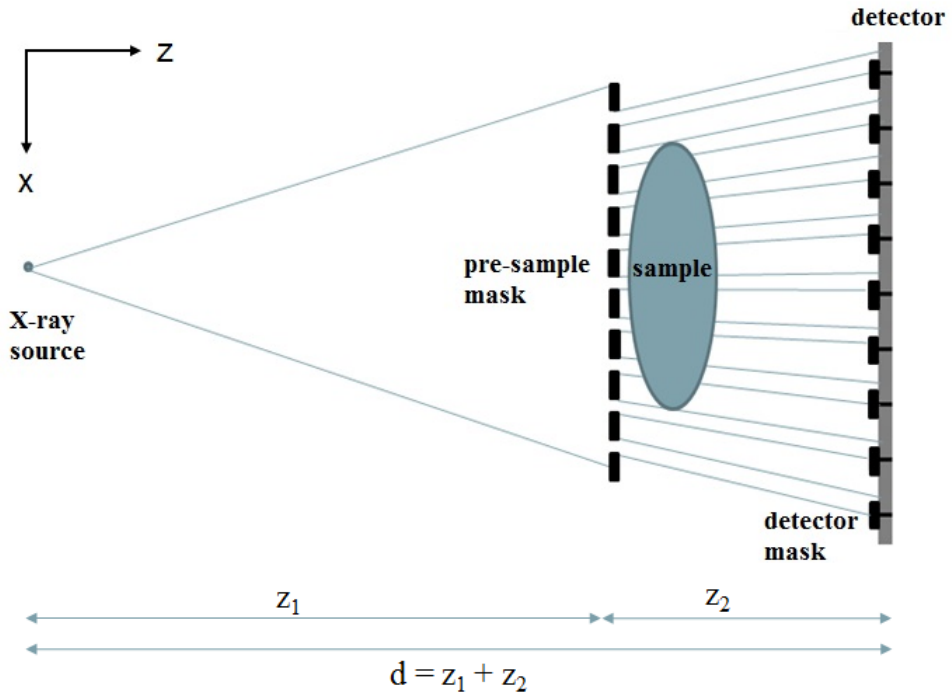

Figure 4.1: Standard laboratory EI setup.

Another important parameter is the angular sensitivity. Its value, as already discussed in previous chapters, gives an estimation of the lowest refraction angle detectable with our method (for a given counting statistics). Typical values of the sensitivity achievable with laboratory X-ray sources are of the order of few hundred nrad [80], depending on the specific setup.

This part of the study focuses on evaluating the effect on angular sensitivity caused by a rescaling of the overall system length (while keeping the magnification constant). The results of this analysis can be used to design more compact systems which, combined with the use of piezo-motors that enable the easy transportation of the setup, can make EI more suitable for straightforward translation into real-world applications.

4.2.1 The underpinning principles

Let us consider the situation in which the noise in an image depends only on the number of photons N_{ph} reaching the detector in a given time interval. This assumption is valid if a photon counting device is used, for which there is no contribution to the noise by the dark current. In this case, the noise distribution is well described by a Poisson statistics and can be expressed by:

$$\sigma = \sqrt{N_{ph}} \tag{4.2}$$

where σ is the standard deviation of a region of the image where no sample is present, and represents a measurement of the background fluctuation. A better estimation is given by its relative value, i.e. normalized to the mean value of the background signal. This quantity, that we will call *relative noise level* ϵ_{rel}, can be defined as:

$$\epsilon_{rel} = \frac{\sigma}{N_{ph}} \tag{4.3}$$

where we took into account that the value of the background signal is given by the number of detected photons N_{ph}. For a photon counter, the above relationship can be written as

$$\epsilon_{rel} = \frac{\sqrt{N_{ph}}}{N_{ph}} = \frac{1}{\sqrt{N_{ph}}} \tag{4.4}$$

where we took into account Eq. 4.2, valid for a Poisson distribution of the noise.
We also note that, as a consequence of the inverse square law, the number of photons reaching each detector pixel, in a given interval of time, is inversely proportional to the square of the distance between source and detector:

$$N_{ph} \propto \frac{1}{d^2} \tag{4.5}$$

By inserting this result into Eq. 4.4, we conclude that the relative noise level is proportional to the distance between X-ray source and detector:

$$\epsilon_{rel} \propto d \tag{4.6}$$

When an object is introduced in the field of view, refraction effects give rise to a variation in the detected signal. This depends on the deviation of the X-rays from their original path after passing through the object: the larger the deviation (or *shift*), the bigger is the change in the signal (i.e. detected photon counts).

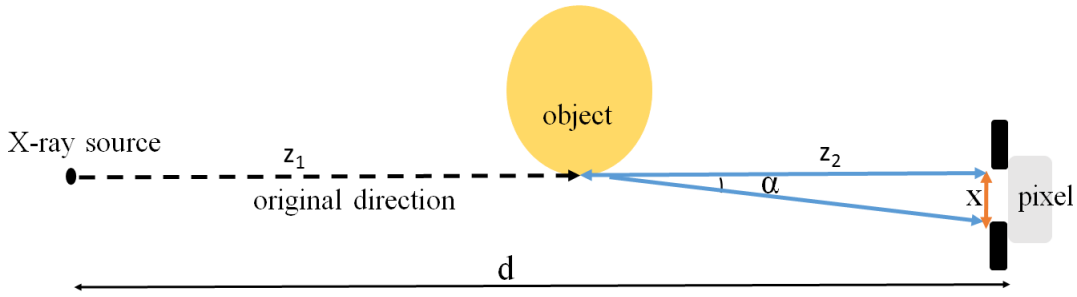

Figure 4.2: Schematic showing the geometric relationship between the shift x and the refraction angle α of an X-ray after passing through an object, placed at a distance z_2 from the detector pixel and at a distance z_1 from the source.

With reference to Fig. 4.2, in the approximation of small angles, the shift x of the photon from its original direction is related to the refraction angle α and to the object-to-detector distance z_2 via the following relationship:

$$x \approx \alpha \cdot z_2 = \alpha \cdot \left(d \cdot \frac{M-1}{M} \right) \tag{4.7}$$

where we used the relationship $M = \frac{z_1+z_2}{z_2} \Rightarrow z_2 = \left(d \cdot \frac{M-1}{M}\right)$.
It can be noted that, whereas both the magnification M and the refraction angle α are constant, the shift x is proportional to the distance d, and so is the detected signal. It follows that, in a given time interval and for a fixed system magnification, the increment/decrement of the noise level with the distance is compensated by a corresponding increment/decrement of the detected signal, ultimately leading to a constant signal-to-noise ratio (SNR) and hence into a constant angular sensitivity.

4.2.2 Simulations

The above hypothesis was tested through a combination of simulated and experimental work. By using the wave optics model developed by Vittoria et al. (2013) [3], I simulated the setup shown in Fig. 4.1 to generate refraction signals of test samples, with the following parameters:

- **sample mask**: pitch = 79 μm, aperture width = 12 μm, gold thickness = 150 μm, graphite substrate thickness = 500 μm;
- **detector mask**: pitch = 98 μm, aperture width = 20 μm, gold thickness = 150 μm, graphite substrate thickness = 500 μm;
- **detector**: pixel size = 50 μm (operated in "pixel skipping" mode [2], i.e. skipping every other pixel column by using a detector mask with a projected pitch equal to double the pixel size);
- **Magnification**: M = 1.25;
- **source-to-detector distance range**: d = (0.5 ÷ 3) m

In order to obtain refraction images, a phase retrieval algorithm [80] needs to be applied. The latter requires two projection images with a pre-sample mask displacement (with

respect to the detector mask) corresponding to two different points on the illumination curve (described in Fig. 2.2 of Chapter 2). For this reason, two projection images on opposite sides on the illumination curve were simulated at each distance, characterized by %50 of the total intensity. The phase retrieval algorithm was applied after adding Poisson noise to the simulated projections, under the assumption that the noise depends only on the number N_{ph} of photons detected in a given time interval. The value of N_{ph} was rescaled according to Eq. 4.5 for each distance d. The corresponding standard deviation $\sigma_{refr.}$ in a rectangular background region (i.e. where no sample is present) was evaluated. This gives an estimation of the angular sensitivity in the refraction images, with higher values of the standard deviation corresponding to a worse sensitivity.
Fig. 4.3 shows a plot of the standard deviation σ as a function of the distance d, with the corresponding values reported in Tab. 4.1.

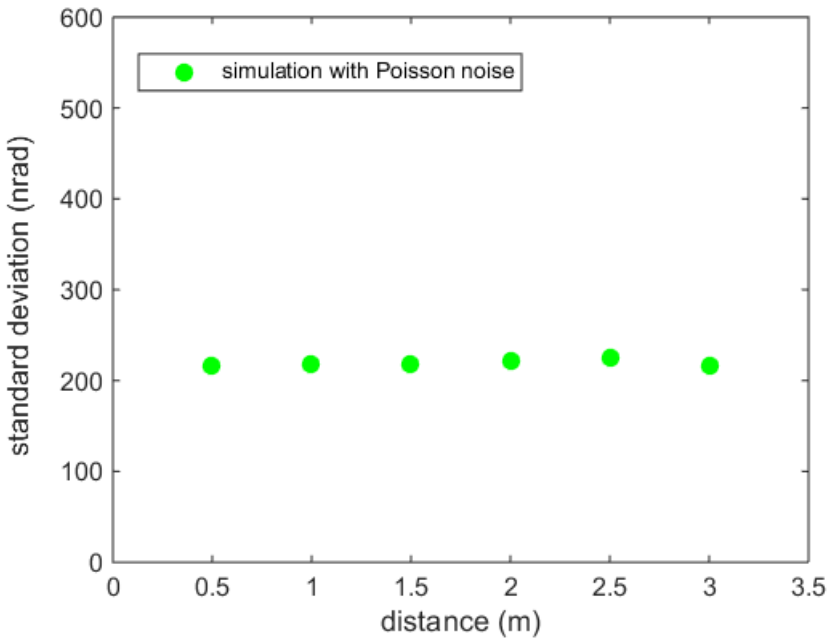

Figure 4.3: Plot of the simulated background standard deviation as a function of the source-to-detector distance.

As expected, the values of σ (and so the sensitivity), do not change appreciably with d, apart from small fluctuations.

Once again, it must be underlined that these values were obtained under the assumption of Poisson-like noise distribution. The results change substantially if this condition is not satisfied, as we will show in the next section.

distance (m)	standard deviation ($nrad$)
0.5	216
1.0	218
1.5	218
2.0	221
2.5	225
3.0	217

Table 4.1: Standard deviation σ extracted from background regions of simulated images, for different values of the source-to-detector distance d.

4.3 Experimental measurements

The angular sensitivity was experimentally evaluated for different system lengths and the results of the measurements were compared with those obtained through the simulation.

The setup used for the experiment is shown in Fig. 4.4, in which we report only the configurations corresponding to $d = 3\,\mathrm{m}$ (maximum system length) and $d = 0.5\,\mathrm{m}$ (minimum system length).

The values used for the masks apertures and pitches, the system magnification and the range of investigated distances were the same as those described above for the simulation case.

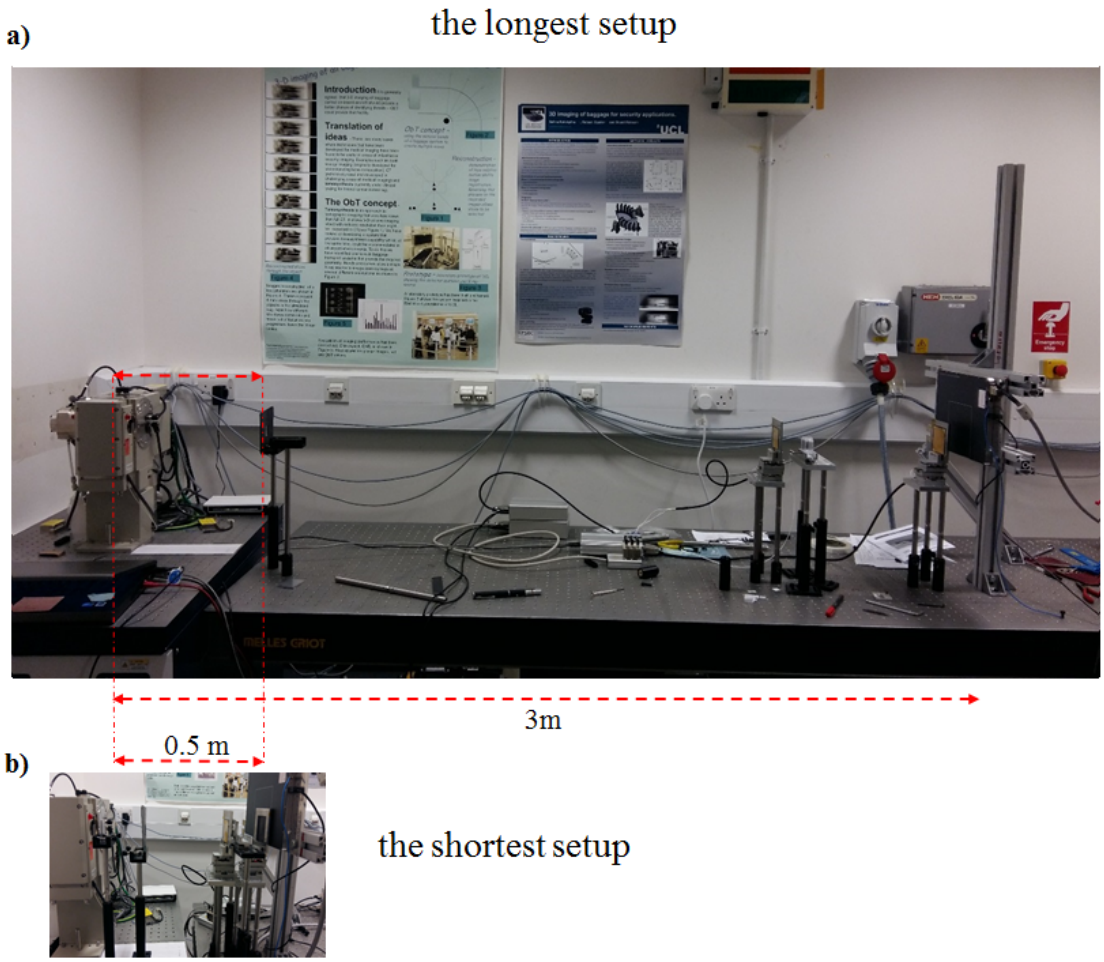

Figure 4.4: Experimental setups corresponding to $d = 3\,\mathrm{m}$ (a) and $d = 0.5\,\mathrm{m}$ (b).

For each image acquisition, the following parameters were chosen and kept constant for all configurations:

- 16 dithering positions for the sample;
- for each sample acquisition, 10 frames acquired with an exposure time of 1.2 seconds, for a total of 12 seconds;

- for each flat field image, 40 frames of 1.2 seconds (corresponding to 4 times the number of frames used for the sample: this is always possible as flat field images can be acquired "off-line");

A Rigaku MultiMax-9 rotating anode tube with a tungsten target was used. As the total exposure time was the same for each configuration, the mA and kVp values were chosen in order to match two requirements: avoid the saturation of the detector at 0.5 m (where the flux of photons is maximum) and have enough statistics at 3 m (where the flux reaching the detector is minimum). A good compromise was obtained by operating the source at 40 kVp and 10 mA.
The detector used in the experiment was a CMOS-based flat panel with directly deposited CsI (Hamamatsu C9732DK-11). This is an integrating device, which does not count individual photons, but rather accumulates the photon-induced signal for a preset period of time, prior to the integrated signal being read out. This characteristic is crucial to the understanding of the results of our experimental measurements.

4.3.1 Sensitivity measurements

In Fig. 4.5, the trend of the measured standard deviation σ as a function of the source-to-detector distance d is compared to the one obtained from the simulation.
A significant deviation of the experimental values from the simulated ones can be noted. In particular, while in the former the observed standard deviation increases with the distance, in the latter it is basically constant, as described earlier in the chapter.
The experimental values of σ, along with the corresponding errors, are shown in Tab 4.2 for the range of investigated distances $(0.5 \div 3)$ m.

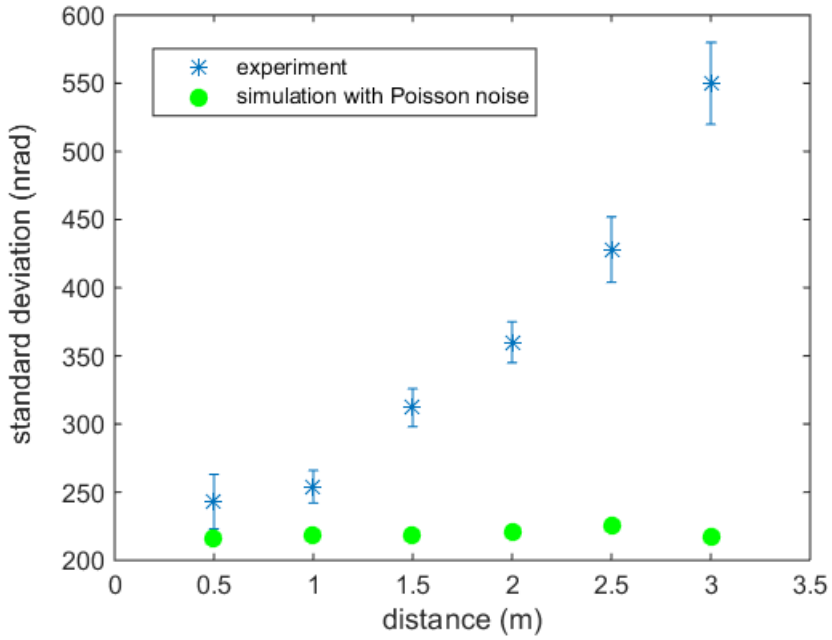

Figure 4.5: Comparison of the experimental (blue asterisk) and simulated (green circles) values of the background standard deviation σ as a function of the source-to-detector distance d. Note that higher values of σ correspond to a worse sensitivity.

distance (m)	standard deviation $(nrad)$
0.5	243 ± 20
1.0	254 ± 12
1.5	312 ± 14
2.0	360 ± 15
2.5	428 ± 24
3.0	550 ± 30

Table 4.2: Standard deviation σ extracted from background regions of experimental images, for different values of the source-to-detector distance d.

The above results suggest that, within the constraints of this study (i.e. use of a constant emitted flux combined with an integrating detector), and especially in applications without any dose restrictions, configurations with smaller system lengths are more convenient as they yield a lower standard deviation i.e a higher sensitivity.

Figs. 4.6 to 4.11 show acquired images of test samples, together with the corresponding

intensity profile along a row of pixels, for the entire set of investigated distances, with the experimental conditions described in section 5.3.

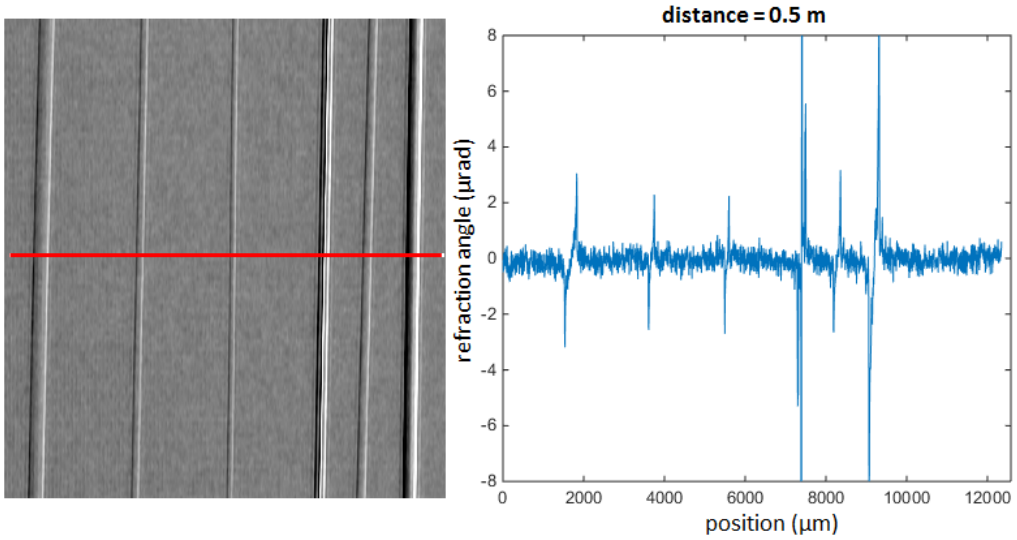

Figure 4.6: Refraction image (left) of wires of different materials and corresponding intensity profile (right) along a row of detector pixels (right), for d = 0.5 m. In order to stretch the contrast in the image, a grey-scale value range of [-3 3] μrad was used.

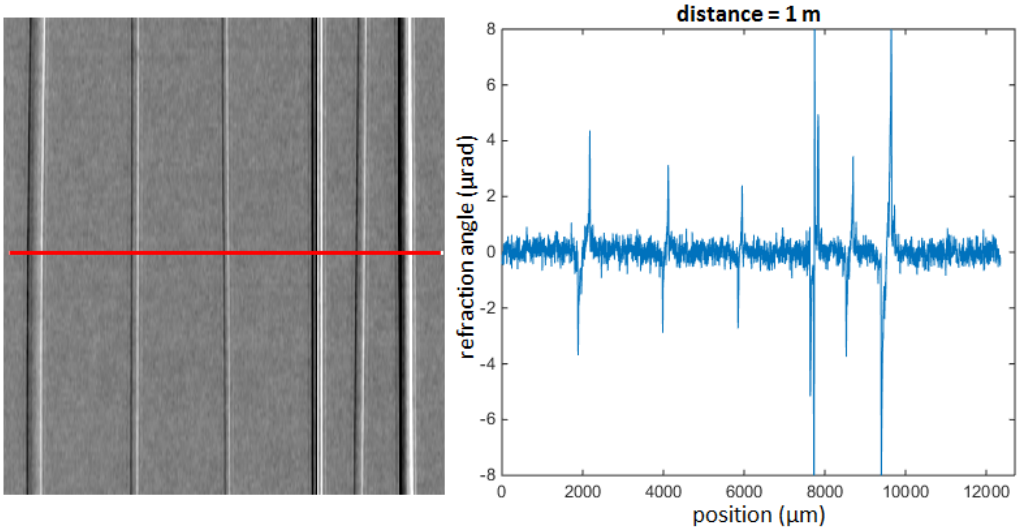

Figure 4.7: Refraction image of wires of different materials (left) and corresponding intensity profile along a row of detector pixels (right), for d = 1 m. The grey-scale value range is [-3 3] μrad.

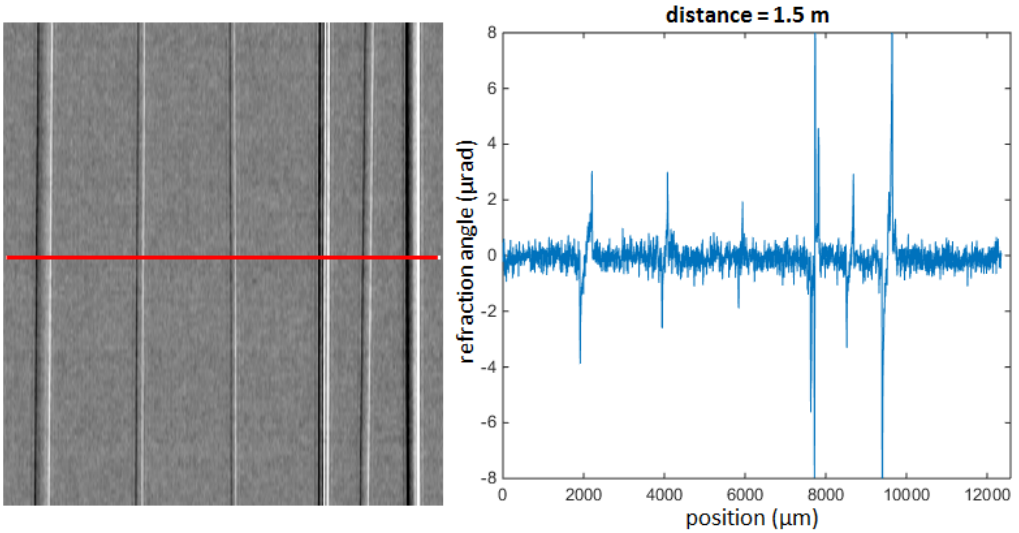

Figure 4.8: Refraction image of wires of different materials (left) and corresponding intensity profile along a row of detector pixels (right), for d = 1.5 m. The grey-scale value range is [-3 3] μrad.

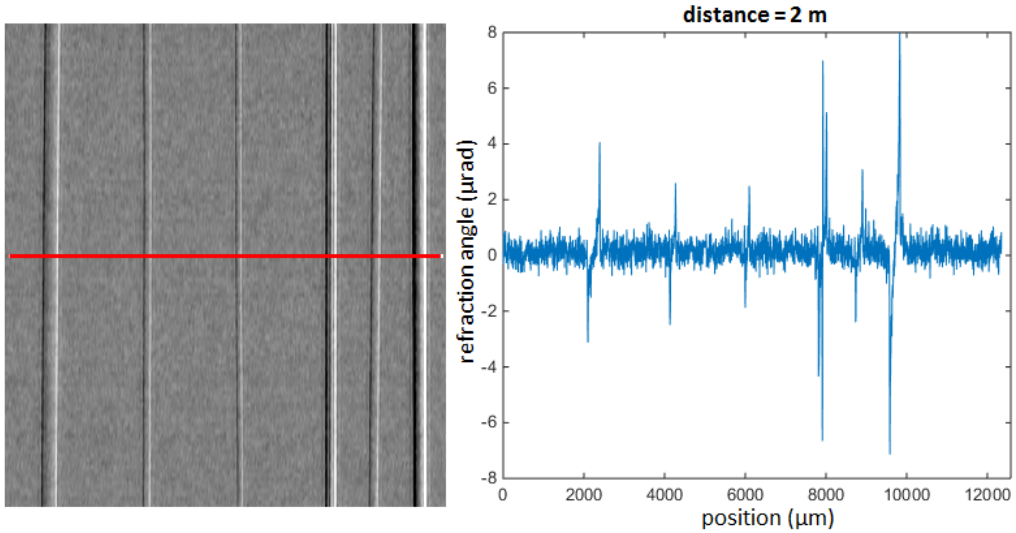

Figure 4.9: Refraction image of wires of different materials (left) and corresponding intensity profile along a row of detector pixels (right), for d = 2 m. The grey-scale value range is [-3 3] μrad.

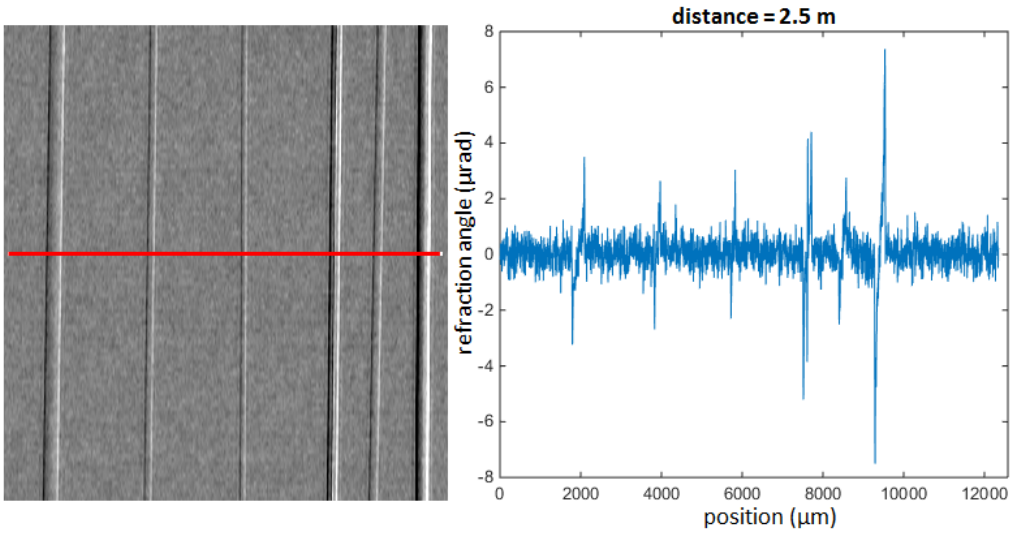

Figure 4.10: Refraction image of wires of different materials (left) and corresponding intensity profile along a row of detector pixels (right), for d = 2.5 m. The grey-scale value range is [-3 3] μrad.

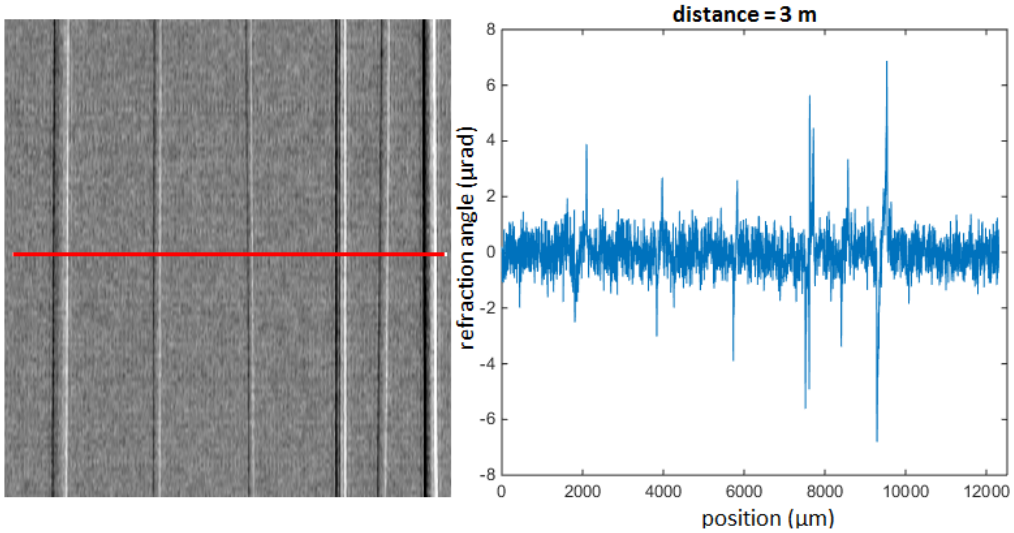

Figure 4.11: Refraction image of wires of different materials (left) and corresponding intensity profile along a row of detector pixels (right), for d = 3 m. The grey-scale value range is [-3 3] μrad.

It can be noted that, as the distance increases, the quality of the images gradually

gets worse. This is also confirmed by looking at the intensity profiles, where the noise level in the background region increases for higher distances.
In the next section, an explanation of the discrepancy between experimental and simulated results will be provided.

4.4 Discussion and analysis

As already mentioned, if an image is acquired with a photon counting detector, the noise depends only on the number of photons reaching the device and its distribution can be described by Poisson statistics.
Hence, the corresponding noise model can be expressed through the variance $\sigma^2_{Poisson}$, with:

$$\sigma^2_{Poisson} = N_{ph} \tag{4.8}$$

For an integrating detector, the contribution of the dark current must also be included in the noise model. In this case, the total variance σ^2_{tot} is composed of two terms added in quadrature: one depending on the number of photons N_{ph} and given by Eq. 4.8, and one due to the dark current σ^2_{dark}.
This can be expressed by the relationship:

$$\sigma^2_{tot} = \sigma^2_{Poisson} + \sigma^2_{dark} \tag{4.9}$$

The corresponding standard deviation is then given by:

$$\sigma_{tot} = \sqrt{\sigma^2_{Poisson} + \sigma^2_{dark}} = \sqrt{N_{ph} + \sigma^2_{dark}} \tag{4.10}$$

One should consider that, since in this case the number of photons emitted by the X-ray source was the same for all measurements, as the exposure time and tube settings were

kept constant, the number of detected photons N_{ph} changes with the distance according to the inverse square law. Since 2 m is the standard system length for EI setups, then N_{ph} at the generic distance d can be expressed as a function of the number of photons $N_{ph}^{(2m)}$ at the reference distance of 2 m through the relationship $N_{ph} = N_{ph}^{(2m)} \cdot \left(\frac{2}{d}\right)^2$. Hence, if we call $\sigma_{tot}^{(d)}$ the standard deviation at the distance d, Eq. 4.10 can be rewritten as

$$\sigma_{tot}^{(d)} = \sqrt{N_{ph}^{(2m)} \cdot \left(\frac{2}{d}\right)^2 + \sigma_{dark}^2} \tag{4.11}$$

where the term in brackets rescales the quantum (Poisson) noise at d = 2 m to that observed at any other distance d at which the standard deviation is evaluated.

The second parameter σ_{dark}^2 was kept constant, because the noise due to dark current was integrated over a fixed time interval (the same for each distance). Under these assumptions, the relative contribution of this term, compared to the Poisson one, becomes more important at higher distances (where the number of photons is lower), which explains the increasing difference between experimental and simulated values.

In order to reproduce the experimental results obtained with an integrating rather than a counting detector, the simulation was repeated by adding, to the two projection images at 50% of the illumination curve, a noise component described by the model in Eq. 4.11. As the two parameters $N_{ph}^{(2m)}$ and σ_{dark} cannot be separated a priori, a χ^2 test was performed in order to obtain the values of the two parameters that provided the best match with the experiment. More specifically, the pair of values $\left(N_{ph}^{(2m)}, \sigma_{dark}\right)_{min}$ corresponding to the minimum of the χ^2 was chosen as the best estimate of the parameters for the noise model.

From the definition of χ^2, we can write:

$$\chi^2_{\left(N_{ph}^{(2m)}, \sigma_{dark}\right)} = \sum_{i=1}^{n} \frac{\left(e_i - s_i\left(N_{ph}^{(2m)}, \sigma_{dark}\right)\right)^2}{s_i\left(N_{ph}^{(2m)}, \sigma_{dark}\right)} \tag{4.12}$$

where e_i is the set of experimental values, $s_i\left(N_{ph}^{(2m)}, \sigma_{dark}\right)$ is the set of simulated ones, which depends on the couple of parameters $\left(N_{ph}^{(2m)}, \sigma_{dark}\right)$, and n = 6 is the number of investigated distances.

The χ^2 was evaluated for different pairs $\left(N_{ph}^{(2m)}, \sigma_{dark}\right)$. The first parameter was varied in the range $(1000 \div 15000)$, with a step equal to 500, while the latter was varied in the range $(0 \div 300)$, with a step equal to 20: this was chosen in order to cover a wide variability range and, at the same time, save computational time. The obtained values were then interpolated, in order to increase the number of points and obtain a more accurate estimation of the minimum for the χ^2, which was found in correspondence of the couple of values $(N_{ph}^{(2m)} = 6090, \sigma_{dark} = 107)_{min}$.

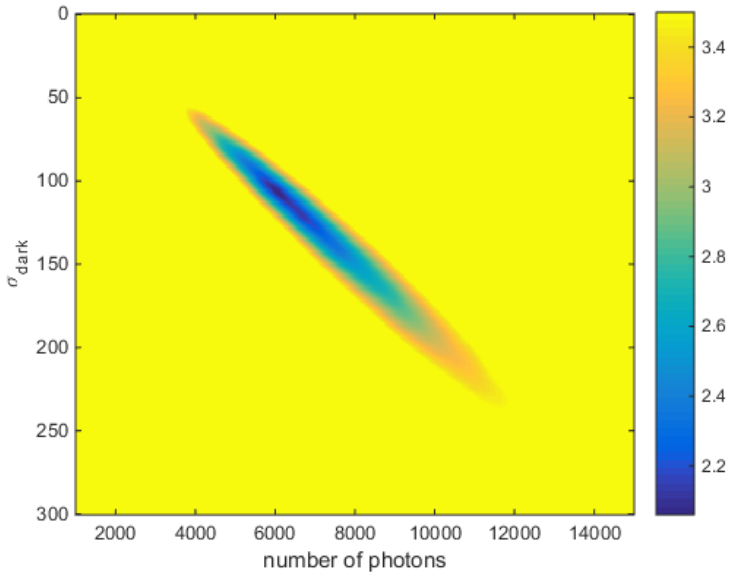

Figure 4.12: χ^2 values, in logarithmic scale, as a function of the parameters $N_{ph}^{(2m)}$ and σ_{dark}.

Fig.4.12 shows the values of χ^2 in logarithmic scale, as a function of $N_{ph}^{(2m)}$ and σ_{dark}. The darker region corresponding to lower χ^2 values is clearly visible in the figure, within the parameter range $N_{ph}^{(2m)} \simeq (5500 \div 7500)$ and $\sigma_{dark} \simeq (100 \div 120)$. An enlargement

of the region around the minimum is shown in Fig.4.13; the constrast was further stretched in this case for an easier visualization of smaller variations.

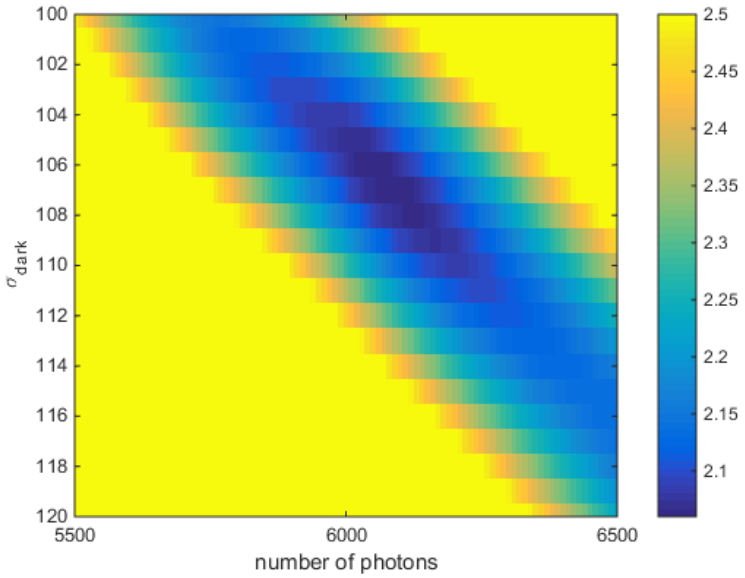

Figure 4.13: χ^2 values around the minimum, in logarithmic scale, as a function of the parameters $N_{ph}^{(2m)}$ and σ_{dark}, in a smaller area selected from the previous figure.

The pairs of values $(N_{ph}^{(2m)} = 6090, \sigma_{dark} = 107)_{min}$ was then used to simulate the background standard deviation σ with the noise model including the Poisson term and the correction due to dark current.

Tab.4.3 shows the values obtained through this refinement of the simulation. Fig. 4.14 compares the corresponding trend versus increasing distance, with the one measured in the experiment and the one obtained through the previous simulation that only included Poisson noise.

As can be seen, the match between simulated and experimental values is significantly improved by the inclusion of this additional term due to dark current. In fact, the experimentally observed trend of the sensitivity is well reproduced for all experimental points, apart from a slightly larger discrepancy observed at the longest distance d = 3 m.

distance (m)	standard deviation ($nrad$)
0.5	230
1.0	267
1.5	315
2.0	382
2.5	452
3.0	504

Table 4.3: Standard deviation σ extracted from background regions of simulated images, obtained by including the dark current term in the noise model, for different values of the source-to-detector distance d.

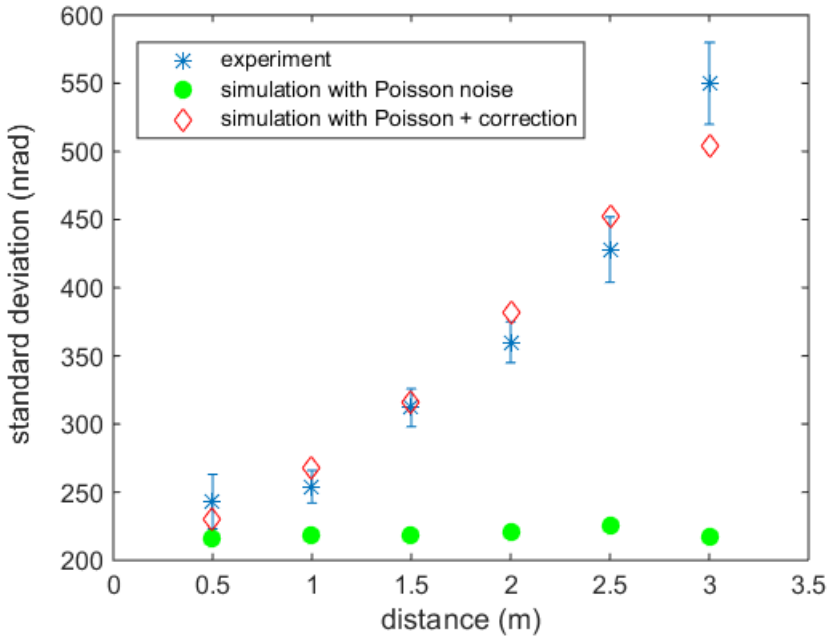

Figure 4.14: Comparison of the "corrected" values of the background standard deviation σ (red diamonds) with the the experimental ones (blue asterisks) and the ones simulated by only including Poisson noise (green circles), as a function of the source-to-detector distance d. Note that higher values of σ correspond to a worse sensitivity.

The little mismatch at d = 3 m could either be linked to an accident occurred during that specific measurement or could indicate that further refinements of the model might be required in order to include second order mechanisms that could have a slightly stronger

effect at longer distances (e.g. system vibrations, scattering from the mask substrates, etc...), investigating which lies beyond the scope of the present chapter.

It can be also noted that the increment of the background standard deviation with the distance corresponds to a worsening of the angular sensitivity. From this last result we can infer that, at fixed magnification, source conditions and exposure time, more compact setups are preferable with respect to larger ones if integrating detectors are employed, especially in applications where the dose delivered to the sample is not an issue.

4.5 Conclusions

In this work I presented an analysis of the dependence of the angular sensitivity on the distance between X-ray source and detector, for configurations in which the system magnification, tube settings and total exposure time are constant. The main purpose of the study was to test the possibility to develop more compact EI setups based on smaller overall system lengths, and understand how this affects the retrieved refraction signal.

Simulated results showed that, if Poisson fluctuations are the only source of noise, the standard deviation of a rectangular background region in the refraction images is expected to be constant within the range of investigated distances ($0.5 \div 3$) m. This would make the signal-to-noise ratio, and therefore the angular sensitivity constant, suggesting the possibility to reduce the dimensions of EI systems without any loss in terms of image quality, at least for applications where sample dose is not an issue. This

result, combined with the use of light and small piezo-motors (described in Chapter 2), could lead to the development of extremely compact imaging systems, down to a few tens of cm.

Different results were however achieved when an integrating detector was used. The experimental values of the standard deviation of the background showed a significant mismatch with respect to the ones simulated by assuming counting behaviour. In particular, while in the latter the standard deviation of the background remained constant with the distance, in the former this increased, indicating a reduction in angular sensitivity with increased system length. This is explained by considering a constant term σ_{dark} due to the dark current and including it in the model that describes the noise behaviour of an integrating detector.

The values $\sigma_{dark} = 107$ and $N_{ph}^{(2m)} = 6090$ (where $N_{ph}^{(2m)}$ is the number of photons reaching a detector pixel at the reference system length of 2 m) that provided the best match between the simulated noise model and the experiment were obtained through an optimization method based on a χ^2 minimization.

With constant magnification, tube settings and exposure time, and if an integrating detector is used, more compact setups might be preferable.
However, this has a cost in terms of delivered dose, because the sample is brought closer to the source in a situation where a constant number of photons is emitted per unit time. This makes tradeoffs more difficult where dose is an issue, because maximizing sensitivity and minimizing dose impose opposite requirements.
Still in those cases where dose must be kept to a minimum, if a photon counter is available, this makes longer setups more beneficial because the dose can be reduced without this having any negative effect on the system sensitivity.

5

An initial exploration into the possible adaptation of Edge Illumination with laser-plasma sources

5.1 Introduction

In the previous chapters various EI configurations were described, which allow the method's implementation with conventional laboratory sources. This makes EI suitable for use in clinics and hospitals, for which the robustness, flexibility and cost-effectiveness of the setup must be taken into account, while maintaining a high image quality. It was also observed that the capability of the EI approach to provide intense phase contrast signals even with incoherent sources, translates into unprecedented phase sensitivity when the method is implemented with coherent ones [86]. Nevertheless, such highly coherent sources can only be achievable at synchrotron facilities, which are very expen-

sive and have limited access due to the high demand for beam time.

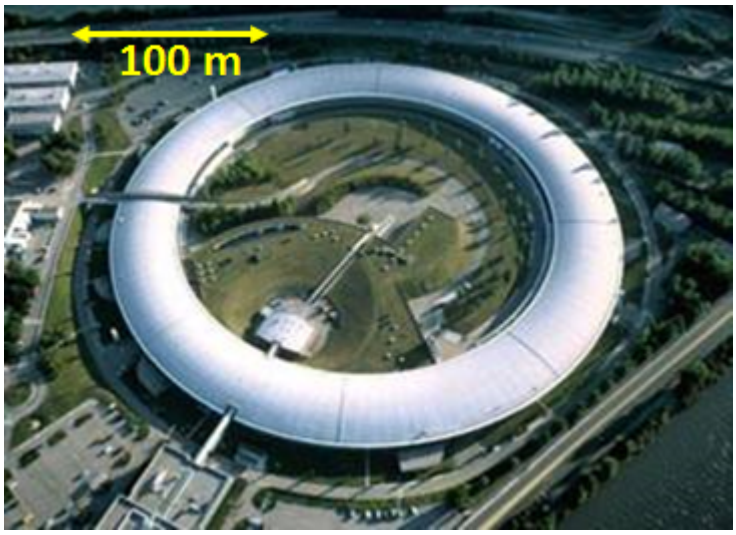

Figure 5.1: Image of the ESRF synchrotron facility in Grenoble (France), where electrons are accelerated in distances of the order of hundreds of metres.

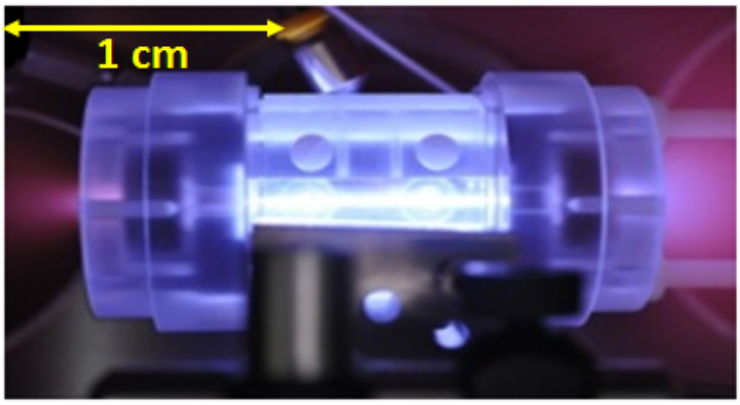

Figure 5.2: Image of a plasma capillary, in which electrons undergo accelerations in cm distances.

The development of Laser-Plasma Wakefield Accelerators (LWFA) [111] represents a possible alternative to synchrotrons. In these novel generation of accelerators, electrons can reach very high energies ($\sim 150\,\mathrm{MeV}$) over very short distances (mm scale) by surfing plasma waves excited by the passage of an ultra-intense laser pulse ($\sim 10^{18}\,W cm^{-2}$).

Electrons in the LWFA can undergo transverse betatron oscillations and emit synchrotron-like radiation, but with a more compact and easily accessible setup. Figs. 5.1 and 5.2 show the dimensions of a synchrotron facility and a laser-plasma source, respectively. The most remarkable properties characterizing the betatron radiation produced by LWFAs are: small source size (μm scale), very short pulse duration (tens of fs) and high peak brilliance (for example, at the Astra-Gemini facility [9], when the laser frequency is a harmonic of the betatron frequency, resonance occurs, leading to a significant increase in photon energy and to a peak brilliance of $\sim 10^{23}\, photons\, s^{-1}\, mrad^{-2}\, mm^{-2}$). This makes the source suitable for applications where high coherence and high flux are needed. The combination of EI with the coherence properties of LWFA could make synchrotron-like performances possible with a much more compact and easily accessible set-up.

In this Chapter the basic principles of a laser plasma source will be described, with particular reference to the LWFA available at the ALPHA-X beamline of the Strathclyde University in Glasgow, where we carried out a proof-of-concept experiment. The initial aim was testing the performance achievable with the combination of the EI method and the LWFA through the acquisition of images of different samples with the portable EI system [87] that I developed (which is described in more detail in Chapter 2). By using appropriate retrieval algorithms [89] to extract information about refraction and dark field signal from the acquired images, I could have also made a comparison with the results achieved by other phase contrast methods and in other EI applications based on different X-ray source technologies.

Unfortunately, non ideal conditions such as instability of the laser and low X-ray flux, did not allow us to obtain images that could be used for a quantitative analysis. Although collection of images was ultimately not possible, the conditions were at least sufficient to allow me to acquire some data in Free Space Propagation (FSP) and make a characterization of the source in terms of flux and spectrum. Thanks to these data, I

was able to discuss the additional requirements that a laser-plasma source should fulfil to enable to perform EI XPC imaging.

5.2 Basic Principles of a Laser Plasma X-ray source

As we already discussed in Chapter 1, there are several ways to produce X-rays. The most common (and cost-effective) is still represented by the X-ray tube, despite its low efficiency in X-rays production (only 1% of the total energy is converted in X-rays, the rest is dissipated as heat) and relatively low brilliance ($10^8 \div 10^9$) $photons\, s^{-1}\, mrad^{-2}\, mm^{-2}$).

Synchrotron sources are characterized by much higher fluxes, with peak brilliances that can be 10 orders of magnitude higher than those achievable with conventional tubes. Furthermore they are characterized by very collimated and highly coherent radiation. The downside is represented by the dimensions and costs of the setup, in addition to their limited access, which prevent the use of such sources in real world application.

LWFAs represent a novel way to produce X-rays, in which synchrotron-like radiation is emitted with a more compact and easily accessible setup. The operation principle was first introduced by Tajima and Dawson [111] and is based on the fact that the passage of an electromagnetic field through a plasma drives electron density oscillations, generating a large amplitude wakefield plasma wave. The plasma electrons can be trapped into the plasma wake and accelerated by its large electrostatic field to very high energies (a few hundreds of MeV) over very short distances (of the order of a millimeter [112]). The ALPHA-X beamline at the Strathclyde University in Glasgow, where we aimed to perform some tests with a portable EI setup [87], is based on this acceleration mechanism.

In the case of LWFA, a high power laser is focused onto an underdense plasma, for which $\omega_0 \gg \omega_p$, where ω_0 is the laser frequency and $\omega_p = \sqrt{\frac{n_p e^2}{\epsilon_0 m_e}}$ the plasma frequency,

with ϵ_0 the vacuum permittivity, e and m_e the charge and mass of the electron, and n_p the electron density. For the laser pulse to be transmitted through the medium, its frequency ω_0 must be such that the electron density n_p is below the critical value $n_c = \left(\frac{\epsilon_0 m_e}{e^2}\right)\omega_0$, above which the plasma is considered overdense and reflects the electromagnetic wave.

For ultrashort laser pulses ($\sim 30\,\text{fs}$), a particularly efficient mechanism for wakefield generation occurs, called the forced laser wakefield regime [113, 114].

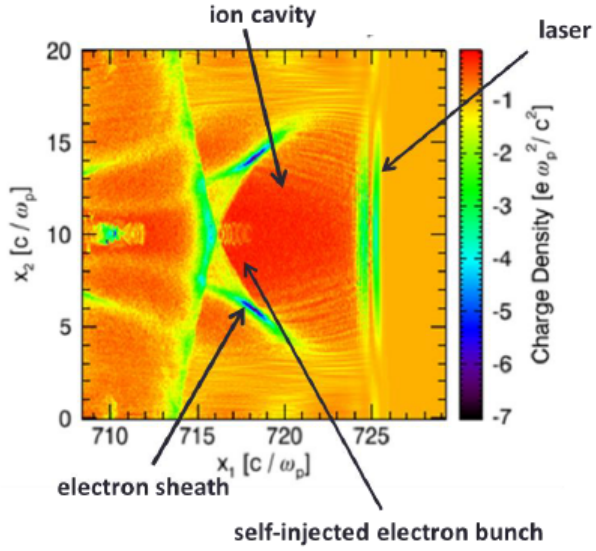

Figure 5.3: Simulation [4] showing three density regions: ion cavity behind the laser pulse, high density electron sheath and self-injected electrons.

In this regime, the plasma wake created by the intense electrostatic field of the laser has an electron depression right behind the laser pulse, leading to the formation of the so called *ion cavity* (or *ion bubble* [114]), in which the positive ions are separated from the electrons, as shown in Fig.5.3. A huge gradient is created between the back of the wake, where there are many electrons, and the middle of the wake, where there are mostly ions. Electrons between these two areas will be accelerated towards the center

of the wake, in a "self-injection" mechanism.

While the electrons are accelerated in the forward direction, their transverse momentum and the strong radial electrostatic field created by the charge displacement lead to transverse betatron oscillations [115] at a frequency $\omega_b = \frac{\omega_p}{\sqrt{2\gamma}}$, where ω_b is the plasma frequency and γ the relativistic Lorentz factor of the electron.

The mechanism behind betatron emission, shown if Fig. 5.4, is similar to the one that leads to the production of synchrotron radiation through a wiggler.

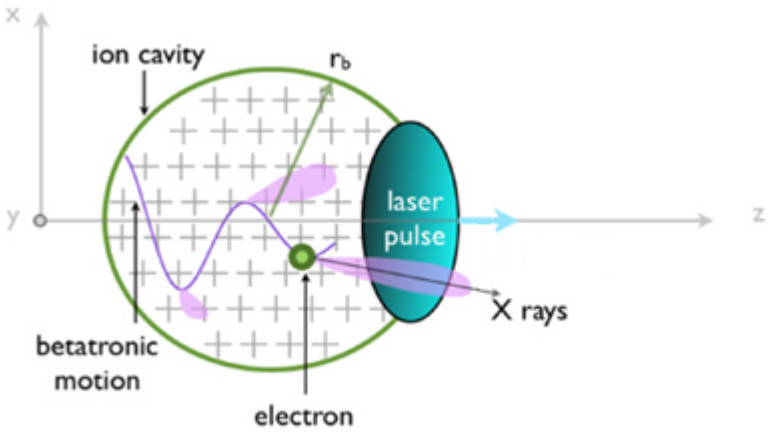

Figure 5.4: Schematic representation [5] of the synchrotron-like radiation emitted by an electron when undergoing transverse betatron oscillations in a laser-produced ion bubble.

In the case of LWFAs, the laser-plasma itself simultaneously plays the role of both accelerator and wiggler. Moreover, because the period of the oscillations can be much shorter in a laser-plasma interaction (micron-scale length) than in a synchrotron based on fixed magnets (centimeter-scale length), the distance required to produce a bright X-ray beam is much shorter (on the scale of millimeters, rather than metres). Also, the required energy of the electron beam is much lower (MeV, rather than GeV).

Another interesting feature of the betatron X-ray beam is its femtosecond pulse duration, which can be used in a wide variety of applications where motion blur is a

problem: this is much harder to achieve with conventional synchrotron sources.

The characteristics of the betatron emission depend on the amplitude of the betatron oscillations r_β. For small betatron oscillations, the radiation is emitted at the fundamental frequency $\omega = \sqrt{2}\gamma^{\frac{3}{2}}\omega_p$. When the amplitude of the oscillations is large, the emitted spectrum is broadband and extends up to a critical energy after which it drops exponentially.

An example of emission spectrum with 4.1 keV critical energy, obtained at the ALPHA-X beamline, is shown in Fig. 5.5.

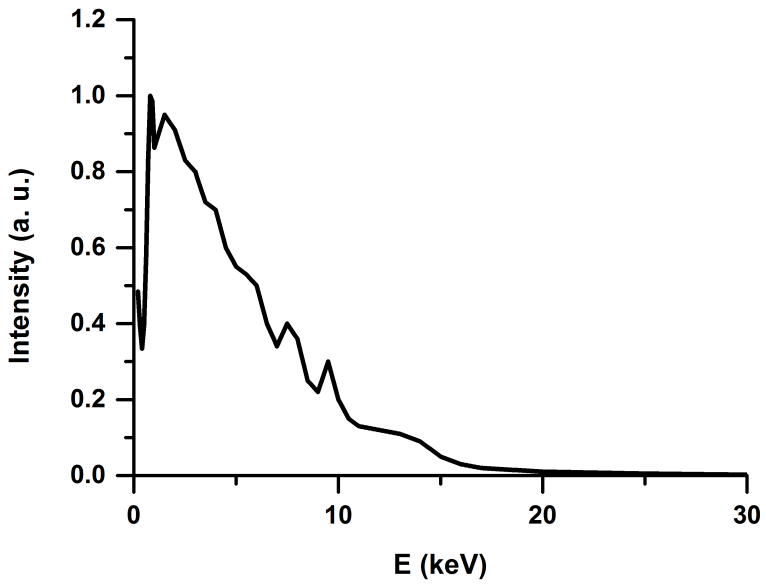

Figure 5.5: Spectrum of betatron radiation with 4.1 keV critical energy, measured at the ALPHA-X beamline.

A huge improvement in terms of flux and peak brilliance can be reached at 100 TW-scale laser systems such as ASTRA-Gemini, at the Rutherford Appleton Laboratory, where a resonant enhancement of the betatron amplitude (i.e. when the laser frequency is a harmonic of the betatron frequency) can lead to critical energies in the range (50÷450 keV) [9].

5.2.1 The LWFA source at Strathclyde

In this section we describe the main properties of the ALPHA-X laser wakefield accelerator beamline at the University of Strathclyde, used to produce betatron X-ray radiation [116]. We report also on the main parameters characterizing the electron beam and the X-ray betatron radiation, as measured by Reboredo et al. (2015)[85], which can be used as a reference to establish the optimal conditions to perform an experiment with the portable EI setup.

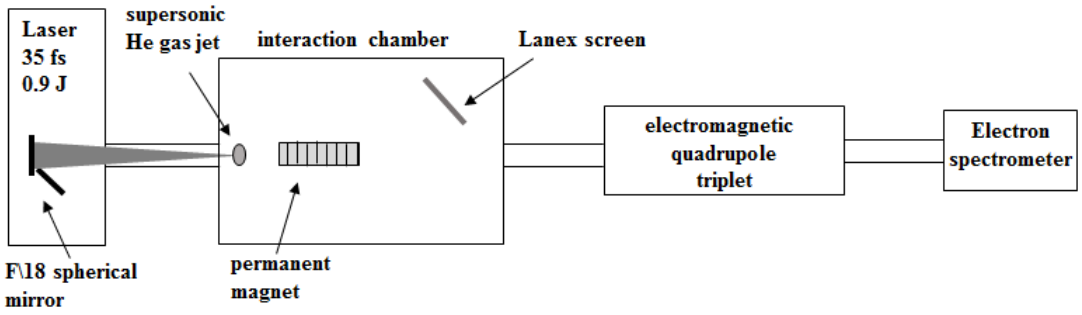

Figure 5.6: Setup of the ALPHA-X bemaline at Strathclyde.

Fig. 5.6 shows a schematic of the setup at the ALPHA-X beamline. A Ti:sapphire laser pulse of 35 fs duration, energy of 1.6 J, and a spectrum centered at 800 nm, is focused onto a spot diameter of 40 μm at the entrance of a 2.7 mm diameter pulsed supersonic helium gas jet. The laser peak intensity is I = 2×10^{18} Wcm^{-2} on the target [85].

The target of the experiment is helium, injected through a nozzle in synchronism with the laser. The latter completely ionizes the gas, creating a plasma with typical densities of the order of $10^{19}\, electrons \cdot cm^{-3}$.

A bending magnet of 0.7 T is placed inside the interaction chamber just after the gas-jet, deflecting the electrons toward a scintillating LANEX phosphor screen (used

to measure their transverse properties such as the beam spatial profile) and allowing only the betatron X-rays to propagate along the beamline and be detected. When the electron beam is used and/or studied, a magnetic quadrupole (see Fig.5.6) is used to collimate the electrons until they reach the electron spectrometer for the diagnostic. Energy measurements result in stable quasi-monoenergetic electron beams of ~ 150 MeV [85].

When the X-ray beam leaves the interaction chamber, it propagates towards two detectors: imaging plates and a semiconductor detector. The formers were used to measure the critical energy of the betatron radiation (i.e. the value of the energy in correspondence of which the area under the spectrum is divided in half) for different plasma densities, obtaining values in the range $(14.9 \div 17.7)$ keV [85]. A decrease in the critical energy is observed by increasing the plasma density: for larger values of the latter, the electron beam energy decreases and, therefore, the critical energy of the betatron X-rays decreases, which provides a simple mechanism for tuning the X-ray source.

A total flux of 10^7 photons/shot was measured [85] by using the Timepix silicon detector, which is a high spatial resolution and high contrast semiconductor detector working in single photon counting mode [117].

The divergence of the X-ray beam was also measured, with obtained values of ~ 40 mrad in the horizontal plane and ~ 35 mrad in the vertical one.

5.2.2 Preliminary XPCi experiment with betatron radiation

Before testing the adaptation of the EI method with the laser-plasma source, a proof-of-principle experiment was carried out by Reboredo et al.(2015) [85] at the APLHA-X beamline of the Strathclyde University, in order to demonstrate the feasibility of using betatron radiation generated by a LWFA source to perform XPCi in its simplest implementation, i.e. free space propagation.

An image of a biological sample (domestic spider) is shown in Fig. 5.7, together with the relative intensity profile of a detail (leg). The image was recorded with an imaging plate and obtained after 300 shots at a repetition rate of 0.33 Hz. The critical energy of the radiation was 15 keV and the magnification of the system was 5.3, with an object-to-detector distance of 4.39 m.

Due to the non ideal experimental conditions such as low flux, the noise level was relatively high. Despite this limitation, details of the sample are clearly visible and edge enhancement is observable, especially in the legs.

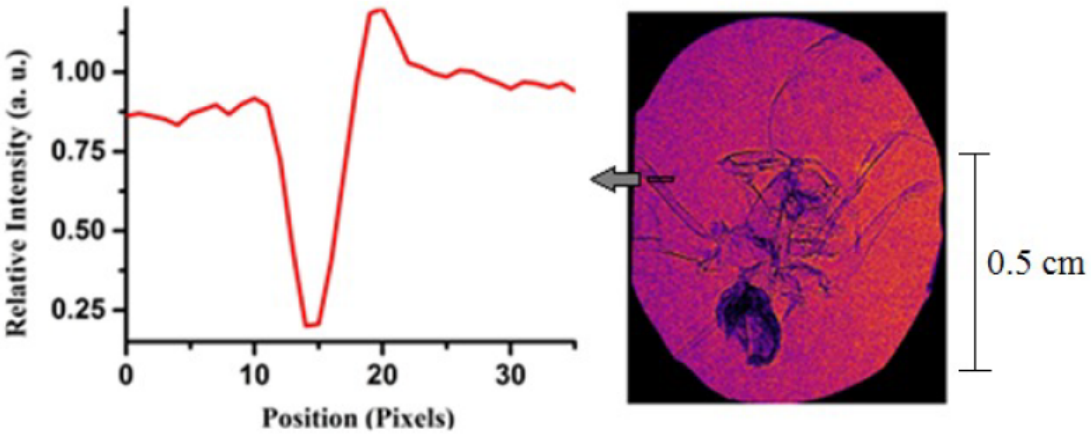

Figure 5.7: X-ray Phase contrast imaging of a spider obtained at the Alpha-X beam line.

A better performance in terms of contrast could be obtained by combining the features of the betatron radiation, such as high coherence and high flux, with the EI method, which was demonstrated to provide a much higher contrast with respect to free-space propagation, especially at high energies [118], and to achieve unprecedented angular sensitivities when used with highly coherent synchrotron radiation [86].

An initial plan to explore this possibility will be described in the next section.

5.3 The experiment and the results

A proof-of-concept experiment was conducted at the ALPHA-X beamline of the Strathclyde University in Glasgow, in order to test the performance of the EI method when used with a laser-plasma source.

In ideal conditions, the laser final energy should be around 1.6 J, with electrons accelerated to $\sim 150\,\mathrm{MeV}$ and a betatron emission spectrum with critical energy up to $\sim 15\,\mathrm{keV}$. Unfortunately, due to instability of the laser (which underwent some upgrade work just a few weeks before our planned experiment), the power was almost half that expected. This was not sufficient to trigger a stable electron acceleration in the plasma (which is a strongly non-linear process) and hence generate betatron radiation with enough flux to perform imaging with the EI method.

The original idea was to use a standard EI setup, consisting of a Hamamatsu C9732DK-11 flat panel detector, two masks (pre-sample mask and detector mask), and the compact piezo-motors [87] (described in Chapter 2) to drive the optical elements. The setup of the laser-plasma source is the one described in Fig. 5.6 of the previous section. The EI setup was assembled in the space between the electromagnetic quadrupole and the electron spectrometer. The detector was, instead, placed just after the electron spectrometer.

Because of the low energy of the laser, the critical energy of the emitted spectrum was expected to be much lower than 15 keV. Hence, for our measurements, we decided to replace the Hamamtsu detector (which is optimized for X-ray energies around 17 keV [119]) with the Andor iKon-M SO detector [6] (13μm pixel size), which is more suitable for lower energies, as can be seen from the quantum efficiency curve shown in Fig. 5.8.

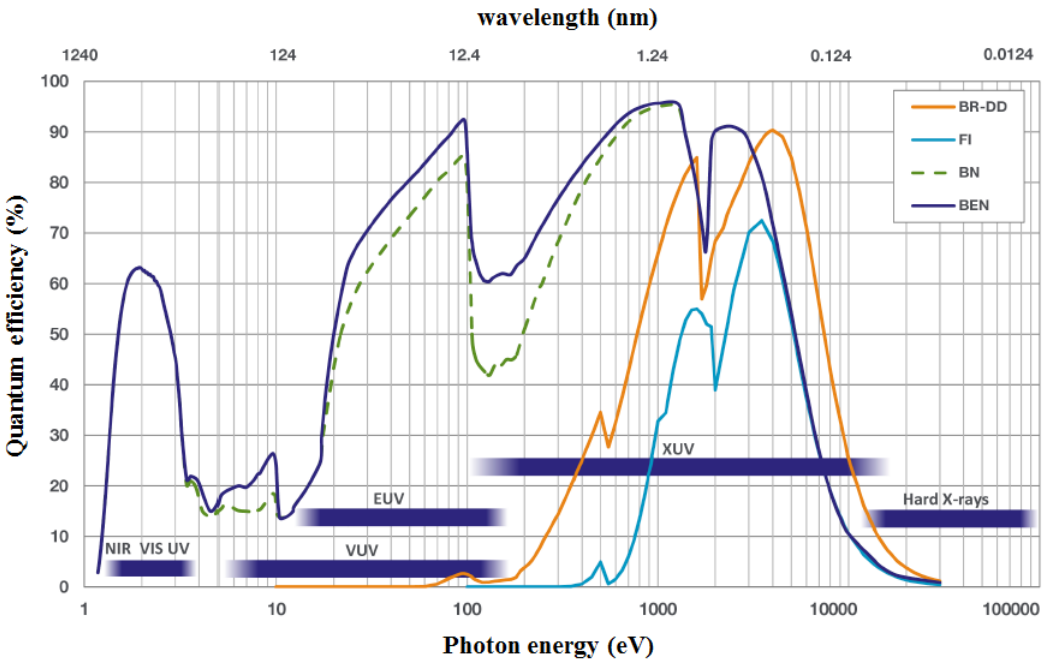

Figure 5.8: Quantum efficiency curves of the Andor detector [6], for different sensor types. In our case, we were using a **BN**: Back Illuminated CCD sensor (dashed green line). The other types are **BEN**: Back-illuminated CCD, enhanced process (dark blue line), **BR-DD**: Back Illuminated, Deep Depletion CCD (orange line) and **FI**: Front Illuminated CCD (light blue line).

Preliminary single shot images were acquired with the Andor camera, without any optical mask or sample in the field of view, in order to evaluate the flux of the source. Fig. 5.9 shows just an example of an image acquired in the conditions described above, together with the intensity profile along a row of detector pixels.

As can be seen, the image is characterized by very few and sparse events corresponding to photons hitting the detector pixels and producing a signal standing out from the background. This made it practically impossible to perform any acquisition with the EI setup because the flux, already very low, would have been attenuated even more by

the graphite substrate of the optical masks. In these conditions, only measurements of the source flux and acquisitions of images in free space propagation (FSP) could be performed.

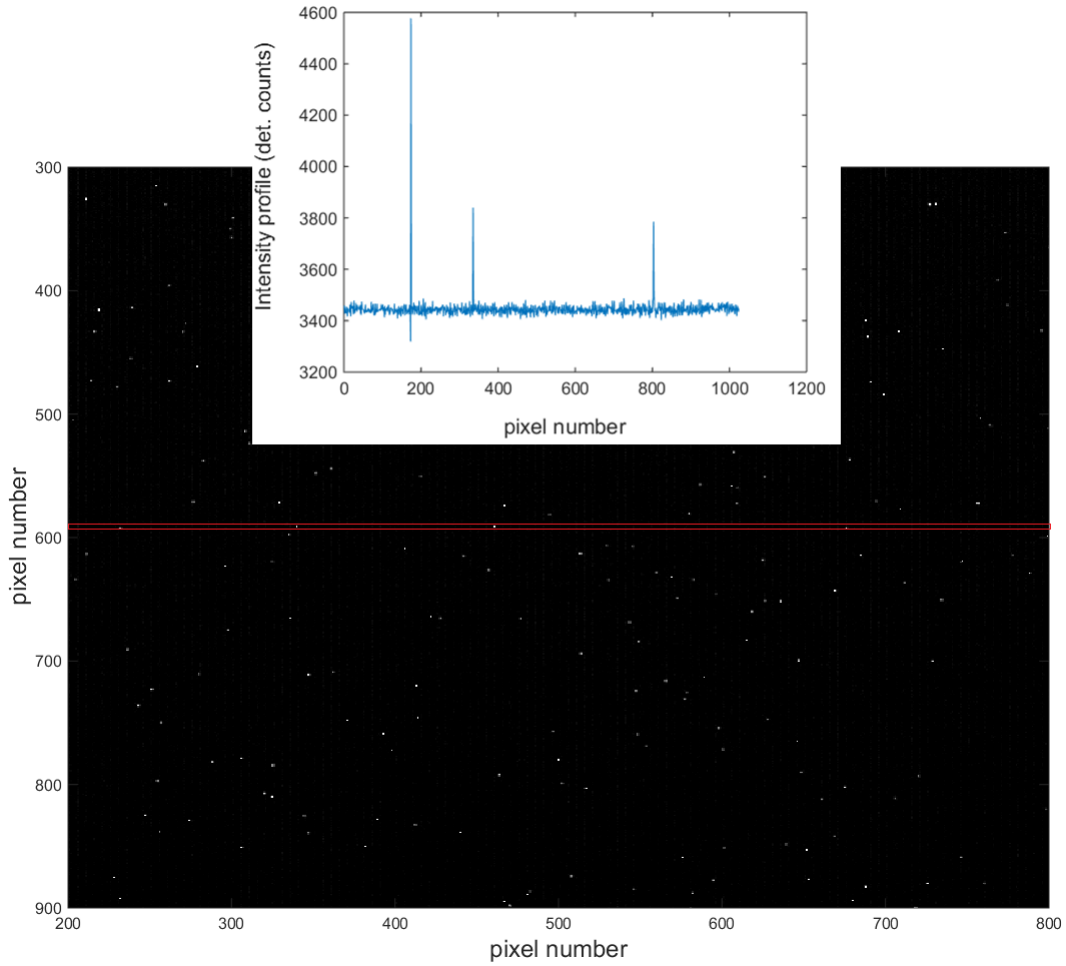

Figure 5.9: Acquired image.

The characterization of the flux and the spectrum of the source was obtained by acquiring a long sequence of images without masks and samples along the beam path. In

optimal conditions, electron bunches should be produced with a regular repetition rate (usually ~ 0.33 Hz [85]), while in our case they were created intermittently and with a much lower frequency. Hence, we had to acquire a large number of frames (500), in order to collect enough statistics to characterize the source.

Our approach to measure the spectrum was based on the assumption that each individual event in a single shot image corresponds to a single photon interaction. Under this assumption, higher values of detected pixel counts correspond to higher energies of the photons hitting the detector. As a first approximation, we did not consider charge sharing between adjacent pixels, which could increase the number of low energy events. By taking a large sequence of images, the number of events above a certain threshold can be counted and their distribution as a function of the pixel content can be obtained. The spectrum of the source can then be measured by converting the detector counts into energy values through the calibration relationship of the Andor camera:

$$en = a + b \cdot counts \tag{5.1}$$

where $a = (-8.1 \pm 0.5)\, keV$ and $b = (0.00487 \pm 0.00015)\, keV/counts$. As all the images in the sequence were dark-field subtracted, the term a in Eq. 5.1 (which takes into account the offset due to dark current) can be neglected.

In order to cut fluctuations due to background noise, a value of the threshold $th = 5\sigma$ was chosen, where $\sigma = 14$ is the measured standard deviation of a small dark region (50x50 pixels) in the acquired images. In each image, only pixels with detected counts above $th = 5\sigma$ were selected, while the value of the other pixels was set to 0.

Unfortunately, only few images in the stack presented a large number of events (i.e. of pixels above th), as shown in the histogram in Fig. 5.10, which represents the number of images containing more than 100 events above the threshold.

Figs. 5.11 and 5.12 show the cases with more than 500 and 1000 events, respectively.

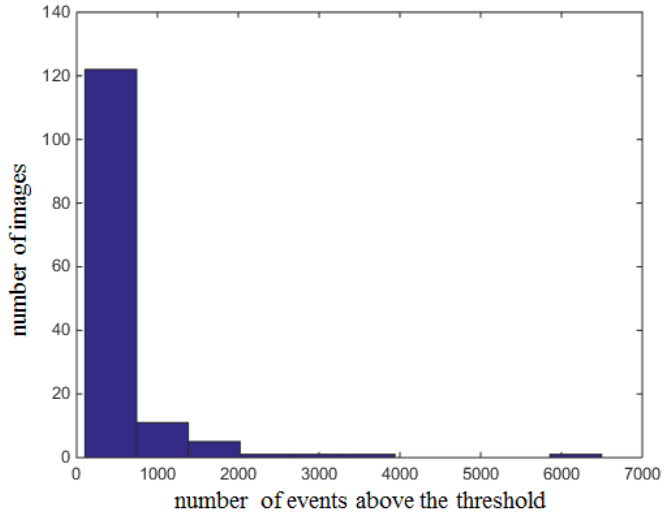

Figure 5.10: Distribution of the images with more than 100 events above the threshold.

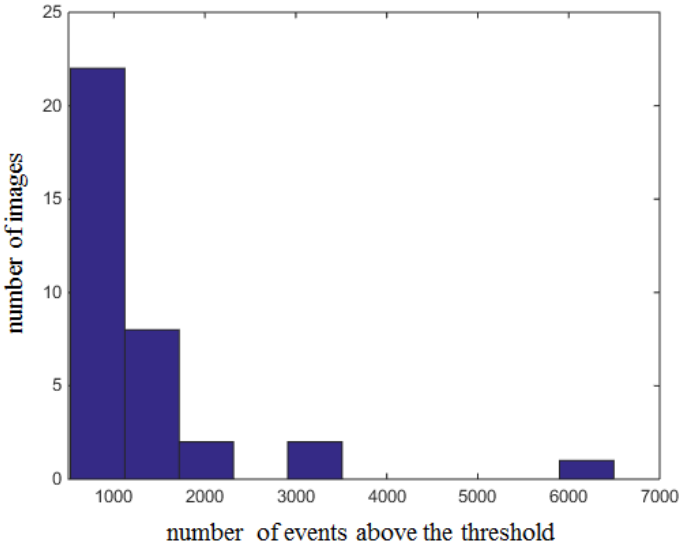

Figure 5.11: Distribution of the images with more than 500 events above the threshold.

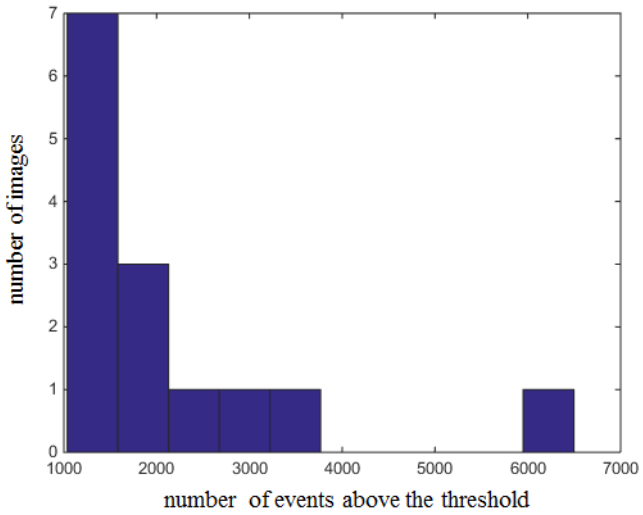

Figure 5.12: Distribution of the images with more than 1000 events above the threshold.

As can be seen from the histograms, the flux of photons produced by the laser-plasma source was very low. In particular, Fig.5.12 shows that only 14 out of the 500 shots counted more than 1000 events. Furthermore, around 10^5 events were counted in the whole stack of images.

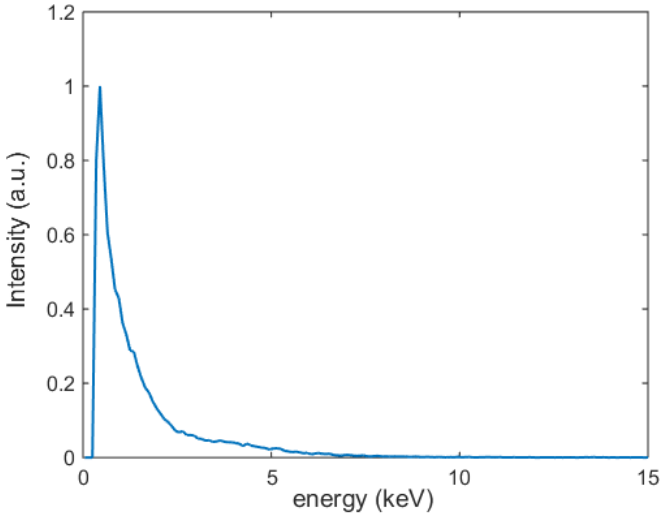

Figure 5.13: Energy spectrum of the laser-plasma source measured at the ALPHA-X beamline.

Following the conversion formula in Eq.5.1, the energy spectrum of the laser plasma source was obtained by plotting the distribution of the total events in the whole stack of images as a function of the energy, as shown in the histogram in Fig. 5.13.

As can be seen, the main contribution to the spectrum is given by photons with energy $< 2\,\text{keV}$ (accounting for around 60% of the entire area under the spectral curve). However, we should note that no correction for possible multiple low energy events generated by charge sharing was applied. This could result in an increased number of events with lower detected counts, which are instead generated by single photon interactions, the signal from which was split between adjacent pixels. By taking this into consideration, multiple events should be counted as one single event with signal equal to the sum of the signals, shifting the spectrum critical energy to higher values. However, by considering that the relative importance of these multiple events with respect to single ones was less than 1% in the acquired images, we can neglect this additional contribution.

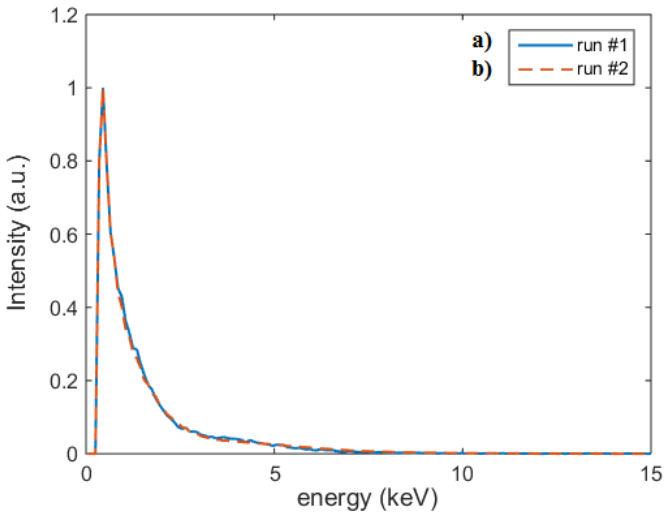

Figure 5.14: Comparison between two different spectra obtained from two independent acquisitions, carried out in the same experimental conditions.

I also compared the spectrum in Fig. 5.13 with the one obtained from the data acquired by the local research group led by Dr. Silvia Cipiccia before our arrival, with the laser operating under the same conditions and with the same acquisition procedure described at the beginning of this section. Fig. 5.14 shows the comparison of the two spectra. The match is good, which supports the reliability of our measurement.
In the next section, we will show an image of a test sample (wires of different material and thickness) acquired in free space propagation (FSP), with the experimental conditions described above.

5.4 Acquisition of wire images

As both the flux and the mean energy of the source were very low, images of test samples were acquired with the simplest possible XPCi setup (i.e. FSP) in order to avoid further attenuation due to the graphite substrate of the masks. The wire sample was placed between the electromagnetic quadrupole and the electron spectrometer, as shown in Fig.5.15.

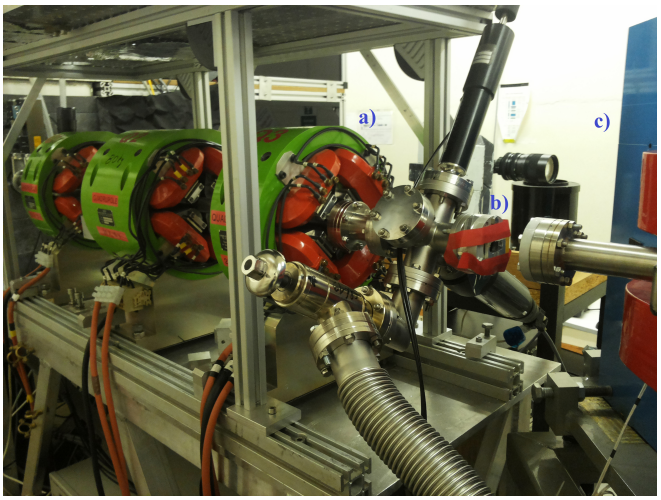

Figure 5.15: Wire sample (b) used for the experiment, placed between the electromagnetic quadrupole (a) and the electron spectrometer (c).

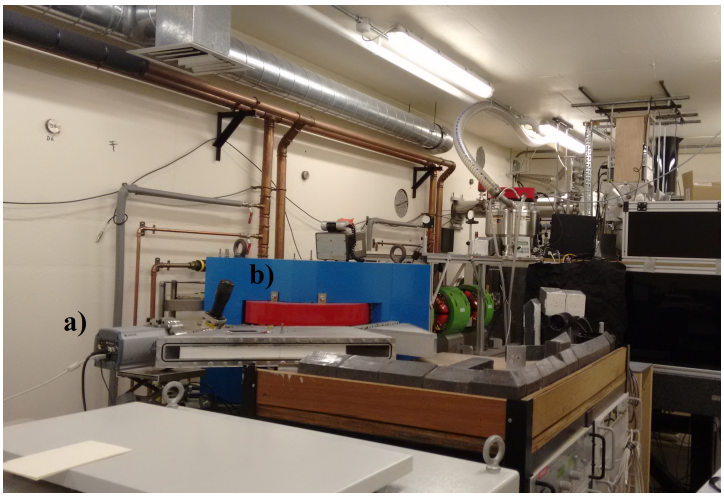

Figure 5.16: Andor detector (a), placed just after the electron spectrometer (b).

The Andor detector was placed just after the electron spectrometer, as shown in Fig.5.16. In this way, the source-to-sample distance was $z_1 = 224\,cm$, while the sample-to-detector distance was $z_2 = 123\,cm$, for a magnification of M = 1.55.

An image of the wire sample, acquired with the experimental conditions described above, is shown in Fig.5.17, with the corresponding intensity profile along a pixel row shown in Fig. 5.18.

Considering the low flux of the source, it was necessary to acquire a sequence of 5000 frames (with 200 ms exposure time per frame), which were then summed in order to have a final image with a better statistics. The same threshold of 5σ that was used to obtain the spectrum in Fig.5.13 was applied to all frames, in order to cut the noise due to the detector. Despite the large number of acquired frames, the image still looks very noisy, as can be seen from the figure.

After measuring the attenuation coefficient of each wire from the contrast in the intensity profile, the corresponding effective energy of the X-ray beam was retrieved, with

an obtained average value of (5.4 ± 0.5) keV.

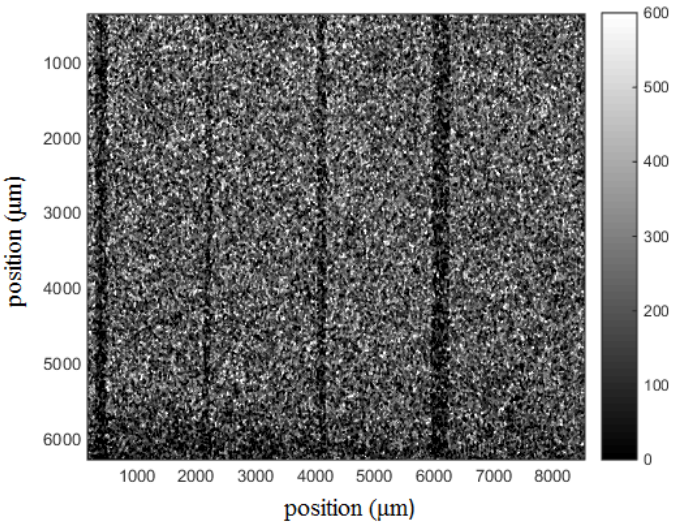

Figure 5.17: Image of the wire sample acquired in FSP with the laser plasma source at the APLHA-X beamline. From left to right, materials and thicknesses of the wires were: boron (200 μm diameter with 14 μm tungsten core); PET (Polyethylene terephthalate, 100 μm); PEEK (Polyetheretherketone, 150 μm); nylon (300 μm).

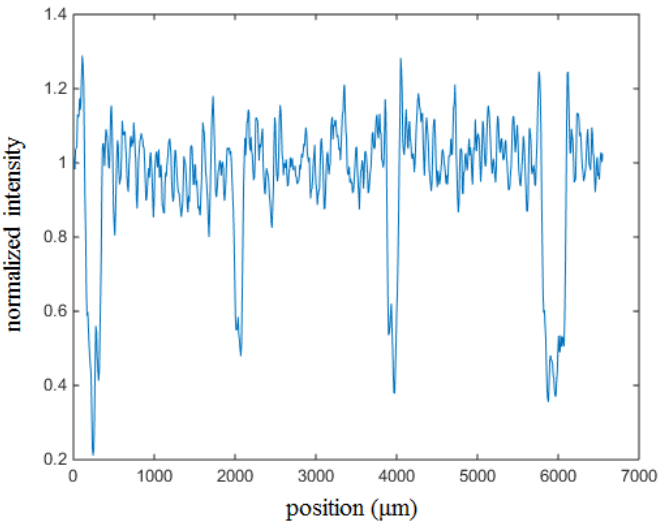

Figure 5.18: Intensity profile of wires sample acquired in FSP with the laser plasma source at the APLHA-X beamline.

The intensity profile of the nylon wire was compared with the one obtained from a monochromatic simulation in free space propagation, as shown in Fig. 5.19.

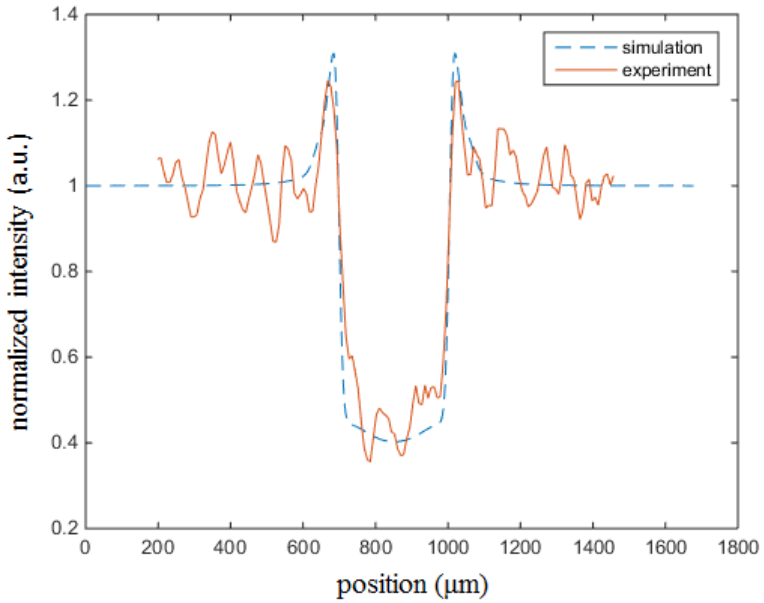

Figure 5.19: Comparison of the experimental intensity profile (solid red line) of a nylon wire with the one obtained through the simulation (dashed blue line).

The best match with the experiment was obtained by using an effective energy of 5.1 keV (compatible with the value obtained by the measurement of the attenuation coefficient of the materials), a detector point spread function (PSF) equal to the pixel size of 13μm (considering that a direct conversion detector was used) and a Gaussian distributed extended source of FWHM = 50μm. In principle, the source size of a laser plasma source should be of the order of <10μm [120] for single shot images. However, due to the instability of the laser, the position of the focal spot typically changes from one shot to another, causing an enlargement of the effective source size. Hence, the obtained value of 50μm can be considered an estimate of the laser-plasma source spatial distribution, in the case of multiple acquired shots.

5.5 Conclusions

After considering the results of the above analysis and making reference to the source characterization described in Reboredo et al.(2005) [85], we can establish some basic requirements that should be achieved in order to perform EI XCPi with the laser-plasma source at the ALPHA-X beamline in Glasgow:

First of all, the final energy of the laser should be 1.6 J (0.9 J on target), in order to accelerate electrons bunches in an underdense plasma at energies high enough to produce betatron radiation in an efficient way.

Second, in order to collect a sufficient statistics within a reasonable exposure time, the flux of the source should be at least equal to 10^7 photons per shot, and the repetition rate should be at least equal to the one achieved so far by the Strathclyde group, which is $0.33\,Hz$. By assuming that all the photons produced during a single shot are collected by a detector of 1024x1024 pixels (with a pixel size of 13μm), this would result in around 10 photons per pixel. In order to have 3% Poisson noise (when using a photon counting detector), which corresponds to 1000 photons per pixel, at least 100 shots are required. Hence, with a repetition rate of $0.33\,Hz$, this would give an exposure time of about 5 minutes, which is not compatible with clinical applications. In this case, the repetition rate should be increased at least by a factor 5 (with the same flux), in order to keep the exposure time below 1 minute. However, for EI, one should also consider the flux losses due to the masks open fraction (i.e. aperture/pitch), which is typically of the order of 1/5, and to the misalignment between the two masks (typically used at 50% illumination level), which reduces the flux by another factor of 2. Assuming substrate-free masks, this would make an additional increase of the repetition rate by a factor 10 necessary, which might have to be increased further if a substrate is indeed

present.

Finally, the critical energy of the betatron radiation can be tuned from a few keV to tens of keV. In principle, with a standard EI setup based on optical masks with a graphite substrate (which stops low energy photons) and using a detector like a Hamamatsu C9732DK-11 (which is not sensitive to photons with energies below $7\,keV$), a critical energy of 15-20 keV would be ideal, if one considers clinical applications such as mammography, where low energy photons stopped inside the patient must be removed from the spectrum by means of appropriate filtering. However, by using masks without graphite substrate and a different detector, such as the Andor camera (which is sensible to lower energies), values of 4-5 keV in critical energy could be acceptable in ex-vivo studies where dose is not an issue (e.g. imaging soft biological tissue specimens or "digital histology" [77]).

Conclusions

In this thesis we developed new and different laboratory implementations of the Edge Illumination (EI) X-Ray Phase Contrast imaging (XPCi) method, with the main aim of facilitating and accelerating its commercial translation.

The high potential of XPCi and its capability to represent a means to solve the basic problems of absorption-based techniques has been demonstrated during recent years and has been discussed in Chapter 1, together with a review of the most widely used XPCi techniques. Among them, our group focusses on EI, for reasons related to its full achromaticity, compatibility with divergent X-ray beams and tolerance to misalignment/vibrations of the optical elements. These features make EI suitable for adaptation with conventional X-ray sources, even though the ultimate performance depends on the source characteristics, which need to be studied.

For this reason, we developed a portable and compact system that enables the easy transportation of the setup to different scientific environments (e.g. labs and hospitals), where novel X-ray sources are being developed. The system, described in full detail in Chapter 2, is based on miniaturised and highly precise piezoelectric motors, which are lighter while remaining as accurate as the stepper motors used so far to move the optical masks composing the standard EI setups. Because of their small dimensions (few cm) and of the limited load that they can support ($\sim$ 1 Kg), the piezo-motors are suitable in particular for small and light samples, while stepper motors might be preferable when a higher robustness is required.

A Labview code was implemented and integrated with the data acquisition software, in order to drive the motors in an automated way and finely adjust their positions through a closed loop procedure, which utilises their built-in sensors. In order to guarantee the portability of the entire system, the code is run on a laptop.
After having obtained positive results from the preliminary tests carried out to evaluate the accuracy of the software procedure when moving the motors to absolute positions, the performance of the portable system was quantitatively compared with that of the old system based on stepper motors. Images of wire samples were acquired with both systems and the corresponding angular sensitivity in the refraction signal was evaluated. A value of (270 $\pm$ 6) *nrad* was obtained with the portable system, which is comparable, within the experimental error, with the value of (260 $\pm$ 10) *nrad* achieved with the previous system.
This result shows that a light and compact system based on piezo-electric motors, while enabling the easy transportation of the EI setup, can guarantee the same performance in terms of angular sensitivity as the one obtained so far with systems based on bulkier and heavier stepper motors. In addition to the easy adaptability of EI to various types of laboratory sources, this makes the method more easily adaptable to a wider variety of real-world applications.

Still on the commercial translation aspect, an important aspect that must be taken into account is the cost of the X-ray sources used for EI setups currently under development at University College London. Such high-powered sources (e.g. Rigaku M007 or Rigaku M009) are, in fact, able to generate very high fluxes from sufficiently small focal spots (around 70-100 μm), compatible with the requirements of EI. Nevertheless, these sources are very expensive, which can represent a limitation for the method's implementation into clinical environments, since in that case costs must be contained. In addition, typical dimensions of EI setups so far ranged between 1.5 and 2 m, which

can pose a hurdle for applications where available space is limited.

For these reasons, in Chapter 3 we presented an alternative EI implementation that simultaneously allows the use of cheaper X-ray sources and the realisation of more compact setups. This can be realized by the introduction of a "source mask", the function of which is to section the large focal spot of a conventional X-ray source into multiple sub-sources. These create a corresponding number of spatially shifted images, which need to be disentangled by means of appropriate algorithms. Refraction images of test samples acquired with this new configuration were successfully restored by using a Richardson-Lucy deconvolution method with a total variation regularization approach, and their corresponding intensity profiles were compared with simulated ones obtained by using only one source, providing a very good match. The approach was tested, with positive results, also on a more complex biological sample.

Hence, despite some non-ideal conditions in the developed proof-of-concept setup, such as low flux and thin pre-sample mask that negatively affected the signal-to-noise ratio of the acquired images, this experiment was sufficient to prove that sectioning a large focal spot by means of a "source mask" is a valid approach in EI. This provides the possibility to exploit cheap laboratory X-ray sources and, at the same time, to realize more compact setups, since the individual "sub-sources" created through the source mask can be smaller than our current standard of 70-100μm, which allows for a different approach to the design of the system.

The aspect of reducing the dimensions of a standard EI system was explored more in detail in Chapter 4 through a quantitative study focused on the dependence of the angular sensitivity on the distance between X-ray source and detector, at constant system magnification, tube settings and total exposure time. The results of this analysis can be used to design more compact systems which, combined with the use of light and highly precise piezo-motors, makes EI more flexible and therefore suitable for a much

wider range of applications.

From preliminary studies carried out through a simulation based on the assumption that Poisson fluctuations are the only source of noise in the images, the system's angular sensitivity resulted to be constant within the range of investigated distances (0.5 $\div$ 3) m, suggesting the possibility to reduce the setup dimensions without any loss in terms of image quality, at least for applications where the dose delivered to the sample is not an issue. Combined with the use of light and small piezo-motors, this result could in principle allow the development of extremely compact imaging systems, down to a few tens of cm.

However, the assumption of Poisson distributed noise, on which the simulation framework was based, is verified only if a photon counting detector is used. As the latter was not available for our tests, an integrating detector was used instead in the experimental validation, leading to a mismatch with the simulated results. In contrast with the expected constant behaviour observed in the simulation, the standard deviation extracted from background regions of experimental refraction images increased with the distance, indicating a reduction in angular sensitivity with increased system length.

This mismatch can be explained by including a constant term σ_{dark} due to the dark current in the model that describes the noise behaviour of an integrating detector. After repeating the simulation with the new model, the best match with the experiment was reached by using the values $\sigma_{dark} = 107$ and $N_{ph}^{(2m)} = 6090$, where $N_{ph}^{(2m)}$ is the number of photons reaching a detector pixel at the reference system length of 2 m. This result was obtained through an optimization method based on a χ^2 minimization.

The results show that, when system magnification, tube settings and exposure time are kept constant, more compact setups might be preferable if an integrating detector is used, at least when sample dose is not an issue. On the other hand, in cases where dose must be kept to a minimum, the use of a photon counter makes longer setups more convenient because it allows to reduce the dose without negatively affecting the system

sensitivity.

Finally, in Chapter 5 we explored the possibility of adapting EI to different X-ray source technologies. While it has been shown that the method is capable to provide unprecedented phase sensitivities when implemented with highly coherent sources, at the moment these are only available at synchrotrons, which are characterized by very high costs/dimensions and have limited access. This triggered research into the development of alternative X-ray sources that can provide similar performances but with a more compact and easily accessible setup.

An example of this new generation of "exotic" X-ray sources is provided by Laser-Plasma Wakefield Accelerators (LWFA), in which electrons are accelerated to energies of the order of hundreds of MeV over distances of centimetres in plasma waves generated by the passage of an ultra-dense laser. The electrons can emit synchrotron-like radiation (called betatron radiation), with typical source sizes of the order of microns and very high peak brilliance (up to $\sim 10^{23}\, photons\, s^{-1}\, mrad^{-2}\, mm^{-2}$).

A proof-of-concept experiment was carried at the ALPHA-X beamline at the University of Strathclyde in Glasgow, in order to evaluate the performance of a system realized through the combination of a standard EI setup and the laser-plasma source developed by the local group.

The non ideal conditions encountered during the experiment, such as instability of the laser, affected the performance of the source and did not allow to perform the acquisition of XPCi data with the EI method. Due to these conditions, it was only possible to image a wire phantom using free space propagation (FSP) XPCi, and a characterization of the source in terms of flux and emitted spectrum was undertaken as well.

The experimental intensity profiles were matched to those obtained from a monochromatic simulation that used an effective energy of 5.1 keV, a detector point spread function (PSF) of 13μm (equal to the pixel size that was effectively used), and a Gaussian

distributed source with FWHM = 50μm. The latter can be considered an estimate of the source size in the case of multiple acquired shots: while in a single shot the source is expected to be smaller, its position is not constant from one shot to another.
Our source characterization was compared with one performed by the local group at the ALPHA-X beamline in Glasgow when the laser was running properly, in order to establish some basic requirements that must be satisfied in order to guarantee a sufficient performance to enable using EI XCPi with the laser-plasma source. From the analysis, we concluded that a laser power of around 1.6 J, photon flux of 10^7 photons per shot and a constant repetition rate of 0.33 Hz would be necessary to collect a sufficient statistics within reasonable exposure times. However, for more challenging applications, the repetition rate should be increased at least by a factor 5 while keeping the flux constant, in order to keep the overall exposure time below 1 minute, if a FSP setup is used. For EI, a further increment of the repetition rate at least by a factor 10 would be necessary, in order to compensate flux losses due to the masks open fraction (typically 1/5) and to the misalignment between the two masks (typically used at 50% illumination level), assuming masks without substrate.
Clinical applications would also require a higher X-ray energy, e.g. for mammography, a critical energy of 15-20 keV for the betatron radiation would be needed. However, for applications where delivered dose is not an issue (e.g. specimen or biopsy imaging), the current 4-5 keV could be acceptable, if a setup based on masks without graphite substrate and a detector sensible to low energies (e.g. Andor iKon-M SO) was used.

The results presented in this work can be considered as a positive indication that the realization of more compact, easily portable and cost-effective setups can open the way to the commercial translation of the EI XPCi method in real world application. Further improvements might though require to target some limits of the presented approaches (e.g. the possibility to scan only light and small samples due to the small

dimensions of the portable system; the flux losses resulting from the use of the source mask; the possibility to use more compact setups only in applications where delivered dose is not an issue).

These requirements can drive and inform the next steps of the research and development needed to translate EI XPCi into real world applications.

References

[1] http://www.smaract.com. 12, 63, 64

[2] K. Ignatyev P. Munro R. Speller and A. Olivo. **Effects of signal diffusion on x-ray phase contrast images**. *Rev. Sci. Instr.*, **82**:073702, 2011. 14, 48, 59, 87, 88, 97, 99, 109

[3] F.A. Vittoria P.C. Diemoz M. Endrizzi L. Rigon F.C. Lopez D. Dreossi P.R.T. Munro and A. Olivo. **Strategies for efficient and fast wave optics simulation of coded-aperture and other x-ray phase-contrast imaging methods**. *Appl. Opt.*, **52**:6940, 2013. 15, 81, 85, 86, 87, 98, 109

[4] A. Subiel D.A. Jaroszynski G.H. Welsh. *PhD Thesis: Feasibility Studies on the Application of Relativistic Electron Beams from a Laser Plasma Wakefield Accelerator in Radiotherapy.* Physics Department, University of Strathclyde, 2014. 18, 129

[5] S. Corde et al. **Betatron emission as a diagnostic for injection and acceleration mechanisms in laser plasma accelerators**. *Plasma Phys. Control. Fusion*, **54**:124023, 2012. 18, 130

[6] http://www.andor.com/pdfs/specifications/Andor_High_Energy_iKonM_SO.pdf. 18, 135, 136

[7] D. McMorrow and J. Als-Nielsen. *Elements of Modern X-ray Physics.* Wiley, 2011. 25, 29, 30, 32

[8] D.M. Paganin. *Coherent X-Ray Optics.* Oxford Science Publication, 2006. 26, 28, 29, 32

[9] S. Cipiccia et al. **Gamma-ray production from resonant betatron oscillations in plasma wakes**. *Nature Physics*, **7**:867–871, 2011. 26, 127, 131

[10] T.S. Curry J.E. Dowdey R.C. Murry. *Physics of Diagnostic Radiology.* Lea & Febiger, 1990. 26, 27, 32

[11] S. Webb. *Webb's Physics of Medical Imaging.* CRC Press, New York, 2012. 29, 34, 35

[12] H. Winick. **Synchrotron radiation sources (a primer)**. *World Scientific*, 1995. 29

[13] M.J. Yaffe and J.A. Rowlands. **X-ray detectors for digital radiography**. *Med. Phys.*, **42**:1, 1997. 35, 50

[14] G.N. Hounsfield. **Computerized transverse axial scanning (tomography): Part 1. Description of system**. *Br. J. Radiol.*, **46**:1016, 1973. 35, 50

[15] J. Ambrose. **Computerized transverse axial scanning (tomography): Part 2. Clinical application**. *Br. J. Radiol.*, **46**:1023, 1973. 35, 50

[16] J.F. Braislford. **Roentgen's Discovery of X rays. Their Application to Medicine and Surgery**. *Br. J. Radiol.*, **19**:453, 1946. 35

[17] S. Wilkins T. Gureyev D. Gao A. Pogany and A. Stevenson. **Phase-contrast imaging using polychromatic hard X-rays**. *Nature*, **384**:335–338, 1996. 36, 37, 38, 50, 86

[18] A. Olivo. **Recent Patents in X-Ray Phase Contrast imaging**. *Recent Patents on Biomedical Engineering*, **3**:95–106, 2010. 36, 39, 40, 47

[19] M. Born and E. Wolf. *Principles of Optics.* Pergamon, Oxford, 1980. 37, 86

[20] A. Sinigrev I. Snigireva V. Kohn and I. Schelokov. **On the possibilities of x-ray phase contrast microimaging by coherent high-energy synchrotron radiation**. *Rev. Sci. Instr.*, **66**:5486–5492, 1995. 37, 50, 80, 86

[21] F. Arfelli M. Assanted V. Bonvicini A. Bravin G. Cantatore E. Castelli L. Dalla Palma M. Di Michiel R. Longo A. Olivo S. Pani D. Pontoni P. Poropat

M. Prest A. Rashevsky G. Tromba A. Vacchi E. Vallazza and F. Zanconati. **Low-dose phase contrast x-ray medical imaging**. *Phys. Med. Biol.*, **43**:2845, 1998. 37, 38

[22] A. Olivo and R.D. Speller. **Deconvolution of x-ray phase contrast images as a way to retrieve phase information lost due to insufficient resolution**. *Phys. Med. Biol.*, **54**:N347, 2009. 38, 103

[23] L. De Caro F. Scattarella S. Tangaro D. Pelliccia C. Giannini U. Bottigli and R. Bellotti. **Deconvolution by finite-size-source effects of x-ray phase-contrast images**. *Med. Phys.*, **38**:1951, 2011. 38, 103

[24] K.A. Nugent T.E. Gureyev D.F. Cookson D. Paganin and Z. Barnea. **Quantitative Phase Imaging Using Hard X Rays**. *Phys. Rev. Lett.*, **77**:2961, 1996. 38

[25] T.E. Gureyev and S.W. Wilkins. **Quantitative in-line phase-contrast imaging with multienergy X rays**. *Phys. Rev. Lett.*, **86**:5827, 2001. 38

[26] T.E. Gureyev S. Mayo S.W. Wilkins D. Paganin and A.W. Stevenson. **On x-ray phase imaging with a point source**. *J. Opt. Soc. Am.*, **15**:579, 1998. 38

[27] P. Cloetens W. Ludwig and J. Baruchel. **Holotomography: Quantitative phase tomography with micrometer resolution using hard synchrotron radiation x rays**. *Appl. Phys. Lett.*, **75**:2912, 1999. 38

[28] D. Paganin S.C. Mayo T.E. Gureyev P.R. Miller and S.W. Wilkins. **Simultaneous phase and amplitude extraction from a single defocused image of a homogeneous object**. *J. Microsc.*, **206**:33, 2002. 38

[29] P. Cloetens M. Pateyron-Salom J.Y. Buffiere G. Peix J. Baruchel F. Peyrin and M. Schlenker. **Observation of microstructure and damage in materials by phase sensitive radiography and tomography**. *J. Appl. Phys.*, **81**:5878, 1997. 38

[30] J.Y. Buffire E. Maire P. Cloetens G. Lormand and R Fougeres. **Characterization of internal damage in a MMC p using X-ray synchrotron phase contrast microtomography**. *Acta mat.*, **47**:1613, 1999. 38

[31] A.V. Bronnikov. **Theory of quantitative phase-contrast computed tomography**. *J. Opt. Soc. Am*, **19**:472, 2002. 38

[32] P. Suortti and W. Thomlinson. **Medical applications of synchrotron radiation**. *Phys. Med. Biol.*, **48**:R1, 2003. 38

[33] A. Bravin P. Coan and P. Suortti. **X-ray phase-contrast imaging: from preclinical applications towards clinics**. *Phys. Med. Biol.*, **58**:R1, 2013. 38, 40

[34] M. Di Michiel A. Olivo G. Tromba F. Arfelli V. Bonvicini A. Bravin G. Cantatore E. Castelli L. Dalla Palma R. Longo S. Pani D. Pontoni P. Poropat M. Prest A. Rashevsky A. Vacchi E. Vallazza. **Phase Contrast Imaging in the Field of Mammography**. *Med. Appl. Synchr. Rad.*, page 78, 1998. 38

[35] U. Bonse and M. Hart. **An X-ray interferometer**. *Appl. Phys. Lett.*, **6**, 1965. 39, 50, 80

[36] U. Bonse and M. Hart. **An X-ray interferometer**. *Appl. Phys. Lett.*, **7**, 1965. 39

[37] H. Wen A.A. Gomella A. Patel S.K. Lynch N.Y. Morgan S.A. Anderson E.E. Bennett X. Xiao C. Liu D.E. Wolfe. **Subnanoradian X-ray phase-contrast imaging using a far-field interferometer of nanometric phase gratings**. *Nat. Commun.*, **4**:2659, 2013. 40

[38] A. Momose. **Demonstration of phase-contrast x-ray computed-tomography using an x-ray interferometer**. *Nucl. Instrum. Methods A*, **352**:622, 1995. 40

[39] A. Momose. **Phase-sensitive imaging and phase tomography using x-ray interferometers**. *Opt. Express*, **11**:2303, 2003. 40

[40] A. Momose. **Recent advances in x-ray phase imaging**. *Japan J. Appl. Phys.*, **44**:6355, 2005. 40

[41] M. Ando K. Hyodo H. Sugiyama A. Maksimenko W. Pattanasiriwisawa K. Mori J. Roberson E. Rubenstein Y. Tanaka J.Y. Chen D.C. Xian and X.W. Zhang. **X-Ray Optics 'Owl' and 'Trinity'**. *Japan J. Appl. Phys.*, **41**:4742, 2002. 40

[42] A. Maksimenko M. Ando H. Sugiyama W. Pattanasiriwisawa and K. Hyodo. **A Test of an X-Ray Quatrochrome Interferometer for Simultaneous Observation of Images Due to Dark- and Bright-Field, Phase-Interference and Absorption Contrasts**. *Japan J. Appl. Phys.*, **42**:L 1096, 2003. 40

[43] L.V. Azarov. *Elements of X-ray crystallography.* Mc Graw-Hill, New York, 1968. 40

[44] Z. Pinskers. *Dynamical Scattering of X-rays in Crystals.* Springer, Berlin, 1978. 40

[45] V. Ingal and E. Beliaevskaya. **X-ray plane-wave topography observation of the phase contrast from a non-crysttaline object**. *Appl. Phys*, **28**:2314, 1995. 42

[46] T. Davis D. Gao T. Gureyev A. Stevenson and S. Wilkins. **An X-ray interferometer**. *Appl. Phys. Lett.*, **373**:595–598, 1965. 42, 50, 80

[47] F.A. Dilmanian Z. Zhongd B. Ren X.Y. Wu L.D. Chapman I. Orion and W.C. Thomlinson. **Computed tomography of x-ray index of refraction using the diffraction enhanced imaging method**. *Phys. Med. Biol.*, **45**:933, 2000. 42

[48] Y.I. Nesterets T.E. Gureyev and S.W. Wilkins. **General reconstruction formulas for analyzer-based computed tomography**. *Appl. Phys. Lett.*, **89**:264103, 2006. 42

[49] F. Arfelli V. Bonvicini A. Bravin G. Cantatore E. Castelli L.D. Palma M.D. Michiel M. Fabrizioli R. Longo R.H. Menk A. Olivo S. Pani D. Pontoni P. Poropat M. Prest A. Rashevsky M. Ratti L. Rigon G. Tromba A. Vacchi E. Vallazza and F. Zanconati. **Mammography with synchrotron radiation: phase-detection techniques**. *Radiology*, **215**:286, 2000. 42

[50] E.D. Pisano R.E. Johnston D. Chapman J. Geradts M.V. Iacocca C.A. Livasy D.B. Washburn D.E. Sayers Z. Zhong M.Z. Kiss and W.C. Thomlinson.

Human breast cancer specimens: diffraction-enhanced imaging with histologic correlation–improved conspicuity of lesion detail compared with digital radiography. *Radiology*, **214**:895, 2000. 42

[51] J. Mollenhauer M.E. Aurich Z. Zhong C. Muehleman A.A. Cole M. Hasnah O. Oltulu K.E. Kuettner A. Margulis and L.D. Chapman. **Diffraction-enhanced X-ray imaging of articular cartilage**. *Osteoarthr. Cartil.*, **10**:163, 2002. 42

[52] P. Coan A. Wagner A. Bravin P.C. Diemoz J. Keyrilinen and J. Mollenhauer. **In vivo x-ray phase contrast analyzer-based imaging for longitudinal osteoarthritis studies in guinea pigs**. *Phys. Med. Biol.*, **55**:7649, 2010. 42

[53] J. Clauser. **Ultrahigh resolution interferometric X-ray imaging**. *Patent US5812629*, 1965. 42

[54] H. Talbot. **Facts relating to optical science**. *Philos. Magaz. and J. of Sci.*, 1836. 42, 51

[55] T. Weitkamp A. Diaz C. David F. Pfeiffer M. Stampanoni P. Cloetens and E. Ziegler. **X-ray phase imaging with a grating interferometer**. *Opt. Exp.*, **13**:6296–6304, 2005. 43, 44

[56] A. Momose W. Yashiro Y. Takeda Y. Suzuki and T. Hattori. **Phase Tomography by X-ray Talbot Interferometry for Biological Imaging**. *Japan J. Appl. Phys.*, **45**:5254–5262, 2006. 43

[57] C. David B. Nöhammer H. Solak and E. Ziegler. **Differential x-ray phase contrast imaging using a shearing interferometer**. *Appl .Phys. Lett.*, **81**:3287, 2002. 43, 51, 80

[58] F. Pfeiffer T. Weitkamp O. Bunk and C. David. **Phase retrieval and differential phase-contrast imaging with low-brilliance X-ray sources**. *Nature Phys.*, **2**:258, 2006. 44, 51, 80, 83

[59] F. Pfeiffer M. Bech O. Bunk P. Kraft E.F. Eikenberry Ch. Bronnimann C. Grunzweig and C. David. **Hard-X-ray dark-field imaging using a grating interferometer**. *Nature Materials*, **7**:134–137, 2008. 44, 52

[60] F. Pfeiffer T. Weitkamp O. Bunk and C. David. **Hard X-Ray Phase Tomography with Low-Brilliance Sources**. *Phys. Rev. Lett.*, **98**:108105, 2007. 44

[61] I. Zanette T. Weitkamp T. Donath S. Rutishauser and C. David. **Two-dimensional x-ray grating interferometer**. *Am. Phys. Soc.*, **105**:248102, 2010. 44

[62] N. Morimoto S. Fujino A. Yamazaki Y. Ito T. Hosoi H. Watanabe and T. Shimura. **Two dimensional x-ray phase imaging using single grating interferometer with embedded x-ray targets**. *Opt. Expr.*, **23**:16582, 2015. 44

[63] F. Pfeiffer J. Herzen M. Willner M. Chabior S. Auweter M. Reiser and F. Bamberg. **Grating-based X-ray phase contrast for biomedical imaging applications**. *Z. Med. Phys.*, **23**:176, 2013. 45

[64] A. Olivo F. Arfelli G. Cantatore R. Longo R. Menk S. Pani M. Prest P. Poropat L. Rigon G. Tromba E. Vallazza and E. Castelli. **An innovative digital imaging set-up allowing a low-dose approach to phase contrast applications in the medical fiels**. *Med Phys*, **28**:1609–1610, 2001. 45, 51, 80

[65] A. Olivo and R. Speller. **Modelling of a novel X-ray phase contrast imaging technique based on coded apertures**. *Phys Med Biol*, **52**:6555–6573, 2007. 47, 81, 87, 97, 99

[66] A. Olivo D. Chana and R. Speller. **A preliminary investigation of the potential of phase contrast x-ray imaging in the field of homeland security**. *J. Phys. D: Appl. Phys.*, **41**:225503, 2008. 49

[67] A. Olivo K. Ignatyev P. Munro and R.D. Speller. **Design and realization of a coded-aperture based X-ray phase contrast imaging for homeland security applications**. *Nucl. Instrum. methods A*, **610**:604, 2009. 49

[68] K. Ignatyev P.R.T. Munro D. Chana R.D. Speller and A. Olivo. **A New Generation of X-ray Baggage Scanners Based on a Different Physical Principle**. *Materials*, **4**:1846, 2011. 49

[69] M. Marenzana C.K. Hagen P. Das Neves Borges M. Endrizzi M.B. Szafraniec T.L. Vincent L. Rigon F. Arfelli R.H. Menk and A. Olivo. **Synchrotron- and laboratory-based X-ray phase-contrast imaging for imaging mouse articular cartilage in the absence of radiopaque contrast agents**. *Philos. Trans. R. Soc. A*, **372**:20130127, 2014. 49

[70] A. Kavanagh A. Olivo R. Speller and B. Vojnovic. **Feasibility testing of a preclinical coded aperture phase contrast imaging configuration using a simple fast Monte Carlo simulator**. *Biomed. Opt. Express*, **5**:93, 2014. 49

[71] A. Olivo S. Gkoumas M. Endrizzi C.K. Hagen M.B. Szafraniec P.C. Diemoz P.R. Munro K. Ignatyev B. Johnson J.A. Horrocks S.J. Vinnicombe J.L. Jones and R.D. Speller. **Low-dose phase contrast mammography with conventional x-ray sources**. *Med. Phys.*, **40**:090701, 2013. 49

[72] A. Olivo P.C. Diemoz and A. Bravin. **Amplification of the phase contrast signal at very high x-ray energies**. *Opt. Lett.*, **37**:915, 2012. 49

[73] M. Endrizzi P.C. Diemoz M.B. Szafraniec C.K. Hagen T.P. Millard C.E. Zapata P.R.T. Munro K. Ignatyev M. Marenzana R.D. Speller and A. Olivo. **Edge illumination and coded-aperture X-ray phase-contrast imaging: increased sensitivity at synchrotrons and lab-based translations into medicine, biology and materials science**. *Proc. SPIE*, **8668**:866812, 2013. 49

[74] A. Olivo S.E. Bohndiek J.A. Griffiths A. Konstantinidis and R.D. Speller. **A non-free-space propagation x-ray phase contrast imaging method sensitive to phase effects in two directions simultaneously**. *Appl. Phys. Lett.*, **94**:044108, 2009. 49

[75] A. Olivo and R.D. Speller. **A laboratory based edge-illumination x-ray phase-contrast imaging setup with two-directional sensitivity**. *Appl. Phys. Lett.*, **107**:204105, 2015. 49

[76] A. Olivo and R. Speller. **Image formation principles in coded-aperture based X-ray phase contrast imaging**. *Phys Med Biol*, **53**:6461–6474, 2008. 49, 51, 81

[77] A. Olivo and E. Castelli. **X-ray phase contrast imaging: From synchrotrons to conventional sources**. *It. Phys. Soc.*, **37**:467, 2014. 50, 51, 147

[78] A. Olivo and R.D. Speller. **A coded-aperture technique allowing x-ray phase contrast imaging with conventional sources**. *Appl .Phys. Lett.*, **91**:074106, 2007. 51, 80, 97

[79] T. Millard M. Endrizzi K. Ignatyev C. Hagen P. Munro R. Speller and A. Olivo. **Method for automatization of the alignment of a laboratory based x-ray phase contrast edge illumination system**. *Rev. Sci. Instr.*, **84**:083702, 2013. 51, 57, 58, 59, 60, 80

[80] P.C. Diemoz C.K. Hagen M. Endrizzi and A. Olivo. **Sensitivity of laboratory based implementations of edge illumination X-ray phase-contrast imaging**. *Appl .Phys. Lett.*, **103**:244104, 2013. 51, 52, 53, 75, 81, 83, 106, 109

[81] A. Olivo S. Gkoumas M. Endrizzi C.K. Hagen M.B. Szafraniec P.C. Diemoz P.R.T. Munro K. Ignatyev B. Johnson J.A. Horrocks S.J. Vinnicombe J.L. Jones and R.D. Speller. **Low-dose phase contrast mammography with conventional x-ray sources**. *Med. Phys.*, **40**:090701, 2013. 51

[82] W. Richardson. **Bayesian-based iterative method of image restoration**. *J. Opt. Soc. Am.*, **62**:55, 1972. 52, 88, 89

[83] M. Endrizzi F.A. Vittoria P.C. Diemoz R. Lorenzo R.D. Speller U.H. Wagner C. Rau I.K. Robinson and A. Olivo. **Phase-contrast microscopy at high x-ray energy with a laboratory setup**. *Opt. Lett.*, **39**:3332, 2014. 52, 81, 95

[84] I.K. Robinson A. Olivo F.A. Vittoria G.K.N. Kallon D. Basta P.C. Diemo and M. Endrizzi. **Beam tracking approach for singleshot retrieval of absorption, refraction, and darkfield signals with laboratory xray sources**. *Appl. Phys. Lett.*, **106**:224102, 2015. 52

[85] D. Reboredo et al. **Phase-contrast imaging using radiation sources based on laser-plasma wakefield accelerators: state of the art and future development**. *Proc. of SPIE*, **445**:94120, 2015. 53, 132, 133, 138, 146

[86] P.C. Diemoz et al. **X-Ray Phase-Contrast Imaging with Nanoradian Angular Resolution**. *Phys. Rev. Lett.*, **110**:138105, 2013. 55, 125, 134

[87] D. Basta M. Endrizzi F.A. Vittoria G.K.N. Kallon T.P.M. Millard P.C. Diemoz and A. Olivo. **Design and realization of a portable Edge Illumination X-ray Phase Contrast imaging system**. *Rev. Sci. Instr.*, **86**:096102, 2015. 56, 104, 127, 128, 135

[88] P.R.T. Munro C.K. Hagen M.B. Szafraniec and A. Olivo. **A simplified approach to quantitative coded aperture X-ray phase imaging**. *Opt. Express*, **21**:11187, 2013. 59

[89] M. Endrizzi P.C. Diemoz T.P. Millard J.L. Jones R.D. Speller I.K. Robinson and A. Olivo. **Hard X-ray dark-field imaging with incoherent sample illumination**. *Appl .Phys. Lett.*, **104**:024106, 2014. 59, 74, 99, 127

[90] P.C. Diemoz F.A. Vittoria and A. Olivo. **Spatial resolution of edge illumination X-ray phase-contrast imaging**. *Opt. Express*, **22**:15514, 2014. 59, 87

[91] M. Endrizzi F.A. Vittoria G. Kallon D. Basta P.C. Diemoz A. Vincenzi P. Delogu R. Bellazzini and A. Olivo. **Achromatic approach to phase-based multi-modal imaging with conventional X-ray sources**. *Opt. Express*, **23**:16473, 2015. 80

[92] P.R.T. Munro K. Ignatyev R.D. Speller and A. Olivo. **Phase and absorption retrieval using incoherent X-ray sources**. *Proc. Natl. Acad. Sci. U.S.A.*, **109**:13922, 2012. 80, 83, 97, 99

[93] M. Endrizzi D. Basta and A. Olivo. **Laboratory-based X-ray phase-contrast imaging with misaligned optical elements**. *Appl. Phys. Lett.*, **107**:124103, 2015. 80

[94] P.C. Diemoz and A. Olivo. **On the origin of contrast in edge illumination X-ray phase-contrast imaging**. *Opt. Express.*, **22**:28199, 2014. 81

[95] D. Basta M. Endrizzi F. A. Vittoria A. Astolfo and A. Olivo. **Compact and cost effective lab-based edge-illumination x-ray phase contrast imaging with a structured focal spot**. *App. Phys. Lett.*, **108**:224102, 2016. 82, 104

[96] A. Olivo K. Ignatyev P.R.T. Munro and R.D. Speller. **Noninterferometric phase-contrast images obtained with incoherent x-ray sources**. *Appl. Opt.*, **50**:1765, 2011. 83

[97] A. Zamir P.C. Diemoz F.A. Vittoria C.K. Hagen M. Endrizzi A. Olivo. **Edge illumination X-ray phase tomography of multi-material samples using a single-image phase retrieval algorithm**. *Opt. Expr.*, **25**:11984, 2017. 87

[98] P.C. Diemoz M. Endrizzi F.A. Vittoria C. K. Hagen G. Kallon D. Basta M. Marenzana P. Delogu A. Vincenzi L. De Ruvo G. Spandre A. Brez R. Bellazzini and A. Olivo. **Laboratory implementation of edge illumination X-ray phase-contrast imaging with energy-resolved detectors**. *Phys. Med. Im.*, **9412**, 2015. 87

[99] M. Endrizzi F.A. Vittoria P.C. Diemoz R. Lorenzo R.D. Speller U.H. Wagner C. Rau I.K. Robinson and A. Olivo. **Phase-contrast microscopy at high x-ray energy with a laboratory setup**. *Opt. Lett.*, **39**:3332, 2014. 87

[100] M.B. Cannell A. McMorland and C. Soeller. *Image enhancement by deconvolution.* J.B. Pawley, 2006. 89

[101] C. Preza M. Miller I. Thomas and J. McNally. **Regularized linear method for reconstruction of three-dimensional microscopic objects from optical sections**. *J. Opt. Soc. Am. A*, **9**:219, 1992. 89

[102] P.J. Shaw and D.J. Rawlins. **Three-dimensional fluorescence microscopy**. *Prog. Biophys. Mol. Biol.*, **56**:187, 1991. 89

[103] G. van Kempen L. van Vliet P. Verveer and H. van der Voort. **A quantitative comparison of image restoration methods for confocal microscopy**. *J. Microsc.*, **185**:354, 1997. 89

[104] M. Laasmaa M. Vendelin and P. Peterson. **Application of regularized Richardson-Lucy algorithm for deconvolution of confocal microscopy images**. *J. Microsc.*, **124**:243, 2011. 89, 90

[105] N. Dey L. Blanc-Feraud C. Zimmer P. Roux Z. Kam J.-C. Olivo-Marin and J. Zerubia. **Richardson-Lucy algorithm with total variation regularization for 3D confocal microscope deconvolution**. *Microsc. Res. Techniq.*, **69**:260, 2006. 89

[106] P. Modregger T.P. Cremona C. Benarafa J.C. Schittny A. Olivo and M. Endrizzi. **Small angle x-ray scattering with edge-illumination**. *Sc. Rep.*, **6**:30940, 2016. 89

[107] N. Dey L. Blanc-Feraud C. Zimmer P. Roux Z. Kam J.-C. Olivo-Marin and J. Zerubia. *3D microscopy deconvolution using Richardson-Lucy algorithm with total variation regularization*, **5272**. INRIA, 2004. 89, 90

[108] G. van Kempen and L.J. van Vliet. **The influence of the regularization parameter and the first estimate on the performance of Tikhonov regularized non-linear image restoration algorithms**. *J. Microsc.*, **198**:63, 2000. 90

[109] J.B. de Monvel E. Scarfone S.L. Calvez and M. Ulfendahl. **Image-adaptive deconvolution for three-dimensional deep biological imaging**. *Biophys. J.*, **85**:3991, 2003. 90

[110] T. Donath et al. **Inverse geometry for grating-based x-ray phase-contrast imaging**. *J. Appl. Phys.*, **106**:054703, 2009. 97

[111] T. Tajima and J. M. Dawson. **Laser Electron Accelerator**. *Phys. Rev. Lett.*, **43**:267, 1979. 126, 128

[112] D. Umstader. **Relativistic laserplasma interactions**. *J. Phys. D*, **36**:R151, 2003. 128

[113] V. Malka et al. **Electron Acceleration by a Wake Field Forced by an Intense Ultrashort Laser Pulse**. *Science*, **298**:1596, 2002. 129

[114] A. Pukhov and J. Meyer ter Vehn. **Laser wake field acceleration: the highly non-linear broken-wave regime**. *Appl. Phys. B*, **74**:355, 2002. 129

[115] D. Rousse et al. **Production of a keV X-Ray Beam from Synchrotron Radiation in Relativistic Laser-Plasma Interaction**. *Phys. Rev. Lett.*, **93**:135005, 2004. 130

[116] D.A. Jaroszynski et al. **The Strathclyde terahertz to optical pulse source (TOPS)**. *Nuclear Instruments and Methods in Physics Research Section A*, **445**:317–319, 2000. 132

[117] X. Llopart et al. **Timepix, a 65k programmable pixel readout chip for arrival time, energy and/or photon counting measurements**. *Nuclear Instruments and Methods in Physics Research Section A: Accelerators, Spectrometers, Detectors and Associated Equipment*, **581(12)**:485–494, 2007. 133

[118] A. Olivo P. C. Diemoz and A. Bravin. **Amplification of the phase contrast signal at very high x-ray energies**. *Opt. Lett.*, **37**:915–917, 2012. 134

[119] `http://www.hamamatsu.com/eu/en/product/alpha/F/4157/C9732DK-11/index.html`. 135

[120] S. Kneip et al. **Bright spatially coherent synchrotron X-rays from a table-top source**. *Nat. Phys.*, **6**:980–983, 2010. 145